Measurement of charged current deep inelastic scattering cross sections using the ZEUS detector at HERA

A. D. Tapper

Imperial College of Science, Technology and Medicine

A thesis submitted for the degree of
Doctor of Philosophy of the University of London
and the Diploma of Imperial College

Abstract

The cross section for charged current e^-p deep inelastic scattering has been measured at a centre of mass energy of 318 GeV. The measurement is based on 16.4 pb^{-1} of e^-p data taken by the ZEUS detector at HERA. The single differential cross sections with respect to Q^2, x and y, and the total cross section were measured in the kinematic region $Q^2 > 200$ GeV^2. The reduced double differential cross section was also measured, in bins of x and Q^2 in the kinematic region 200 $\text{GeV}^2 < Q^2 < 60000$ GeV^2 and $0.01 < x < 0.56$. The measurements are confronted with the Standard Model predictions evaluated using the CTEQ5D and MRST (99) parameterisations of the parton density functions. Both parameterisations are found to describe the data well. The measurements are compared with previously measured cross sections for e^+p charged current deep inelastic scattering, and cross sections for neutral current deep inelastic scattering. The mass of the W boson is extracted from $d\sigma/dQ^2$ as $M_W = 79.8 \pm 2.1(stat)\ ^{+1.8}_{-1.4}(syst)\ ^{+1.3}_{-1.2}(PDF)$ GeV. This value is found to be in good agreement with measurements of time-like W boson production made at the Tevatron and LEP.

Acknowledgements

I would like to thank my supervisor Ken Long for a wealth of help, good advice and encouragement over the past three years. I thank my friends and colleagues at Imperial College and DESY for making the past three years entertaining and reasonably productive. I would also like to thank Kunihiro Nagano, Masahiro Kuze and Stefan Schlenstedt for detailed advice. It was a pleasure to work closely with Takahiro Fusayasu, and very productive despite spending most of our time on opposite sides of the world. Finally, particular thanks must go to Rod Walker and Dave Bailey for much help and advice. I acknowledge the financial support of the *Particle Physics and Astronomy Research Council*.

I don't know if you have had the same experience, but the snag I always come up against when I'm telling a story is this dashed difficult problem of where to begin it. It's a thing you don't want to go wrong over, because one false step and you're sunk. I mean, if you fool about too long at the start, trying to establish atmosphere, as they call it and all that sort of rot, you fail to grip and the customers walk out on you.

Get off the mark, on the other hand, like a scalded cat, and your public is at a loss. It simply raises its eyebrows, and can't make out what you're talking about.

- Right Ho, Jeeves; P G Wodehouse 1934

Contents

List of Figures

List of Tables

Chapter 1

Deep inelastic scattering

1.1 Introduction

The Standard Model of particle physics [1] describes the interactions between fundamental particles. The Standard Model provides a unified description of electromagnetism, described by quantum electrodynamics (QED), and the weak force. The strong force is described in the Standard Model by quantum chromodynamics (QCD). The proton is known to be a composite particle, with constituents held together by the strong force. At the HERA collider highly energetic beams of protons collide with either electrons or positrons. The electron or positron interacts with the proton via the exchange of a gauge boson. This exchanged boson can be an electrically neutral particle, such as a photon or a Z^0, in which case the interaction is termed neutral current, or an electrically charged $W^\pm$ can be exchanged, in what is termed charged current scattering.

The kinematics of charged current and neutral current deep inelastic scattering (DIS) processes (see figure 1.1) are defined by the four-momenta of the incoming lepton (k), the incoming proton (P), the outgoing lepton (k') and the final hadronic state (P'). The four-momentum transfer between the electron and the proton is given by $q = k - k' = P' - P$. The square of the energy in the ep centre of mass is given by $s = (k + P)^2$. The description of DIS is usually given

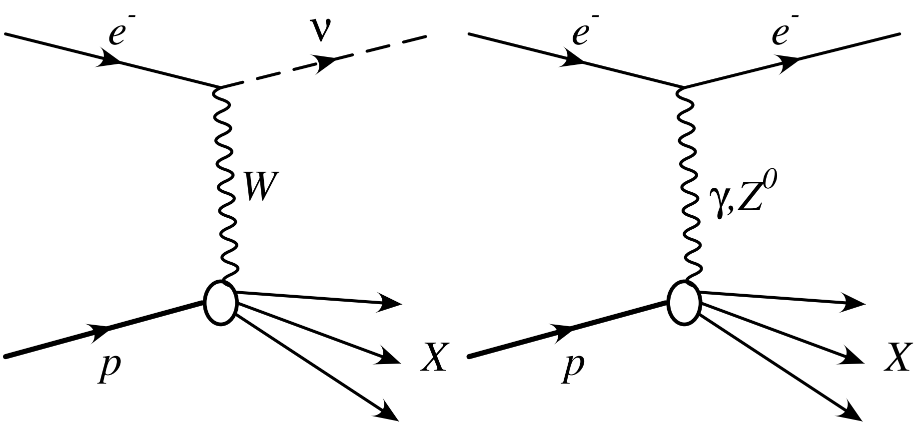

Figure 1.1: Feynman diagrams for charged current (left) and neutral current (right) DIS.

in terms of three Lorentz invariant quantities, which may be defined in terms of the four-momenta k, P and q:

- $Q^2 = -q^2$, the negative square of the four-momentum transfer,
- $x = \frac{Q^2}{2p \cdot q}$, the Bjorken scaling variable,
- $y = \frac{q \cdot P}{k \cdot P}$, the fractional energy transfer to the proton in its rest frame.

These variables are related by $Q^2 = xys$, when the masses of the particles can be neglected. At any given value of s, the kinematic variables x, y and Q^2 can be reconstructed from any two of four measured quantities: the angles of the scattered electron and hadronic jet, shown in figure 1.2, and the measured energies of the scattered electron and jet. The Q^2 of the interaction characterises how energetic the reaction is, and therefore at what scale the structure of the proton is probed. High Q^2 means that the proton structure is probed at a very small distance scale.

1.2 The quark parton model

In the naive quark parton model the proton is considered to be a collection of non-interacting point-like partons called quarks. In this model the DIS process is

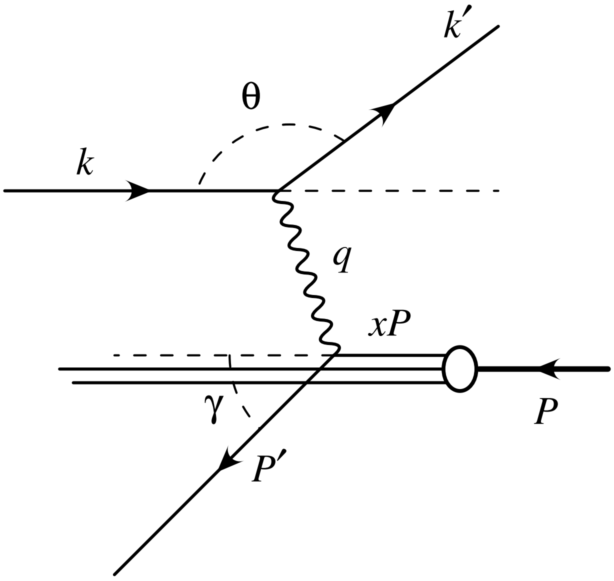

Figure 1.2: Kinematics of neutral current DIS, showing the electron scattered at an angle θ, and the hadronic jet at an angle γ to the proton beam direction.

the quasi-elastic scattering of the exchanged gauge boson off a single quark in the proton. In the quark parton model the Bjorken scaling variable, x, represents the fraction of the proton's momentum carried by the struck quark. If the quarks are assumed to be non-interacting point-like particles confined within the proton then the structure functions can be expected to be a function of x but not of Q^2, since changes in Q^2 correspond to changes in the scale probed by the exchanged boson, which will be irrelevant for point-like constituents. Figure 1.3 shows the structure function F_2^{em} measured for NC DIS as a function of Q^2 for fixed values of x [2]. F_2^{em} is the purely electromagnetic part of the F_2^{NC} structure function (see section 1.3.2). It can be seen that, for x of ~ 0.1, F_2^{em} is approximately independent of Q^2. When interactions in the proton are considered, then the possibility of quarks radiating gluons and gluons splitting to form quark-antiquark pairs cannot be ignored. At high x, the cross section is sensitive only to the valence quarks. The density of the valence quarks will fall with increasing Q^2 due to gluon radiation, resulting in scaling violation and a decrease in the cross sections. At low x, gluon radiation leads to more gluons and quark-antiquark pairs in the proton, so this scaling behaviour is not obeyed and the cross sections will rise with increasing Q^2. This can clearly be seen in figure 1.3.

1.3 Cross sections

1.3.1 Charged current deep inelastic scattering

The double differential Born cross section for the unpolarised charged current deep inelastic scattering processes $e^- p \rightarrow \nu X$ and $e^+ p \rightarrow \bar{\nu} X$ are given by [3]:

$$\frac{d^2\sigma^{CC}_{Born}(e^{\pm}p)}{dxdQ^2} = \frac{G_F^2}{4\pi x}\frac{M_W^4}{(Q^2+M_W^2)^2}[Y_+ F_2^{CC}(x,Q^2) - y^2 F_L^{CC}(x,Q^2) \mp Y_- xF_3^{CC}(x,Q^2)] \tag{1.1}$$

where $Y_{\pm} = 1 \pm (1-y)^2$, G_F is the Fermi coupling constant and M_W is the mass of the W boson (units in which $\hbar = c = 1$ are used throughout). The charged current structure functions in the quark parton model for $e^- p$ scattering are given by:

$$F_2^{CC}(x,Q^2) = \sum_{q=u,c,t} xq(x,Q^2) + \sum_{q=d,s,b} x\bar{q}(x,Q^2) \tag{1.2}$$

$$xF_3^{CC}(x,Q^2) = \sum_{q=u,c,t} xq(x,Q^2) - \sum_{q=d,s,b} x\bar{q}(x,Q^2) \tag{1.3}$$

similarly for $e^+ p$ scattering:

$$F_2^{CC}(x,Q^2) = \sum_{q=d,s,b} xq(x,Q^2) + \sum_{q=u,c,t} x\bar{q}(x,Q^2) \tag{1.4}$$

$$xF_3^{CC}(x,Q^2) = \sum_{q=d,s,b} xq(x,Q^2) - \sum_{q=u,c,t} x\bar{q}(x,Q^2) \tag{1.5}$$

where the parton density functions (PDFs), $q(x,Q^2)$, give the probablility of finding a quark, q, with momentum fraction x at a given Q^2. The structure

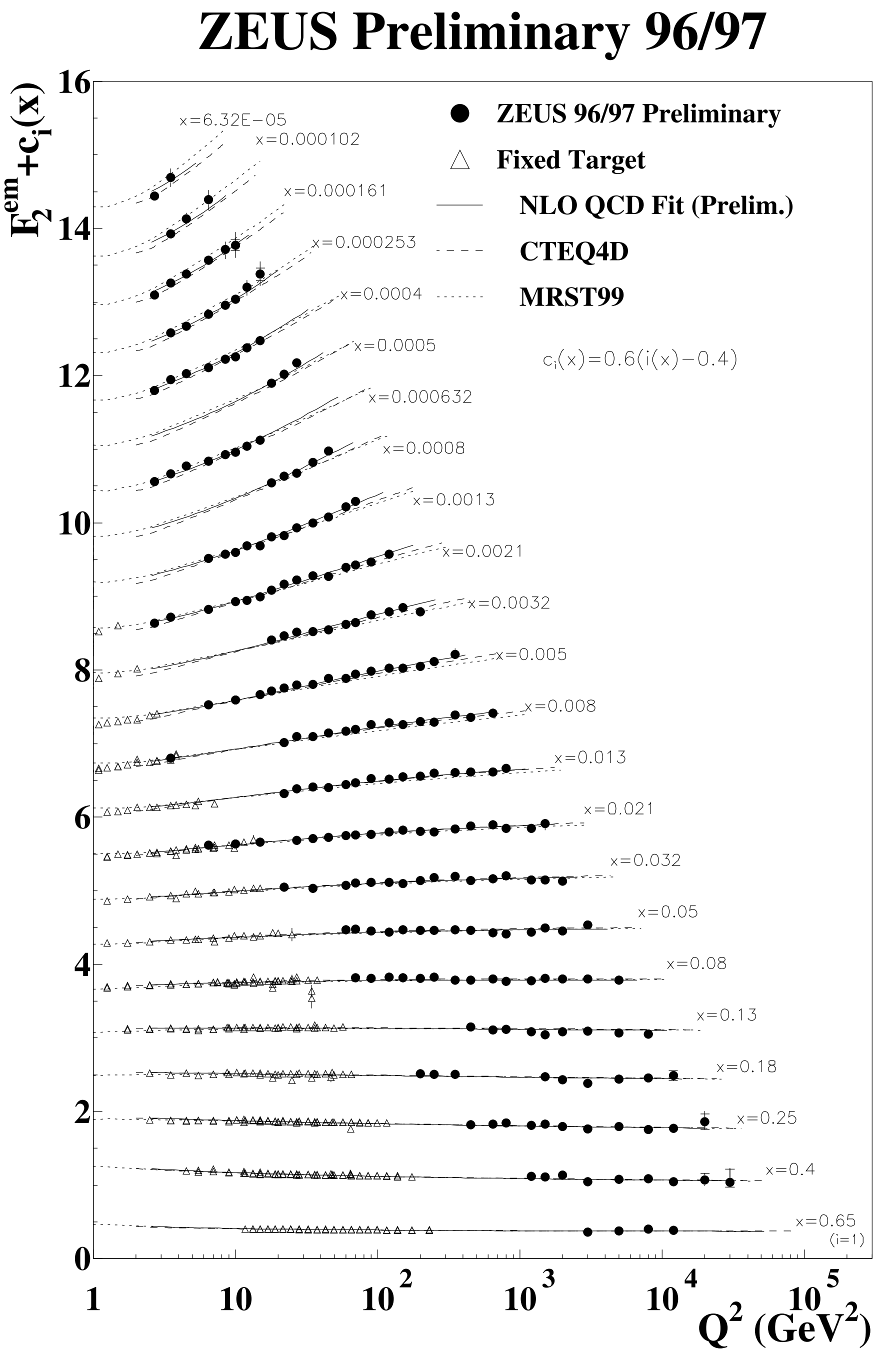

Figure 1.3: The structure function F_2^{em} measured for NC DIS as a function of Q^2 for fixed values of x [2].

function $F_L^{CC}(x, Q^2)$ gives the contribution to the cross section of longitudinally polarised W bosons, and in the quark parton model $F_L^{CC}(x, Q^2) = 0$. The energy at HERA is insufficient to give significant contributions from bottom and top quarks. Substituting the parton density functions into the expression for the Born cross section gives:

$$\frac{d^2\sigma^{CC}_{Born}(e^-p)}{dxdQ^2} = \frac{G_F^2}{2\pi}\frac{M_W^4}{(Q^2+M_W^2)^2}[(u+c)+(1-y)^2(\bar{d}+\bar{s})] \tag{1.6}$$

$$\frac{d^2\sigma^{CC}_{Born}(e^+p)}{dxdQ^2} = \frac{G_F^2}{2\pi}\frac{M_W^4}{(Q^2+M_W^2)^2}[(\bar{u}+\bar{c})+(1-y)^2(d+s)] \tag{1.7}$$

The form of the cross sections can be understood in terms of the V-A nature of the weak interaction. Weak isospin is responsible for different quark flavours contributing to e^-p and e^+p scattering. This means that the structure of the proton can be probed in a flavour specific way using the charged current interaction. It can be shown that the scattering angle of an electron in electron-quark scattering, in the electron quark centre of mass frame, θ^*, is related to y in the following way:

$$1 - y = \frac{1+\cos\theta^*}{2} \tag{1.8}$$

Helicity conservation imposes isotropic scattering for electron-quark and positron-antiquark scattering. For electron-antiquark and positron-quark scattering the angular dependence is given by $(1+\cos\theta^*)^2$ which is proportional to $(1-y)^2$. Hence the antiquarks are suppressed by a factor of $(1-y)^2$ in the cross section for e^-p charged current scattering and vice versa in the case of e^+p scattering.

1.3.2 Neutral current deep inelastic scattering

The double differential Born cross section for the neutral current deep inelastic scattering processes $e^-p \to e^-X$ and $e^+p \to e^+X$ is given by:

$$\frac{d^2\sigma^{NC}_{Born}(e^{\pm}p)}{dxdQ^2} = \frac{2\pi\alpha^2}{xQ^4}[Y_+F_2^{NC}(x,Q^2) - y^2F_L^{NC}(x,Q^2) \mp Y_-xF_3^{NC}(x,Q^2)] \quad (1.9)$$

where $Y_\pm = 1 \pm (1-y)^2$, and α is the QED coupling constant. The neutral current structure functions in the quark parton model, where $F_L^{NC}(x,Q^2) = 0$, are given by:

$$F_2^{NC}(x,Q^2) = \frac{1}{2}\sum_q[(V_q^L)^2+(V_q^R)^2+(A_q^L)^2+(A_q^R)^2][xq(x,Q^2)+x\bar{q}(x,Q^2)] \quad (1.10)$$

$$xF_3^{NC}(x,Q^2) = \sum_q[V_q^LA_q^L - V_q^RA_q^R][xq(x,Q^2) - x\bar{q}(x,Q^2)] \quad (1.11)$$

For neutral current scattering all quark flavours contribute, so the sums run over all quarks in the proton, q. The structure function xF_3^{NC} has contributions from the interference between the photon and Z^0 exchange amplitudes, and Z^0 exchange, and violates parity. The functions V_q and A_q can be written as

$$V_q^{L,R} = e_q - (v_e \pm a_e)v_q\chi_Z(Q^2) \quad (1.12)$$

$$A_q^{L,R} = -(v_e \pm a_e)a_q\chi_Z(Q^2) \quad (1.13)$$

where $a_i = T_i^3$ and $v_i = T_i^3 - 2e_i\sin^2\theta_W$, T_i^3 is the weak isospin, θ_W is the weak mixing angle and e_i is the charge in units of the positron charge. The function $\chi_Z(Q^2)$ is proportional to the ratio of Z^0 and photon propagators

$$\chi_Z(Q^2) = \frac{1}{4\sin^2\theta_W\cos^2\theta_W}\frac{Q^2}{Q^2+M_Z^2} \quad (1.14)$$

1.4 Parton density functions

The cross sections depend on the parton density functions, $q(x, Q^2)$, which give the probability of finding a quark, q, with momentum fraction x at a given Q^2. These functions cannot be calculated analytically and must instead be determined by global fits to many measured experimental data sets. The PDFs are parameterised in x at a fixed starting value of Q^2 and can then be evolved using the DGLAP [4] equations to all points in Q^2 where perturbative QCD is applicable. Figure 1.3 shows the predictions of the Standard Model using three different parameterisations of the PDFs. The predictions evaluated using CTEQ4D [5], MRST (99) [6] and the ZEUS NLO QCD fit [7]. All describe the data well.

1.5 Electroweak radiative corrections

The $\mathcal{O}(\alpha)$ electroweak radiative corrections to the charged current DIS Born cross section are shown in figure 1.4. There are contributions from initial state radiation (ISR) from the incoming electron and quark, photon emission from the exchanged W boson and final state radiation (FSR) from the outgoing quark. The largest of these is the contribution from the emission of a photon from the incoming electron. Additional contributions to the electroweak radiative corrections come from W self energy, lepton vertex loops and two boson exchange as shown in figure 1.5. The largest contribution from these is the W self energy diagram.

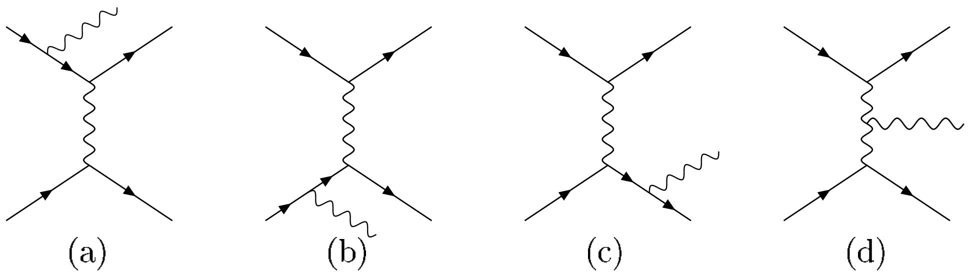
(a) (b) (c) (d)

Figure 1.4: $\mathcal{O}(\alpha)$ electroweak radiative corrections to the charged current DIS Born cross section arising from (a) initial state radiation from the incoming lepton, (b) initial state radiation from the incoming parton, (c) final state radiation from the struck parton and (d) radiation from the exchanged boson.

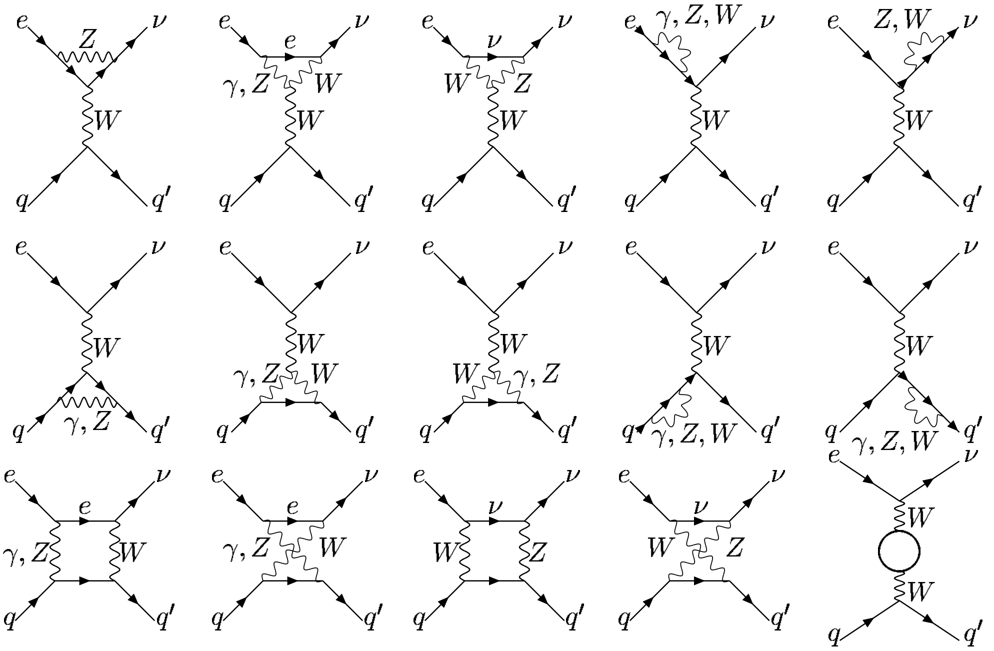

Figure 1.5: Electroweak radiative corrections to the charged current DIS Born cross section.

Chapter 2

HERA and the ZEUS detector

2.1 The HERA accelerator

The HERA accelerator [8] is situated at the DESY (Deutsches Elektronen-Synchrotron) laboratory in Hamburg. Protons and electrons (or positrons) are collided in HERA. The layout of HERA and the pre-accelerators is shown in figure 2.1. Between 1994 and 1997 positrons of energy 27.5 GeV were collided with protons of energy 820 GeV. In 1998 and early 1999 27.5 GeV electrons were collided with protons of energy 920 GeV, to give electron-proton (ep) interactions at a centre of mass energy of 318 GeV. Later in 1999 and 2000 HERA switched back to colliding 27.5 GeV positrons with 920 GeV protons. This analysis is based on the e^-p data of integrated luminosity 16.4 pb^{-1} that was collected by the ZEUS experiment in 1998 and 1999 (see figure 2.2).

The configuration of the HERA collider gives a maximum of 220 bunches in each beam, with bunches colliding every 96 ns. The number of bunches actually filled with electrons (or positrons) and protons has been increased since the comissioning of HERA up to the current usual value of 170 colliding bunches. This means that some electron (or positron) bunches and some proton bunches are left unfilled. The partners of the unfilled bunches are termed electron or proton pilot bunches and are used in the estimation of beam related background quantities.

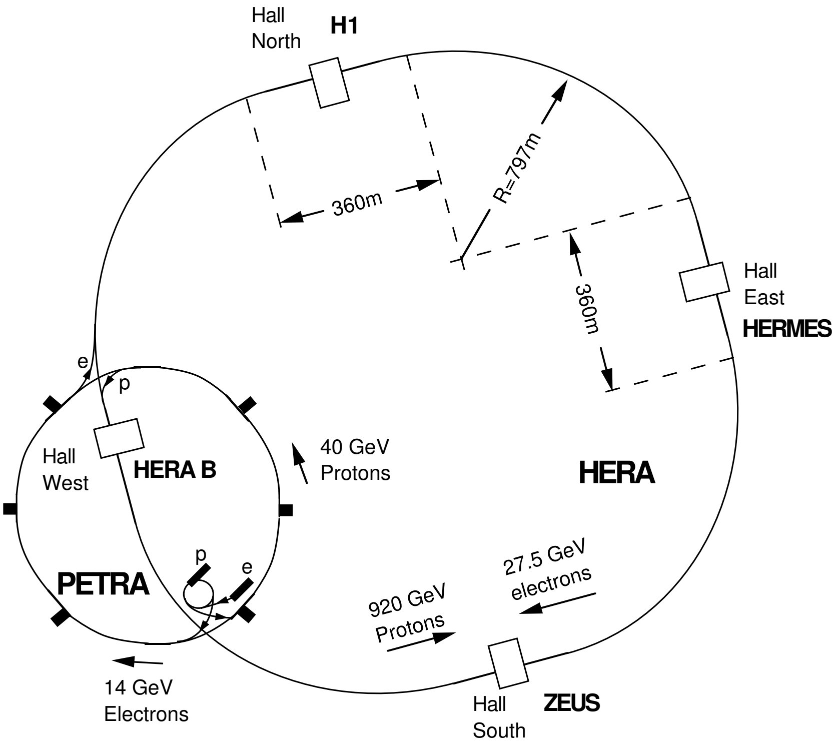

Figure 2.1: The layout of the HERA accelerator and pre-accelerators.

2.2 The ZEUS detector

The ZEUS detector [9] collects data from *ep* interactions in the HERA collider. Figures 2.3 and 2.4 show the layout of the ZEUS detector components. The ZEUS coordinate system is right-handed with the Z axis pointing in the proton direction (referred to as forward) and the X axis pointing towards the centre of HERA.

The main components of the detector used in this analysis are the central tracking detector, the uranium-scintillator calorimeter and the luminosity monitor.

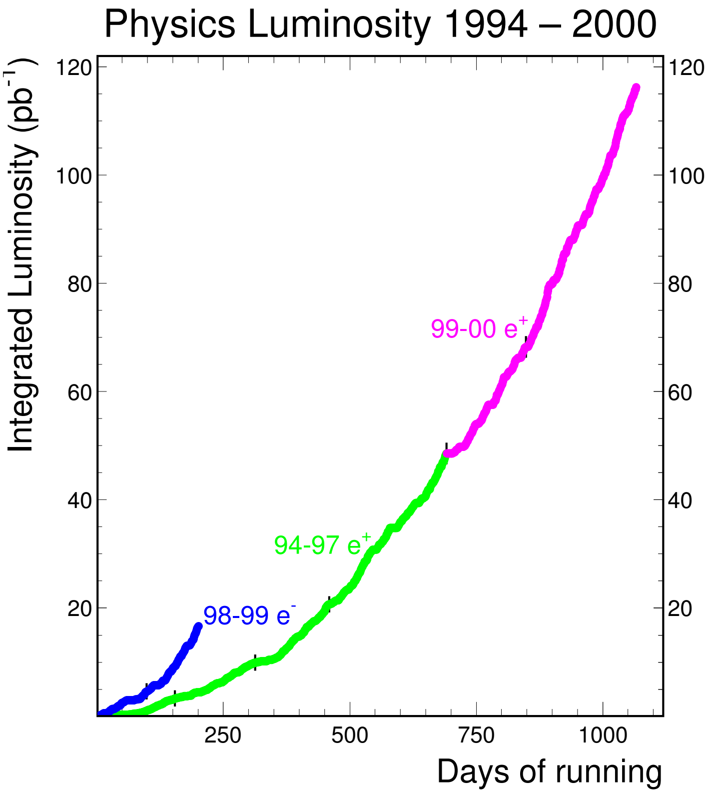

Figure 2.2: Integrated luminosity suitable for physics analysis collected by the ZEUS experiment between 1994 and 2000.

2.2.1 Uranium-scintillator calorimeter

The calorimeter [10] is split into three sections, forward (FCAL), barrel (BCAL), and rear (RCAL). The layout of the calorimeter sections is shown in figure 2.5. The calorimeter is hermetic, apart from holes in FCAL and RCAL for the beam pipe, and covers 99.7% of the solid angle around the interaction point. Each section of the calorimeter is divided into electromagnetic (EMC) cells, and hadronic (HAC) cells. FCAL and BCAL have two layers of HAC cells (HAC1 and HAC2) and one layer of EMC cells. RCAL has one layer of each of EMC and HAC cells. The FCAL is more segmented than RCAL having 4 EMC cells to each HAC cell. The RCAL has 2 EMC cells per HAC cell. The hole for the beampipe is smaller in the rear calorimeter. The cells are made up of sheets of depleted

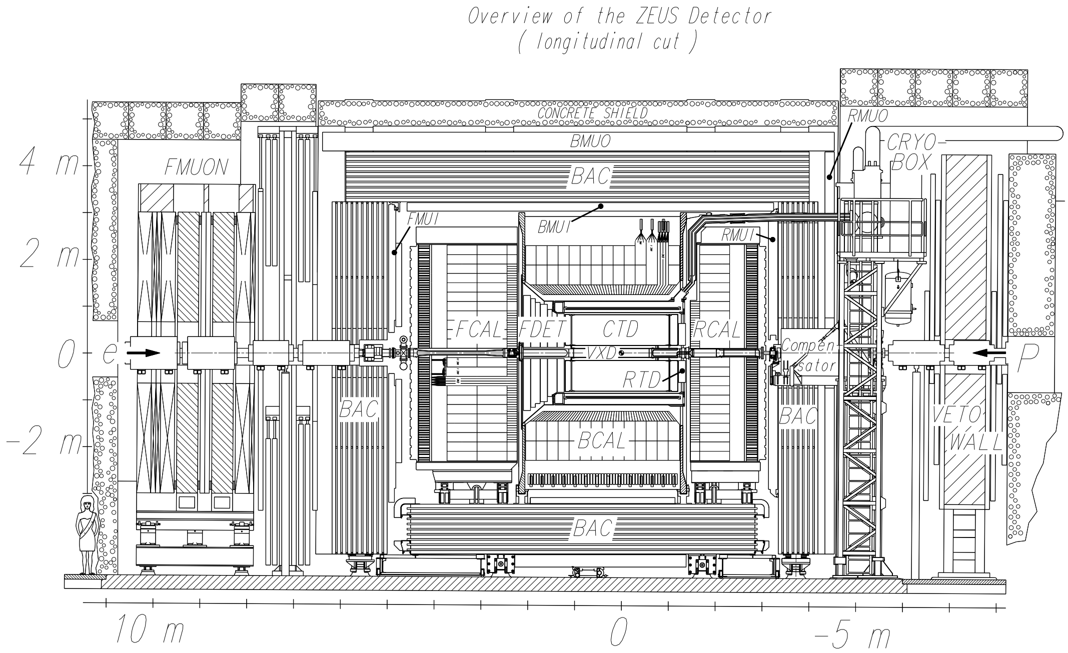

Figure 2.3: A side view of the ZEUS detector.

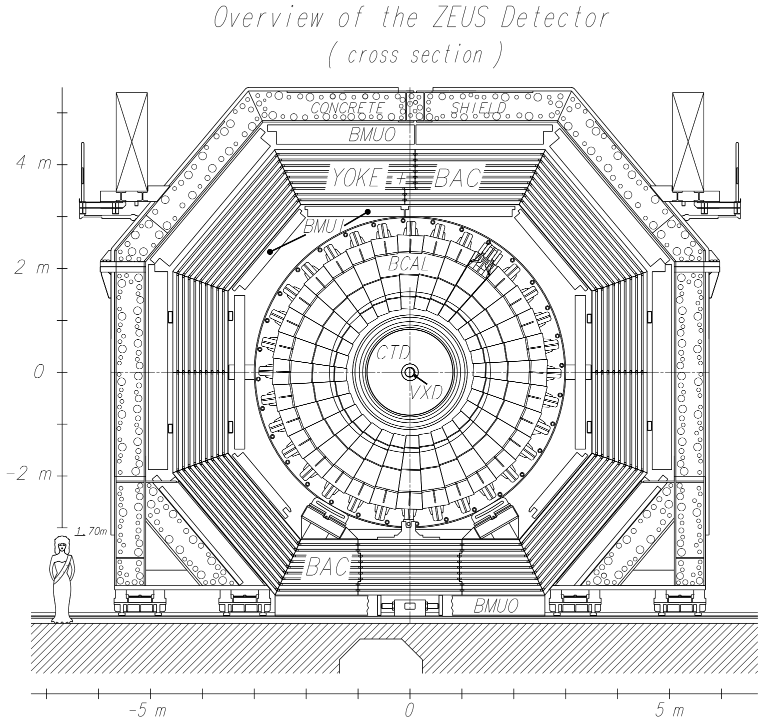

Figure 2.4: An XY projection of the ZEUS detector.

uranium absorber, interleaved with sheets of plastic scintillator. Light from the scintillator material is conveyed to two photomultiplier tubes (PMTs), connected by wavelength shifters to each cell, where it is converted into an electrical signal (see figure 2.6). The energy resolution of the calorimeter from test beam data is $35\%/\sqrt{\mathrm{E}} \oplus 2\%$ for hadronic deposits and $18\%/\sqrt{\mathrm{E}} \oplus 1\%$ for electromagnetic energy (with E in GeV). The calorimeter also provides timing information for energy deposits. The resolution of this timing is better than 1 ns, for energy deposits greater than 4.5 GeV.

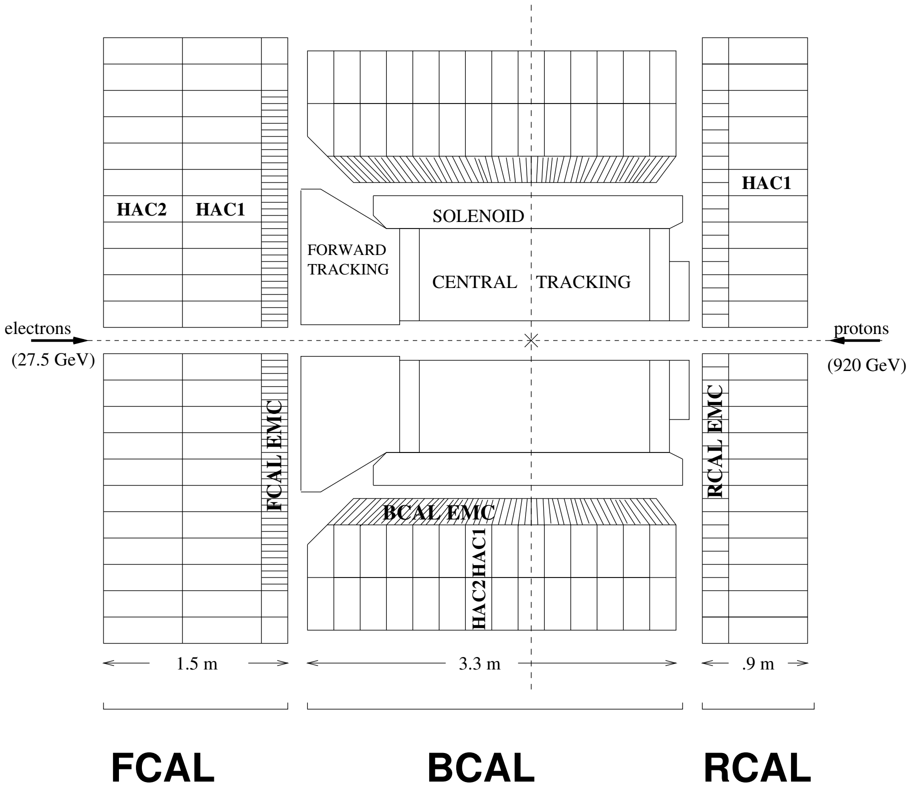

Figure 2.5: A side view of the calorimeter showing the three separate calorimeter sections and the layout of EMC and HAC cells.

2.2.2 Central Tracking Detector

The central tracking detector (CTD) [11] is a cylindrical drift chamber, positioned at the centre of the ZEUS detector, and enclosed in a 1.43 T solenoidal magnetic

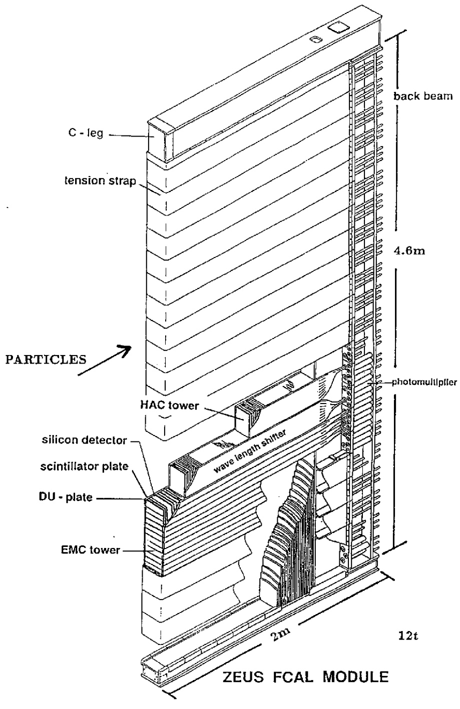

Figure 2.6: A forward calorimeter module. The EMC and HAC sections, the layers of depleted uranium (DU) and the wavelength shifters that convey the light to the PMTs can be seen.

field. It is used to reconstruct the tracks of charged particles emerging from the collisions. The measured tracks can then be used to determine the momentum of the charged particles and the coordinates of the interaction vertex. The CTD covers the range $15^\circ < \theta < 164^\circ$, and consists of 72 radial layers, organised into 9 "superlayers" as shown in figure 2.7. Each superlayer has wires parallel to the beam line and inclined at $\sim \pm 5^\circ$ to the Z axis (stereo layers), in order to determine the Z trajectory of tracks. For trigger purposes superlayers 1, 3 and 5 determine the Z trajectory of tracks from timing information with a resolution of $\sim$5 cm. Typical resolution in $r-\phi$ is 230 μm, which gives a transverse momentum resolution of $\sigma(P_T)/P_T = 0.0058 P_T \oplus 0.0065 \oplus 0.0014/P_T$ (with P_T in GeV) for long tracks [12].

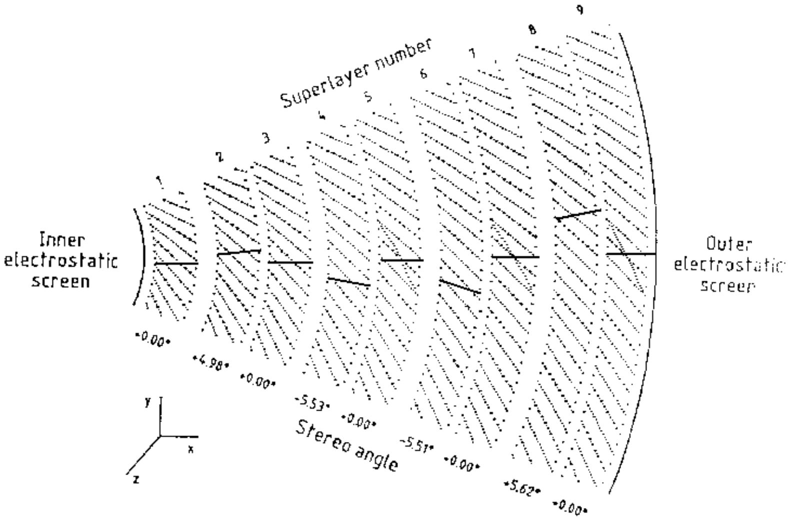

Figure 2.7: An octant of the CTD showing the wires arranged into nine superlayers.

2.2.3 Luminosity monitor

The luminosity delivered by HERA is measured using the Bethe-Heitler [13] reaction $ep \rightarrow ep\gamma$. The luminosity monitoring system consists of an electron detector and a photon detector, positioned 35 m and 108 m respectively from the centre of the detector in the electron beam direction. The layout is shown in figure 2.8. The final state particles, in the Bethe-Heitler reaction, are emitted at very small angles with respect to the initial electron direction. Magnets for bending the electron beam act as a spectrometer for off beam energy electrons and deflect them into the electron detector. The final state photons travel inside the proton beam pipe until it bends away, at which point the photons leave the beam pipe and enter the photon detector. The photon and electron detectors both consist of lead-scintillator calorimeters equiped with position detectors. The photon detector also has an adjustable thickness carbon filter and an air filled Cerenkov counter. The luminosity measurement uses the rate of Bethe-Heitler photons measured by the photon detector [14]. The collected luminosity was measured with an uncertainty of 1.8%.

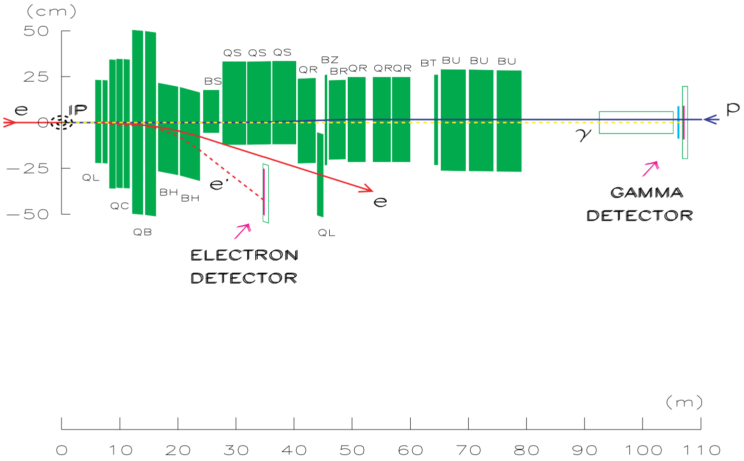

Figure 2.8: The layout of the luminosity monitor. The x axis shows the distance along the beam line from the centre of the detector and the y axis shows the transverse distance from the beam line of the detectors that make up the luminosity monitor.

2.2.4 Backing calorimeter

The iron flux return for the solenoid that provides the magnetic field for the CTD is instrumented and makes up the backing calorimeter (BAC). There is an analogue output in order to measure the energy of showers that are not fully contained in the calorimeter. This allows hadronic jets in the calorimeter to be matched to energy deposits in the BAC. There is also a digital readout which provides high precision position measurement in two dimensions. This can be used to identify muons passing through the BAC.

2.2.5 Muon chambers

Muon chambers surround the central detector components. The barrel (BMU) and rear (RMU) muon chambers cover approximately the same angular ranges as the BCAL and RCAL respectively, except that the barrel muon detector has no bottom octant. The BMU and RMU have inner and outer detectors placed on the inside and outside of the BAC. The forward muon detector (FMU) is slightly different in that it has outer detectors which have additional drift chambers compared to the BMU and RMU housed in a separate magnetic field of 1.7 T. The extra detectors provide high precision measurements of position and momentum for muons travelling in the forward direction.

2.2.6 Background vetos

The C5 counter is positioned 315 cm from the interaction point in the direction of the RCAL. It consists of scintillation counters that provide timing information for particles associated with the electron and proton bunches. It is used in the trigger chain to veto events which have timing inconsistent with the HERA *ep* bunch crossing.

The veto wall is an iron wall, instrumented on both sides, that is positioned 750 cm from the interaction point in the direction of the RCAL. The veto wall helps to protect the central detector components from particles that make up the beam halo which accompanies the proton bunches, by absorbing some of them. Also events in which particles have passed through the veto wall into the main detector can be rejected by the veto wall.

2.2.7 Trigger

Events are selected using a three level trigger system [15]. The function of the trigger system is to eliminate events due to non-*ep* background processes. The main background processes are beam gas interactions in which an electron or proton from one of the colliding beams interacts with residual gas in the beam pipe, and beam halo interactions in which the proton or electron interacts with some part of the accelerator outside the detector, and the resulting particles are detected. Also cosmic muons passing through the detector are a source of background.

The small time interval between HERA bunch crossings requires that the first level trigger (FLT) is hardware based. Digital and analogue pipelines are used to store data from the detector components in order to provide enough time for the data to be processed and a decision to be reached. Each individual component that partcipates in the FLT decision processes its own data and sends information to the global first level trigger (GFLT). The GFLT combines the information from different components and issues the decision to keep or discard the event. The data available to the FLT components is a subset of the full data.

The two key components for triggering on charged current DIS events are the calorimeter FLT (CFLT) [16] and the CTD FLT [17]. Due to the short time available the CFLT is not able to make use of all the calorimeter information. The full granularity of the calorimeter is not used, instead cells are grouped into towers made up of four (two in RCAL) EMC cells, and the HAC1 cells adjacent to them and the HAC2 cells adjacent to the HAC1 cells, in BCAL and FCAL. The combined energy of each tower is read out by the CFLT, with a lower energy threshold of a few hundred MeV. This means that towers with energy below this threshold are considered to have no energy and are ignored. The tower energies are combined to give global quantities. These energies are digitised on a course logarithmic scale in order to give a large range, which leads to a reduction in accuracy. Another approximation made at the FLT is that the vertex is assumed to be at Z=0 cm. This effects the measured transverse momentum.

There is insufficient time available for the CTD FLT to perform track fitting to the hits detected in the CTD. Instead a pattern recognition algorithm is used to look at the distribution of hits in sections of the CTD and determine whether they line up to form a track and then whether this track points to the nominal interaction point at $Z = 0$ cm. The Z coordinates used in the pattern recognition come from the timing information available for superlayers 1, 3 and 5 since there is insufficient time to use the data from the stereo layers. Finally, the total number of tracks and the number of these tracks that point to the interaction vertex, are used to select or veto each event. The overall effect of the processing time contraint at the first level trigger is that the quantities measured by the CFLT and CTD FLT do not correspond closely to the offline quantities.

The second level trigger (SLT) is based on a set of parallel processing transputers. Data from each component are processed simultaneously and then sent to the global second level trigger, which issues the decision to keep or discard the event. At the SLT level it is possible to use the full granularity of the calorimeter to measure energies and there is sufficient time to perform track fitting on the hits measured in the CTD. There is not however enough processing time to use the stereo layer information from the CTD to determine the Z position of tracks and the interaction vertex.

The third level trigger (TLT) consists of a farm of computers running a reduced version of the offline analysis software. The full data set is available to the TLT and differs from the offline data only slightly due to calibrations that are not available at the time the data are taken. The main differences are in the energy calibration of the calorimeter, which is determined on an approximately run by run basis from dedicated calibration runs taken between physics runs. Also calibration constants for the CTD reconstruction are adjusted offline, according to environmental data such as the temperature and pressure for each run. The output from the TLT is at a rate that is suitable for writing to tape or disk.

Figure 2.9 is a schematic view of the trigger system, simplified by only showing the CAL and CTD components in detail. The reduction in rate at each stage, from the FLT input rate of 10^7 Hz, to the rate of 5 Hz that is written to offline tape is shown.

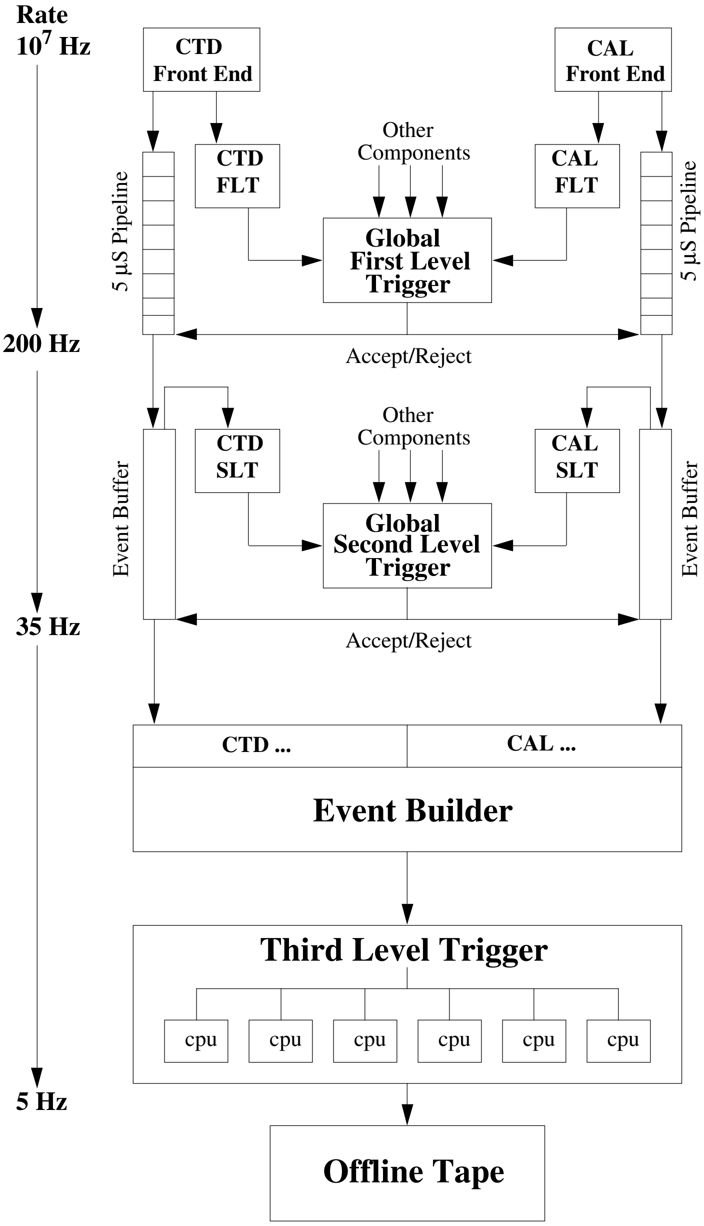

Figure 2.9: A schematic of the ZEUS trigger system.

Chapter 3

Event simulation

A Monte Carlo (MC) simulation is used to convert the measured number of events into the cross section measurement and estimate the contamination from non-charged current *ep* physics processes. In order to measure the cross section it is necessary to know the detector acceptance for the process being measured. The detector is much too complicated for an analytic calculation of the acceptance, so many simulated events are generated and fed through a software simulation of the detector. The events are then filtered using a simulation of the trigger chain, and finally reconstructed using the same offline reconstruction code as was used for the real data events. In this way the acceptance of the detector can be determined. In addition, events are generated for background *ep* physics processes so the level of contamination in the charged current candidate events can be estimated.

3.1 Signal Monte Carlo

The charged current MC events used were generated with DJANGOH 1.1 [18], which is an interface between the LEPTO 6.5.1 [21] and HERACLES 4.6.1 [19] generators. LEPTO simulates the hard scattering process between the lepton and the parton, and HERACLES simulates initial state radiation from the incoming electron, vertex and propagator corrections, and two boson exchange processes.

The ARIADNE 4.10 colour dipole model (CDM) [20] was used for the fragmentation. This model views the struck quark and proton remnant as a colour dipole which can radiate gluons. Radiated gluons can form further colour dipoles and these processes continue until all the dipoles have reached some minimum energy. Events were also generated using the MEPS fragmentation scheme of LEPTO. MEPS describes the hard scatters using the first order matrix elements of the processes and the soft higher order emissions using parton showers, where the quarks and gluons evolve by sucessive branchings until all the partons reach some minimum energy. Charged current DIS events were generated using electroweak parameters from the particle data group (PDG) [42] and the parton density function (PDF) parameterisation (see section 1.4) used was CTEQ5D [22]. The Lund string model of hadronisation was used, as implemented in JETSET 7.4 [23]

Several samples of charged current DIS MC were used with different minimum Q^2 and x cuts at the generator level. Using separate samples in this way eliminates the need to generate large numbers of low Q^2 and low x events in order to cover the HERA Q^2 and x range. The samples are then combined using weighting appropriate to the luminosity of each sample. The Q^2 and x thresholds and luminosities of the samples used are detailed in table 3.1.

MC sample	N_{gen}	σ (pb)	$\mathcal{L}$ (pb^{-1})
$Q^2 > 10$ GeV^2	24954	78.943	316
$Q^2 > 100$ GeV^2	24993	72.778	343
$Q^2 > 100$ GeV^2, $x > 0.1$	9991	28.201	354
$Q^2 > 100$ GeV^2, $x > 0.3$	4993	5.6590	882
$Q^2 > 5000$ GeV^2	14985	14.445	1037
$Q^2 > 10000$ GeV^2	10000	5.3854	1856
$Q^2 > 20000$ GeV^2	10000	1.1339	8819

Table 3.1: Summary of the charged current DIS MC samples used, where N_{gen} is the number of events generated, σ is the cross section and $\mathcal{L}$ is the integrated luminosity.

3.2 Background Monte Carlo

Several physics processes were identified as potential sources of background to the charged current DIS signal. For each process MC events were generated and put through the detector simulation in order to evaluate the amount of contamination each contributed to the measurement. Details of the background MC events that were generated are given in table 3.2.

3.2.1 Photoproduction

Photoproduction (PhP) events, where $Q^2 \sim 0$ GeV^2, can have large missing transverse momentum, and constitute a background to CC DIS, if a jet is partially or fully lost down one of the beam pipe holes in the calorimeter, or substantial energy from a jet is undetected in dead material or poorly measured in a crack between calorimeter regions. There are two photoproduction processes at leading order in QCD: direct; where the exchanged photon participates in the hard scatter; and resolved, in which the exchanged photon acts as a source of partons for the the hard scattering process. The Feynman diagrams for these processes are shown in figure 3.1. Direct and resolved photoproduction events were generated with the HERWIG [24] program. It was found that the number of events it was necessary to generate could be reduced significantly by using a filter at the generator level. The missing transverse momentum, $P_T(had)$, and total transverse momentum, $E_T(had)$, were calculated from the generator level (before the detector simulation) particles, excluding particles which would be lost in the holes in the calorimeter for the beam pipe. The events were required to have either $P_T(had) > 6$ GeV or $E_T(had) > 30$ GeV. Samples with lower thresholds in $E_T(had)$ were also generated. Figure 3.2 shows $P_T(had)$ plotted against $E_T(had)$. The events plotted were selected using the event selection detailed in chapter 5, except that no requirement on P_T/E_T was made, allowing many more photoproduction events to be plotted. It can be seen that the vast majority of the events plotted have $P_T(had) > 6$ GeV or $E_T(had) > 30$ GeV. It should be noted that the events plotted correspond to a luminosity many times that of the data.

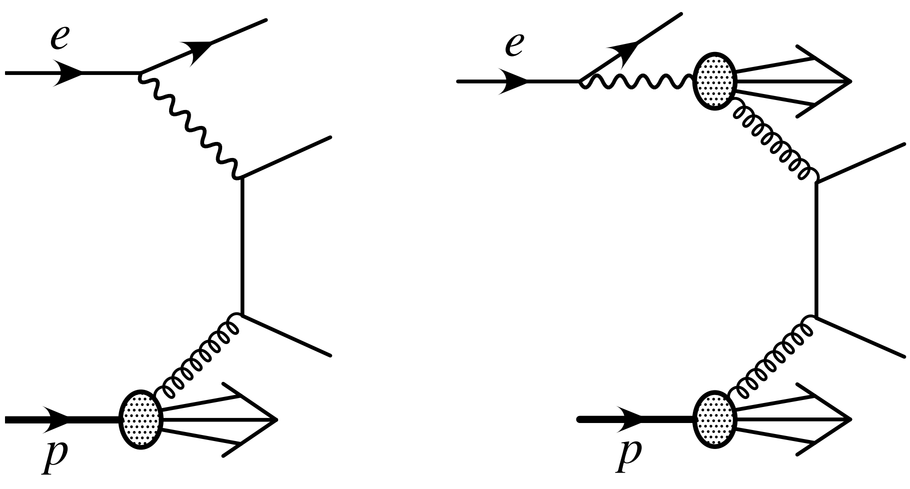

Figure 3.1: Leading order QCD Feynman diagrams for the direct and resolved photoproduction processes.

3.2.2 Neutral current DIS

Poorly measured NC DIS events can have large missing transverse momentum, and therefore constitute a background to CC DIS. In order to evaluate this background contribution NC DIS events were generated with DJANGOH.

3.2.3 Di-lepton production

Muon pair production occurs through elastic, quasi-elastic and DIS Bethe-Heitler reactions. The muons in the final state deposit only a small amount of their energy in the calorimeter, which can lead to significant missing transverse momentum in such events, and makes muon pair production a background to charged current DIS. Elastic, quasi-elastic and DIS di-muon events were generated with the LPAIR [25] generator.

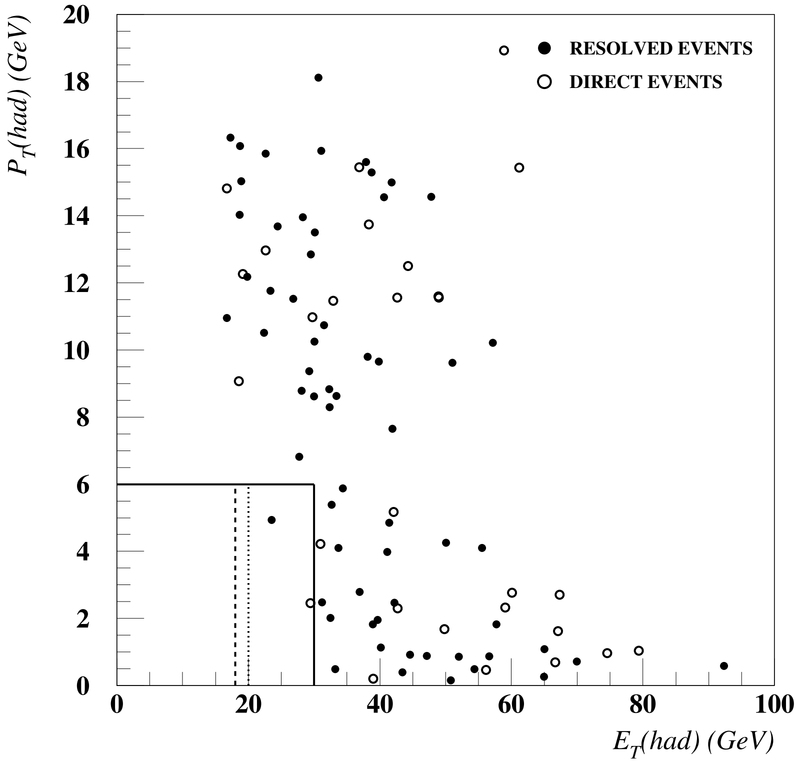

Figure 3.2: $P_T(had)$ plotted against $E_T(had)$ for photoproduction background events. It can be see that the vast majority of events have $P_T(had)$ or $E_T(had)$ above the thresholds marked at $P_T(had)$ of 6 GeV and $E_T(had)$ of 18, 20 and 30 GeV, used to filter the generated events.

Similarly tauon pair production can also consitute a background to CC DIS, since the tauons can decay to a final state with a neutrino which leads to missing transverse momentum. Elastic and DIS di-tauon events were generated with the LPAIR [25] generator.

Electron pair production does not constitute a background to CC DIS, since the electrons are well contained in the detector resulting in no significant missing transverse momentum.

3.2.4 W production

Real W bosons can be produced at HERA through the charged current and neutral current interactions:

$$e^- p \rightarrow e^- W^\pm X \tag{3.1}$$

$$e^- p \rightarrow \nu W^\pm X \tag{3.2}$$

where X represents the hadronic final state. The cross section for the neutral current reaction is expected to be an order of magnitude greater than that of the charged current process, because the charged current reaction is mediated by a W boson. The presence of a real W boson in the final state, which can decay to a lepton and a neutrino, resulting in missing transverse momentum, can make these events a background to charged current DIS. The neutral current reaction can occur through a direct process and a resolved process in an analogous way to the photoproduction reactions. MC events for the production of real W bosons through the neutral current interaction were generated using the EPVEC [26] generator, and passed through the detector simulation.

MC sample	N_{gen}	σ	$\mathcal{L}$ (pb^{-1})
Direct PhP $E_T > 18$ GeV or $P_T > 6$ GeV	99739	21.7 nb	4.6
Direct PhP $E_T > 20$ GeV or $P_T > 6$ GeV	560000	15.6 nb	35.9
Direct PhP $E_T > 30$ GeV or $P_T > 6$ GeV	240000	3.62 nb	66.3
Resolved PhP $E_T > 18$ GeV or $P_T > 6$ GeV	350000	115.6 nb	3.0
Resolved PhP $E_T > 20$ GeV or $P_T > 6$ GeV	1800000	79.2 nb	22.7
Resolved PhP $E_T > 30$ GeV or $P_T > 6$ GeV	520000	11.9 nb	43.7
NC DIS $Q^2 > 40$ GeV^2	100000	25723 pb	3.88
NC DIS $Q^2 > 100$ GeV^2	180000	8003.4 pb	22.5
NC DIS $Q^2 > 400$ GeV^2	59976	1178.8 pb	50.9
NC DIS $Q^2 > 1250$ GeV^2	24990	215.21 pb	116.1
NC DIS $Q^2 > 2500$ GeV^2	12000	71.468 pb	167.9
NC DIS $Q^2 > 5000$ GeV^2	12000	21.615 pb	555.2
NC DIS $Q^2 > 10000$ GeV^2	11960	5.377 pb	2224
NC DIS $Q^2 > 20000$ GeV^2	11997	0.851 pb	14097
NC DIS $Q^2 > 30000$ GeV^2	5995	0.187 pb	32059
NC DIS $Q^2 > 40000$ GeV^2	5998	0.0432 pb	138843
NC DIS $Q^2 > 50000$ GeV^2	6000	0.00928 pb	646552
Di-muon (DIS)	60000	63.6 pb	943
Di-muon (elastic)	40000	42.3 pb	945
Di-muon (quasi-elastic)	20000	21.4 pb	934
Di-tauon (DIS)	24920	7.91 pb	3150
Di-tauon (elastic)	50000	6.13 pb	8156
$e^-p \rightarrow e^-W^-X$ (DIS)	10000	0.406 pb	24630
$e^-p \rightarrow e^-W^-X$ (resolved)	10000	0.121 pb	82644
$e^-p \rightarrow e^-W^+X$ (DIS)	10000	0.478 pb	20920
$e^-p \rightarrow e^-W^+X$ (resolved)	10000	0.152 pb	65789

Table 3.2: Summary of the background MC samples used, where N_{gen} is the number of events generated, σ is the cross section and $\mathcal{L}$ is the integrated luminosity.

Chapter 4

Event reconstruction

The measurement of cross sections relies on the precise measurement of the kinematic variables x, y and Q^2. The kinematic variables are reconstructed from the position and energy of deposits in the calorimeter. The position where the *ep* interaction occured, the event vertex, is reconstructed in order to measure the angle of the hadronic jet, and the angle of the scattered electron in NC DIS.

4.1 Jacquet-Blondel reconstruction

The Jacquet-Blondel [27] method must be used to reconstruct the kinematic variables for charged current events, because the outgoing lepton is a neutrino, which is not detected. The missing transverse momentum, P_T, is given by

$$P_T = \sqrt{\left(\sum_i p_X^i\right)^2 + \left(\sum_i p_Y^i\right)^2} \tag{4.1}$$

and the quantity δ by

$$\delta = \sum_i (E^i - p_Z^i) \tag{4.2}$$

where the sums run over all final state particles, E^i are the measured energies and p^i are the momenta of each particle. The Jacquet-Blondel estimators of y, x and Q^2 are given by

$$Q^2_{JB} = \frac{P_T^2}{1 - y_{JB}} \tag{4.3}$$

$$y_{JB} = \frac{\delta}{2E_e} \tag{4.4}$$

$$x_{JB} = \frac{P_T^2}{s y_{JB}(1 - y_{JB})} \tag{4.5}$$

where E_e is the electron beam energy.

4.2 Electron method of reconstruction

The electron method of reconstruction [28] can be used for neutral current events. The kinematic variables x, y and Q^2 are estimated from the scattered electron energy, E'_e, and angle, θ, using the equations:

$$Q^2_e = 2E_e E'_e(1 + \cos\theta) \tag{4.6}$$

$$x_e = \frac{E_e}{E_p} \frac{E'_e(1 + \cos\theta)}{2E_e - E'_e(1 - \cos\theta)} \tag{4.7}$$

$$y_e = 1 - \frac{E'_e}{2E_e}(1 - \cos\theta) \tag{4.8}$$

4.3 Double angle method of reconstruction

The double angle method of reconstruction [28] can also be used for neutral current events. The kinematic variables x, y and Q^2 are estimated from the scattered electron angle, θ, and the angle of the hadronic jet, γ, using the equations:

$$Q^2_{DA} = 4E_e^2 \frac{\sin\gamma(1+\cos\theta)}{\sin\gamma + \sin\theta - \sin(\theta+\gamma)} \tag{4.9}$$

$$x_{DA} = \frac{\sin\theta(1-\cos\gamma)}{\sin\gamma + \sin\theta - \sin(\theta+\gamma)} \tag{4.10}$$

$$y_{DA} = \frac{E_e \sin\gamma + \sin\theta + \sin(\theta+\gamma)}{E_p \sin\gamma + \sin\theta - \sin(\theta+\gamma)} \tag{4.11}$$

4.4 Calorimeter reconstruction

A single particle produced in an interaction will shower in the calorimeter generally depositing energy in more than one calorimeter cell. A two stage clustering algorithm [29] was used to combine the information from the calorimeter cells into "islands" of energy in the calorimeter. The objective of the clustering algorithm is to combine neighbouring groups of calorimeter cells with energy into one island, ideally one that corresponds to the shower created by one particle, and in doing so remove the effect of the granularity of the calorimeter.

Before starting the clustering algorithm, fake energy deposits in the calorimeter due to noise in the electronics and the noise from radioactive decays in the uranium are removed. The method removes energy deposits of less than 140 MeV in HAC sections of the calorimeter and deposits with less than 80 MeV in EMC sections [30].

The first stage of "islanding" combines calorimeter cells that are in the same physical section of the calorimeter (FCAL, BCAL or RCAL), and the same layer (EMC, HAC1 or HAC2). Calorimeter cells with energy after the noise is removed are considered for clustering and are connected to the highest energy neighbouring cell. This is illustrated schematically in figure 4.1. The resulting two dimensional

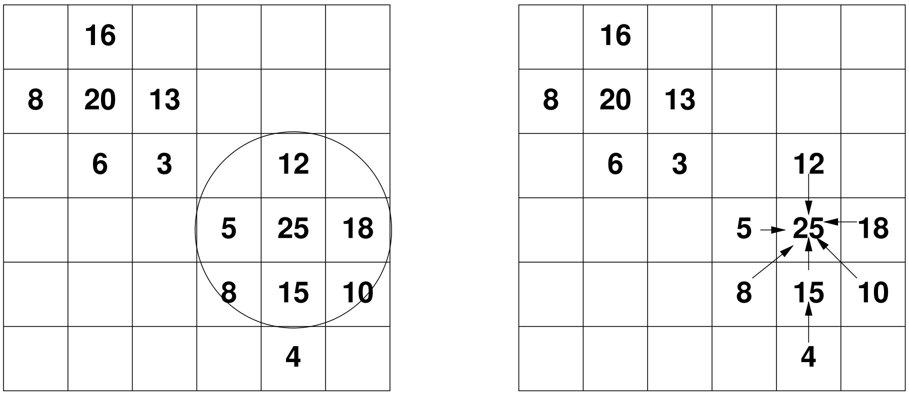

Figure 4.1: A schematic illustration of the clustering algorithm used to create cell islands. Cells are connected to the highest energy neighbouring cell.

islands are called “cell islands”, and are the input to the second stage of islanding.

The second stage of the clustering uses the azimuthal and polar angles of the cell islands to combine them into three dimensional “cone islands”. The cell islands are matched according to a probability function based on angular separation, which is derived from single pion MC events. The cell islands are combined from the outside, inwards. So HAC2 islands are matched first with HAC1 and then HAC1 with EMC. EMC islands can also be matched with other EMC islands. Cell islands in different calorimeter sections can also be combined, so that a single island is created for a particle that struck the boundary between two calorimeter sections.

The calorimeter islands are corrected for several different effects. The first is the effect of energy deposits far from the real direction of the particle. These deposits are caused by backsplash from the calorimeter and scattering and showering in material between the interaction point and the calorimeter. These deposits can cause an over estimation in γ at the low end of the spectrum. A method to remove these deposits is described in [31]. The method removes low energy islands (<3 GeV) if the event has a hadronic angle greater than a threshold, γ_{max}, which is itself a function of the hadronic angle and is derived from a fit to NC DIS MC. The fit for γ_{max} removes as many backsplash islands as possible without removing more than 1% of non-backsplash islands, and is shown in figure 4.2. This correction process is iterated until the difference between successive iterations of the hadronic angle is less than 1%.

Energy loss in uninstrumented material between the interaction point and the calorimeter is also considered. A map of the dead material taken from the MC simulation of the detector is used to correct the measured energies of the calorimeter islands, in both data and MC. The dead material map is shown in figure 4.3.

The improvement of the measured x, y and Q^2 after the corrections described above can be seen in figures 4.4, 4.5 and 4.6, where the bias and resolution estimated from the MC simulation is shown, for the Jacquet-Blondel estimators of Q^2, x and y. The bias is defined, for example for the Q^2 estimator, as

$$\frac{Q^2 - Q^2_{TRUE}}{Q^2_{TRUE}} \tag{4.12}$$

where Q^2 is the Jacquet-Blondel estimator and Q^2_{TRUE} is the generated value of Q^2. The resolution of the estimator is the rms of the distribution of the biases. Figure 4.4 shows the bias and resolution of the corrected and uncorrected Jacquet-Blondel estimator for Q^2. It can be seen that the bias for the uncorrected estimator is ~20%, whereas the bias is typically less than 5% after correction. The resolution for both corrected and uncorrected estimators is found to be ~20%. The corresponding quantities for the x estimator are shown in figure 4.5. Again the bias is improved from around 20% to a few percent by the corrections and the resolution remains roughly constant at values of 15% at high x to 25% at the lowest values of x. The effect of removing islands due to backsplash is clearly shown in figure 4.6, where the bias and resolution of the Jacquet-Blondel estimator of y are shown before and after correction. A bias of up to 25% at low y in

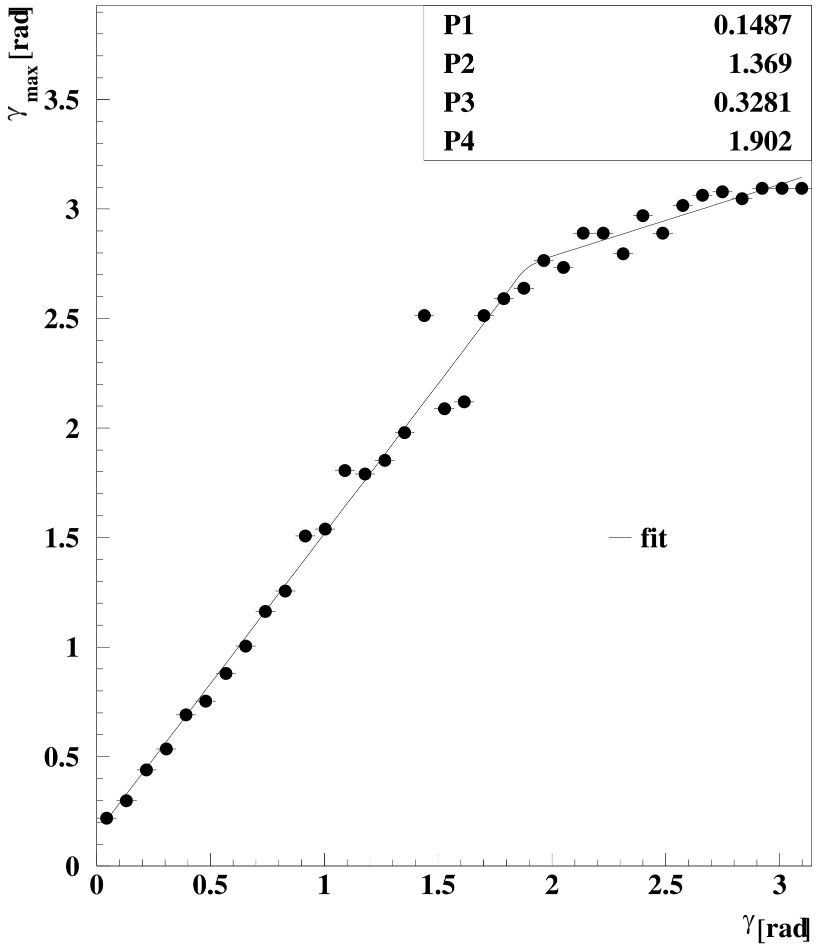

Figure 4.2: The fit to NC DIS MC events for γ_{max} as a function of γ, used in the removal of backsplash islands [31].

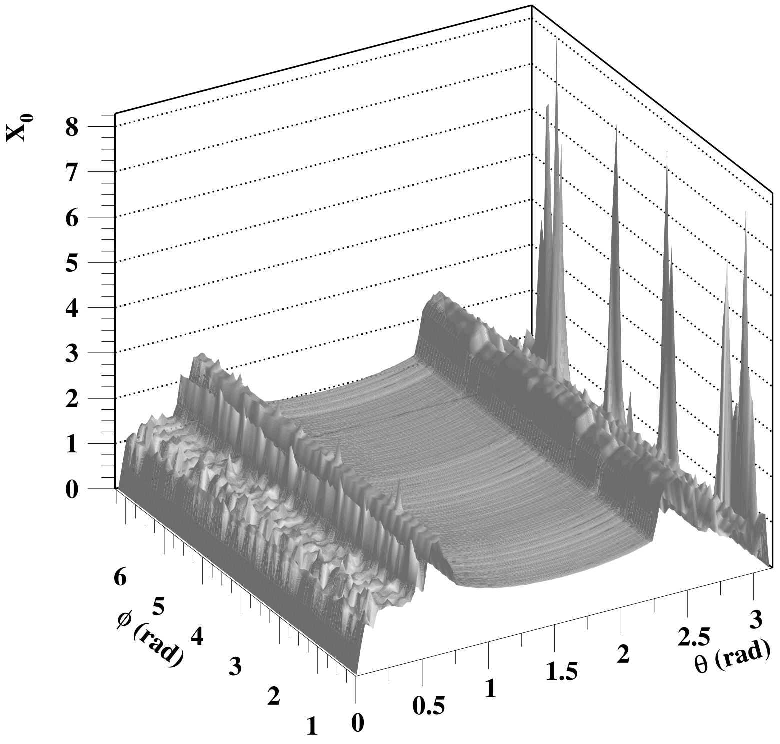

Figure 4.3: The dead material map taken from the MC detector simulation. The amount of inactive material between the centre of the detector and the CAL is shown in radiation lengths (X_0) as a function of polar angle, θ, and azimuthal angle, ϕ.

the uncorrected value is reduced to $< 5\%$ by the correction. Similarly a bias of 10-15% at higher y is reduced to 1-2%. The resolution is 15% at low y decreasing to ∼10% at higher y.

Neutral current events can be used to check the corrections made to the measured energies. By comparing the double angle method estimators, which are independent of the measured energy, with the Jacquet-Blondel estimators, which come only from the hadronic final state, the improvement can be measured without relying on Monte Carlo simulation. The double angle transverse momentum can be obtained using,

$$P_{TDA} = \sqrt{Q^2_{DA} \cdot (1 - y_{DA})} \tag{4.13}$$

and then compared with the measured transverse momentum. Figure 4.7 (a) shows that the double angle transverse momentum is unbiased and has resolution of $\sim 5\%$. Figure 4.7 (b) shows the bias of the measured hadronic transverse momentum, P_{Th}, relative to P_{TDA}. It can be seen that P_{Th} agrees with P_{TDA} to within 2%, and the systematic shift between data and MC is $< 2\%$. Figure 4.7 (c) shows the resolution of the measured hadronic transverse momentum relative to P_{TDA}. It can be seen that the P_{Th} resolution is $\sim 10\%$, and is simulated well in MC to an accuracy of $\sim 1\%$.

4.5 Interaction vertex reconstruction

Using the CTD it is possible to reconstruct the interaction vertex position from the measured tracks. Tracks are fitted to give a primary vertex and a number of secondary vertices. The primary vertex fit includes the position of the beam line as a constraint. The fitting method is detailed in [32]. The objective of the multi-vertex fitting is to provide a good measurement of the primary vertex. An important bias when fitting only the primary vertex can come from events in

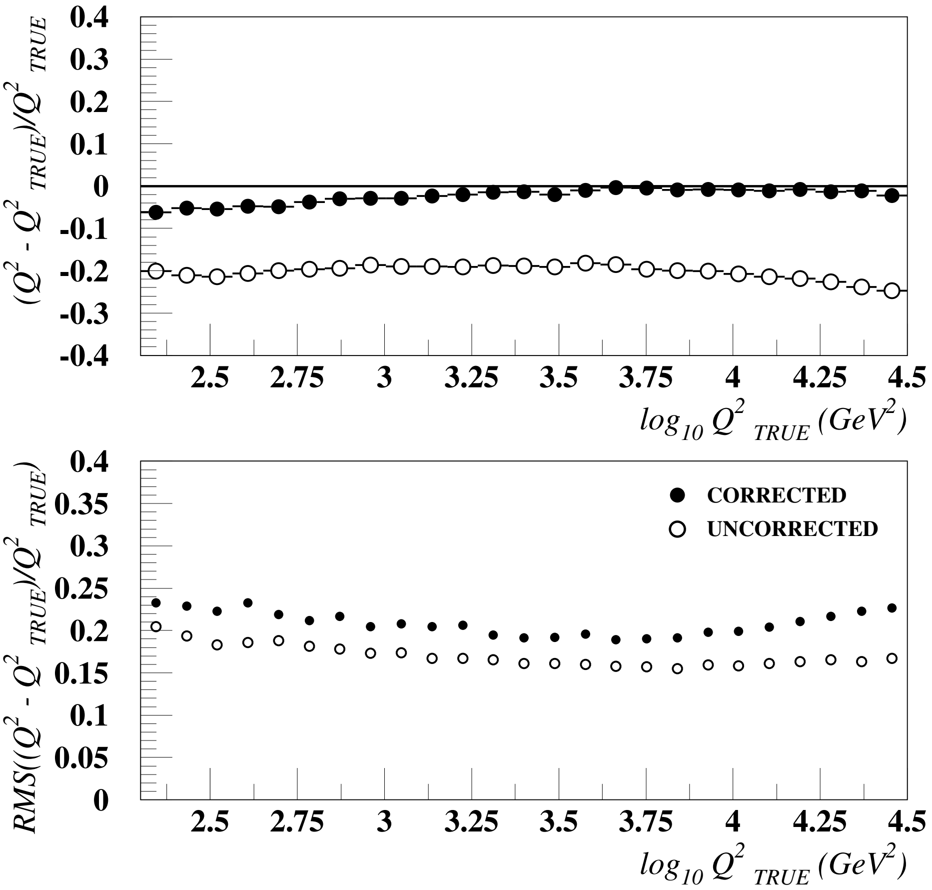

Figure 4.4: The bias (top) and resolution (bottom) from MC is shown for the corrected and uncorrected Jacquet-Blondel estimators of Q^2.

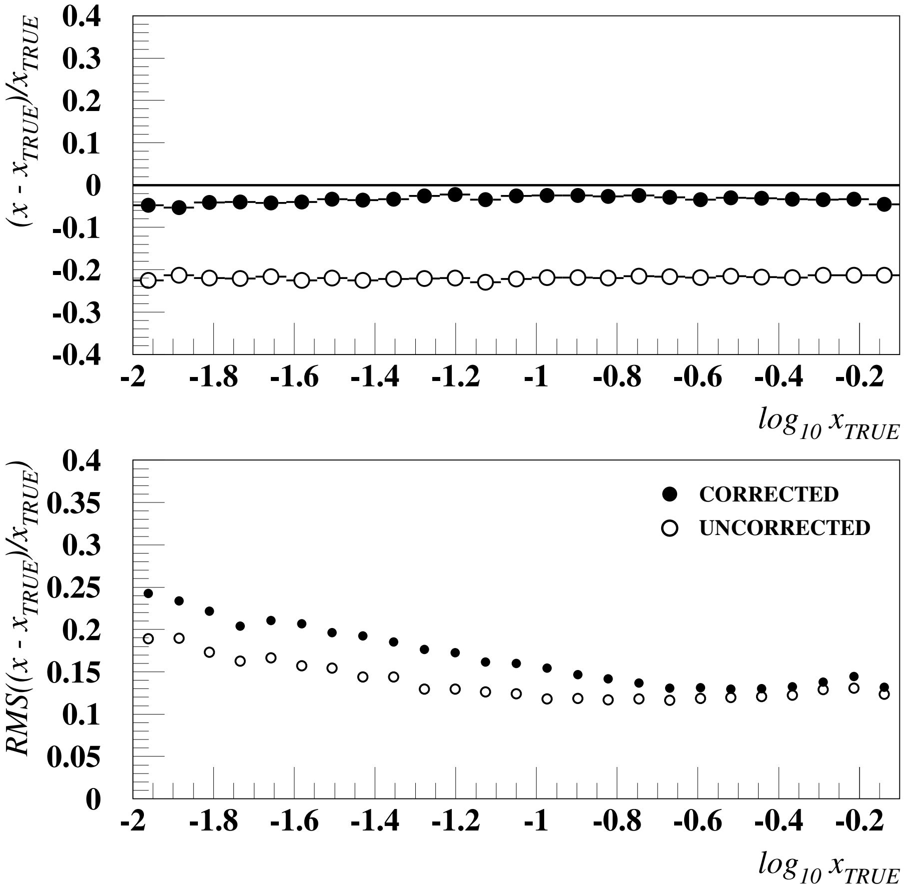

Figure 4.5: The bias (top) and resolution (bottom) from MC is shown for the corrected and uncorrected Jacquet-Blondel estimators of x.

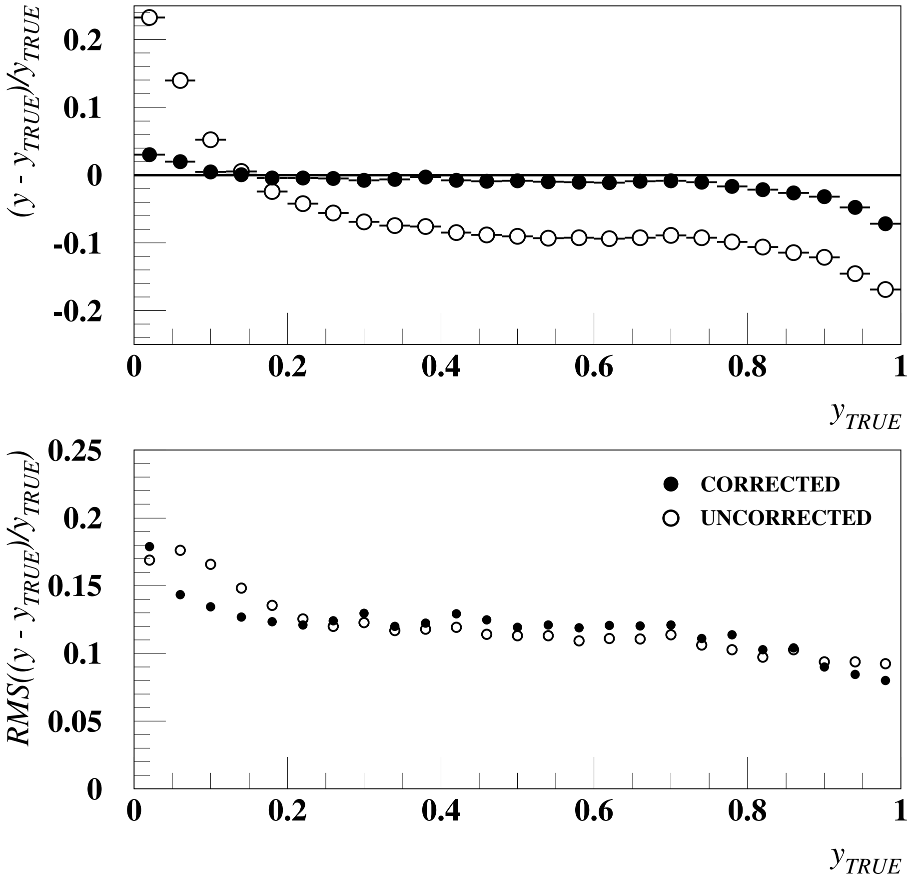

Figure 4.6: The bias (top) and resolution (bottom) from MC is shown for the corrected and uncorrected Jacquet-Blondel estimators of y.

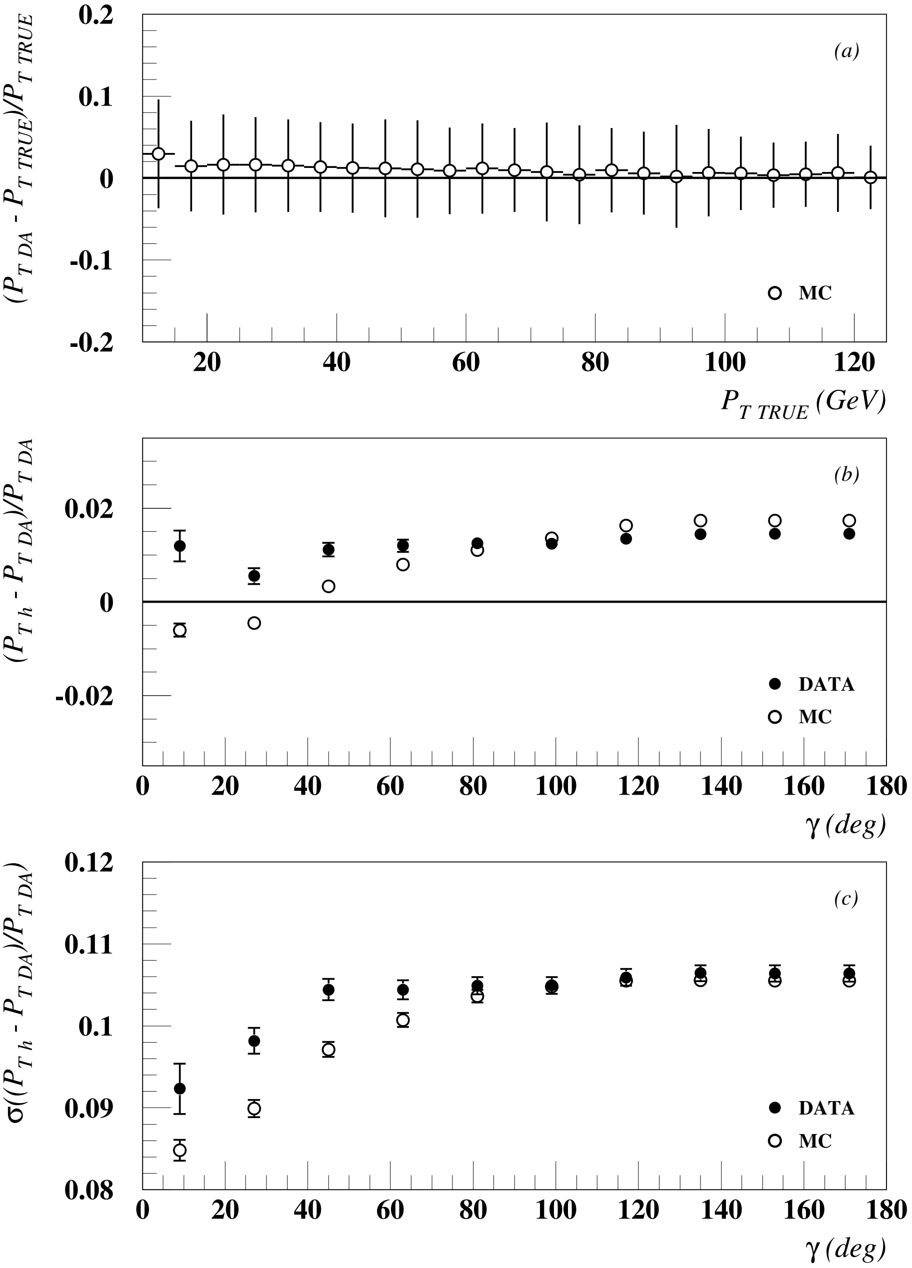

Figure 4.7: The bias of the double angle estimator for hadronic P_T from MC events is shown in figure (a). Figure (b) shows the bias of the measured hadronic transverse momentum, P_{Th}, relative to P_{TDA}, for data (closed circles) and MC (open circles). Figure (c) shows the resolution of the measured hadronic transverse momentum relative to P_{TDA}, for data (closed circles) and MC (open circles).

which the hadronic jet interacts with material in the beam pipe, producing many tracks pointing to the interaction in the beam pipe rather then the *ep* interaction. By also fitting secondary vertices this bias in the primary vertex is removed. The distribution of the number of vertices found is shown in figure 4.8, for data and MC events after the selection detailed in chapter 5. It can be seen that the number of vertices found is a little larger for data events than MC events. The underlying distribution of the Z coordinate of the interaction vertex is measured in an unbiased way from NC DIS events [33], and the MC events are generated according to the measured vertex distribution. For charged current events the Z position resolution for the interaction vertex is ∼1 cm. For neutral current events the presence of a high P_T scattered electron track improves the resolution of the Z position of the interaction vertex to ∼0.15 cm. The distribution of the Z position of the interaction vertex is shown in figure 4.8 for data and MC after the selection detailed in chapter 5 has been applied. It can be seen that the data distribution is well described by MC.

As mentioned in an earlier section the calorimeter provides accurate timing information for each cell with energy deposited in it. This timing information can be used to determine the Z coordinate of the interaction vertex, for events with a hadronic jet at low angle. The method, described in [34], uses the timing for each electron and proton bunch from the C5 detector, and the timing measurements from cells in FCAL to estimate the Z coordinate of the interaction vertex. NC DIS events are used to calibrate the cell timing on a run by run basis in the data. The calorimeter timing is not well simulated in the MC events, so the resolution of the vertex measurement in data is parameterised as a function of the number of cells in FCAL used and the generated MC vertex is smeared by this function. The resolution is found to be ∼10 cm for events with greater than 10 GeV deposited in FCAL. In figure 4.10 the distribution of the Z coordinate of the interaction vertex, reconstructed using the timing information of energy deposits, is compared for data and MC for the final candidate events selected using the

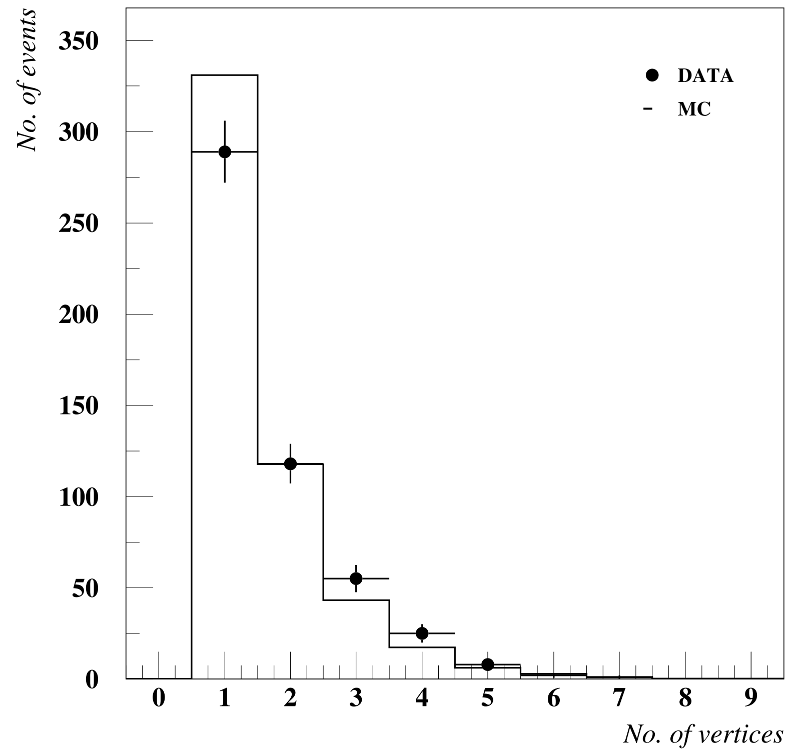

Figure 4.8: Distribution of the number of vertices found by the CTD, for data (closed circles) and MC (histogram) for charged current candidate events.

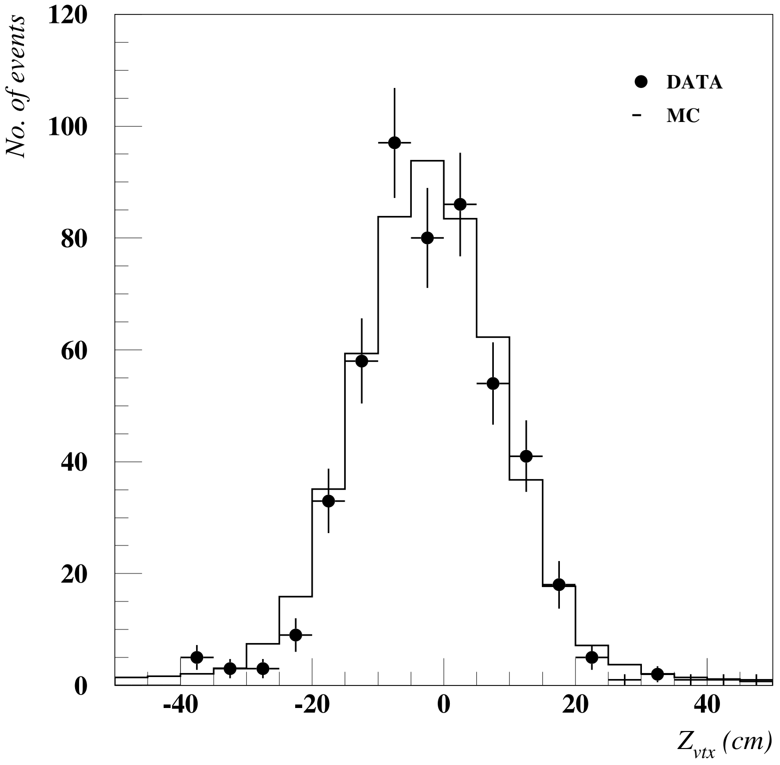

Figure 4.9: Distribution of the Z position of the interaction vertex found by the CTD, for data (closed circles) and MC (histogram) for charged current candidate events.

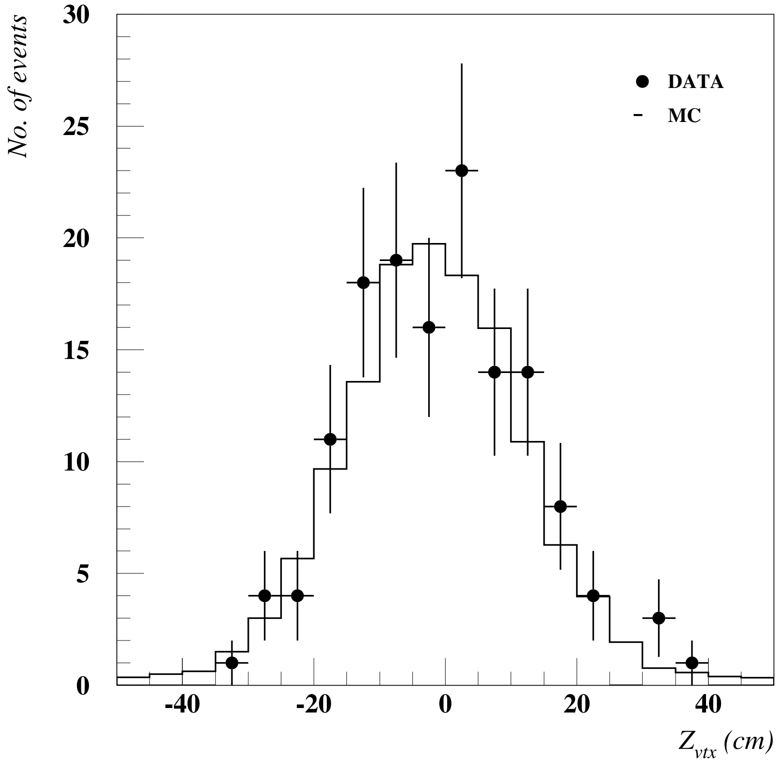

Figure 4.10: Distribution of the Z position of the interaction vertex reconstructed using the timing information of energy deposits, for data (closed circles) and MC (histogram) for charged current candidate events.

requirements detailed in chapter 5. It can be seen that the data distribution is well described by MC.

The efficiency of the CTD vertex reconstruction decreases significantly at low angles of the hadronic jet. Events that deposit energy at very forward angles in the FCAL, populate the area of high x and low y in the kinematic phase space, shown in figure 4.11, between γ of 5° and 25°. In order to increase the phase space available for the cross section measurements, charged current candidate events are split into two classes according to the angle of the hadronic jet calculated

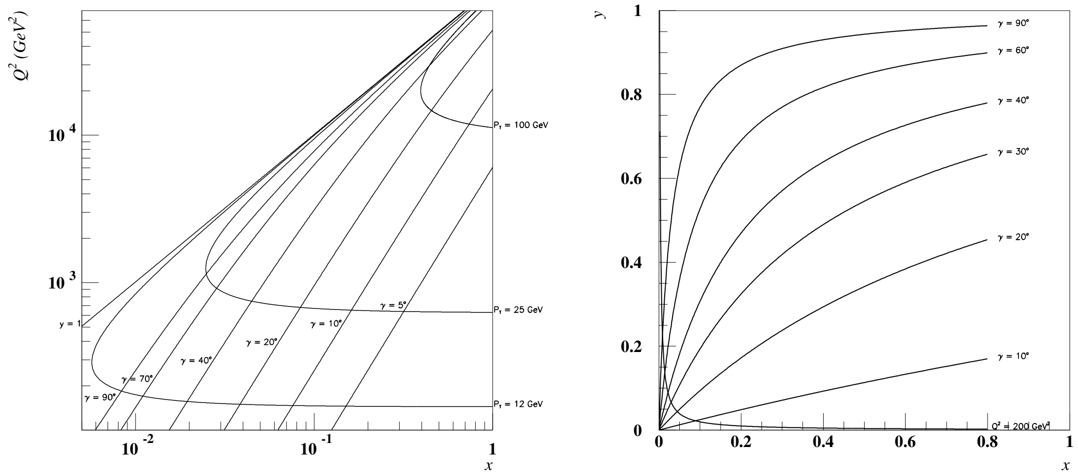

Figure 4.11: The xQ^2 plane is shown with isolines of γ and P_T (left) and the xy plane with isolines of γ (right). It can be seen that an additional area of kinematic phase space at high x and low y is made available through the use of calorimeter timing to measure the interaction vertex for events with $\gamma < 23°$.

assuming zero for the vertex position, γ_0. Those events with $\gamma_0 > 0.4$ radians ($\sim 23°$) are within the acceptance of the CTD, and therefore the CTD tracks can be used to reconstruct the interaction vertex position with high efficiency. Candidate events with $\gamma_0 < 0.4$ radians are typically too far forward to ensure that the CTD vertex is reconstructed efficiently and with no bias, because there are few or no tracks reconstructed. For these events the arrival time of energy deposits in the FCAL is used to reconstruct the Z position of the interaction vertex. In figure 4.12 the vertex reconstruction method used is compared for data and MC for the final candidate events selected using the requirements detailed in chapter 5. It can be seen that the partition of events between high and low γ_0 in the data is well reproduced by the MC simulation.

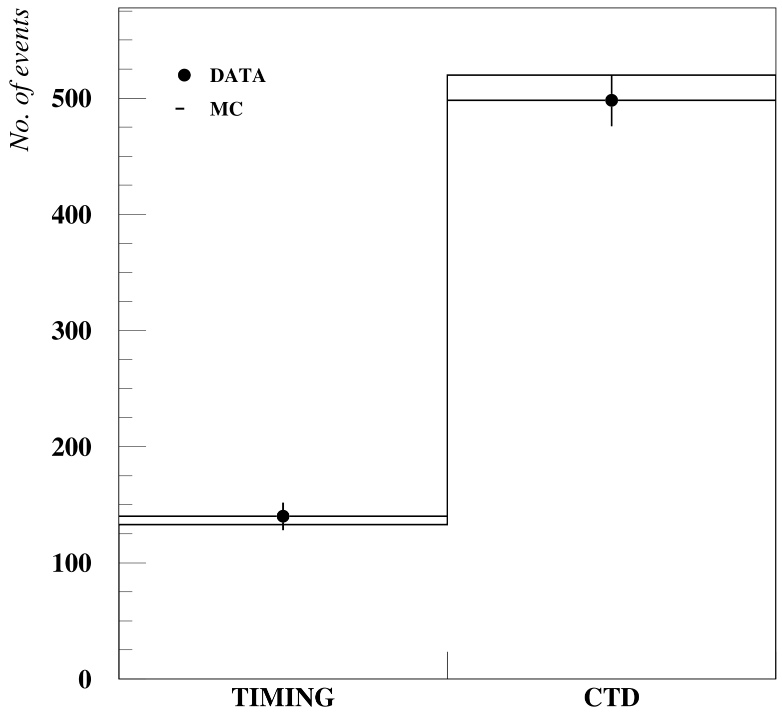

Figure 4.12: Comparison of vertex reconstruction method for data (closed circles) and MC (histogram).

Chapter 5

Event selection

In order to measure the charged current DIS cross sections it is necessary to select charged current candidate events with high acceptance and as small an amount of background contamination as possible from the large amount of data taken. The characteristic signature of charged current DIS events is missing transverse momentum, P_T, measured in the detector, due to an outgoing neutrino which escapes undetected. Charged current events are selected by requiring that candidate events have missing transverse momentum at each level of the trigger and finally a more stringent selection is applied to the events offline.

5.1 The charged current trigger

The ZEUS trigger system is described in section 2.2.7. The first level trigger (FLT) conditions reject the bulk of background from protons interacting outside the detector using the time measurement made from the energy deposits in the upstream veto counters. Charged current candidate events are required to satisfy at least one of:

- $P_T \geq 5$ GeV and $E_T \geq 5$ GeV together with several tracks found in the CTD.
- $P_T \geq 8$ GeV together with several tracks found in the CTD.

- $P_T \geq 8$ GeV together with at least 10 GeV of energy in FCAL.

where the total transverse energy, E_T, is defined as:

$$E_T = \sum_i \sqrt{(p^i_X)^2 + (p^i_Y)^2}$$

where the sums run over calorimeter cells. At the FLT, the calorimeter cells closest to the beam pipe hole are excluded from the sum used to calculate E_T. This means the first branch takes events in the centre of the calorimeter with a relatively low P_T threshold. The second branch with no E_T requirement has a higher P_T threshold of 8 GeV. The final branch is for very forward events, so no tracking information is required but at least 10 GeV must be deposited in the FCAL. This combination of trigger branches maintains a high acceptance for CC DIS events, while keeping the trigger rate reasonably low.

The second level trigger uses the measured times of energy deposits in the calorimeter to remove background events for which the timing of the deposits is not consistant with an *ep* interaction from a HERA bunch crossing. Charged current candidate events are accepted if at least one of the following conditions is satisfied.

- $P_T > 6$ GeV and E_T (excluding the two rings of cells closest to the forward beam pipe) > 6 GeV and at least one track fitted to a vertex found in the CTD.
- $P_T > 9$ GeV and P_T (excluding the cells adjacent to the forward beam pipe) > 8 GeV and at least 20 GeV of energy in FCAL.
- $P_T > 9$ GeV and $P_T/\sqrt{E_T} > 2.1$ GeV$^{\frac{1}{2}}$ and at least 80 GeV of energy in FCAL.
- $\delta > 6$ GeV and $P_T^2 > 2.25 \cdot E_T$ GeV^2 and at least one track fitted to a vertex found in the CTD.

In the second level trigger, the parallel nature of the processing means that the track fitting and vertex finding are done at the same time as the calorimeter deposits are reconstructed. This means that the P_T and E_T must be calulated using the nominal interaction position for the vertex.

The full event information is available to the third level trigger. Tighter timing cuts in addition to algorithms to remove proton interactions with gas in the beam pipe are applied. Charged current candidate events are required to satisfy at least one of the following conditions.

- $P_T > 6$ GeV and a CTD vertex found
- $P_T > 8$ GeV and at least 10 GeV of energy in FCAL for events with no vertex fitted tracks

5.2 Backgrounds

Background events to the charged current DIS signal can be split into two catagories, *ep* interactions and non-*ep* interactions. The main sources of background events are listed below:

5.2.1 Non-*ep* background events

- Beam gas events, where the proton or electron beam interacts with residual gas in the beam pipe. Typically these events have high track multiplicity and high activity in the calorimeter. The amount of contamination from these events can be estimated using events from pilot bunches (see section 2.1).
- Cosmic shower muon events, where muons produced in the upper atmosphere penetrate the detector, can result in missing transverse momentum when the muon loses energy while passing through the detector.

- Halo muon events, where muons are produced upstream of the detector by interactions between one of the particle beams and some part of the accelerator. These muons travel through the detector parallel to the beampipe and deposit energy in the calorimeter, resulting in missing transverse momentum.

5.2.2 *ep* background events

The amount of contamination from *ep* background events is estimated using the MC samples. See chapter 3.

- Photoproduction events, where Q^2 is close to zero, can have missing transverse momentum because part of the hadronic final state is lost down one of the holes in the calorimeter for the beam pipe or in a crack between calorimeter sections, and is not detected.

- Poorly measured neutral current DIS events can be a background to the charged current DIS signal. Events in which the scattered electron or jet hits a crack between calorimeter sections, or in which part of the hadronic jet is lost down one of the holes in the calorimeter for the beam pipe, can have missing transverse momentum.

5.3 High γ_0 selection

Events with a hadronic angle, calculated with reference to the nominal interaction point, γ_0, greater than 0.4 radians are required to satisfy the following criteria.

- P_T >12 GeV
  Missing transverse momentum, P_T, due to the momentum of the undetected neutrino, is the primary characteristic of charged current *ep* events. Figure 5.1 (left) shows the distribution of P_T for data and MC events, after all other cuts. It can been seen that the MC describes the data distribution well.

- $P_T(-ir)$ >10 GeV

  where $P_T(-ir)$ is the transverse momentum evaluated excluding the cells adjacent to the forward beam pipe. This cut removes beam gas events which deposit energy in cells adjacent to the beam pipe. Figure 5.1 (right) shows the distribution of $P_T(-ir)$ for data and MC events, after all other cuts have been applied. It can been seen that the MC describes the data distribution well.

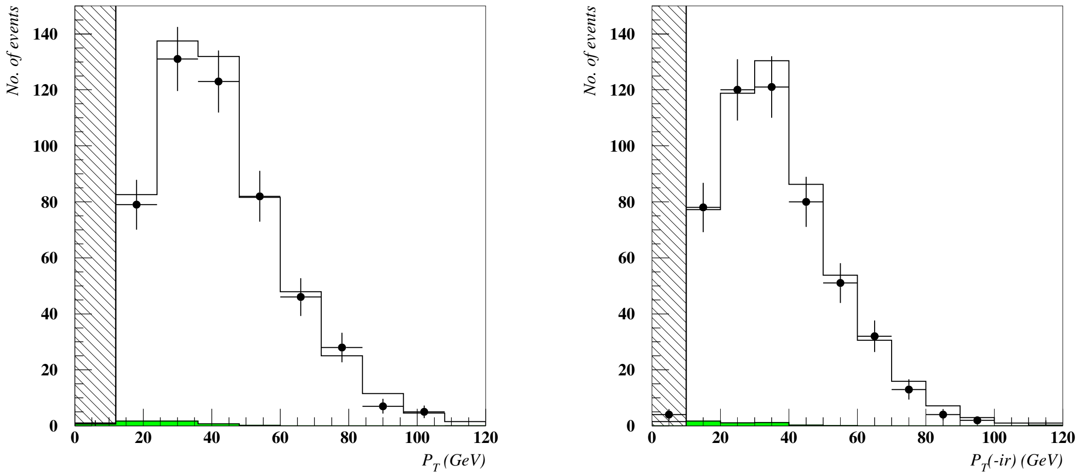

Figure 5.1: Distributions of total P_T (left), and P_T excluding the inner ring of cells in FCAL, $P_T(-ir)$, (right), for high γ_0 events after all other cuts have been applied. The data events are shown as closed circles, the sum of signal and background MC as the open histogram, and the background contribution is shown by the shaded histogram. The shaded areas shows those events that pass all other cuts but are rejected by the P_T or $P_T(-ir)$ cut.

- P_T/E_T >0.5 for $P_T < 30$ GeV

  The quantity P_T/E_T characterises how collimated the transverse energy flow is. Requiring a highly collimated, or single jet-like event, reduces backgound from beam gas interactions and photoproduction. No requirement is made for high P_T events, where background contamination is small, in order to improve the acceptance for dijet charged current DIS events. Figure 5.2

shows the P_T/E_T distributions for $P_T < 30$ GeV (left) and $P_T > 30$ GeV (right), for data and MC events after all other cuts have been applied.

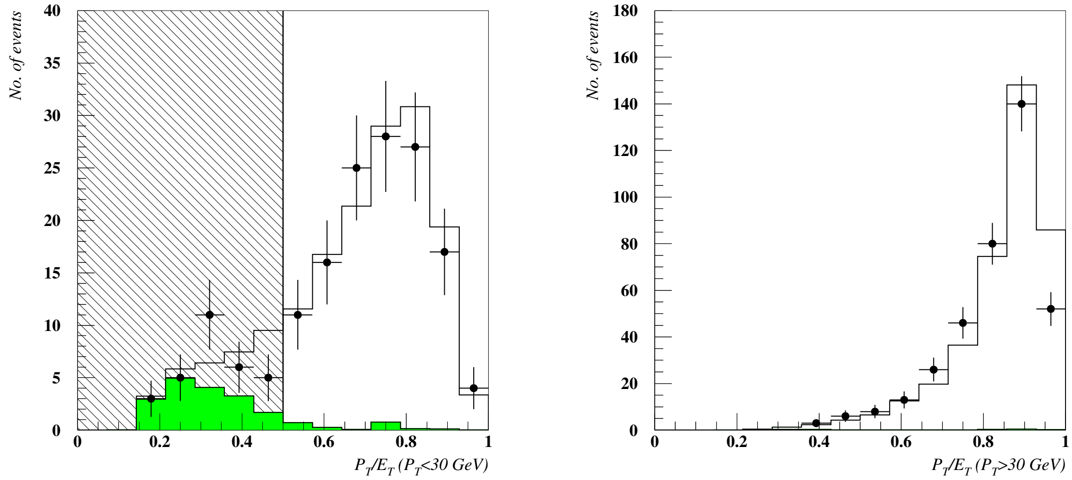

Figure 5.2: Distribution of P_T/E_T for $P_T < 30$ GeV (left) and $P_T > 30$ GeV (right), for high γ_0 events after all other cuts have been applied. The data events are shown as closed circles, the sum of signal and background MC as the open histogram, and the background contribution is shown by the shaded histogram. The shaded area shows those events that pass all other cuts but are rejected by the P_T/E_T cut.

- -50 cm $< Z_{vtx} <$ 50 cm

  The Z position of the *ep* interaction vertex, measured by the CTD, is required to be within 50 cm of the nominal interaction point at $Z = 0$ cm. Confining the vertex to the central region of the detector helps to reject non-*ep* interactions and insures the events have been well reconstructed. Figure 5.3 shows the distribution of the Z coordinate of the interaction vertex for data and MC.

- $N_{good} \geq 1$

  where N_{good} is the number of good tracks. A good track is defined as a vertex fitted track with $P_T >0.2$ GeV which passes within 1.5 cm of the nominal

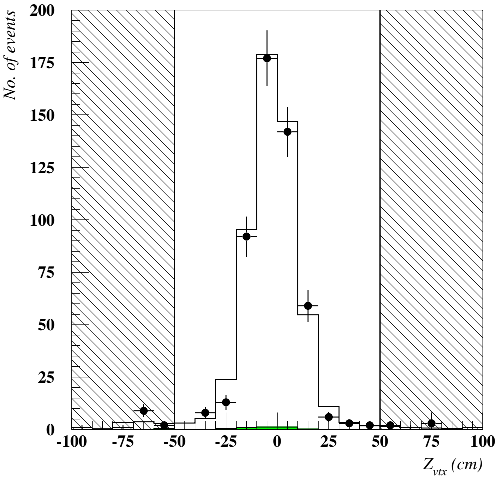

Figure 5.3: Distribution of the Z position of the ep interaction vertex measured by the CTD for high γ_0 events. The data events are shown as closed circles, the sum of signal and background MC as the open histogram, and the background contribution is shown by the shaded histogram. The shaded areas show those events that pass all other cuts but are rejected by the Z vertex position cut. In the unshaded region there is good agreement between data and MC.

beam line, and has polar angle in the range 15° to 164°. Requiring at least one good track reduces background from non-*ep* interactions. Figure 5.4 shows the distribution of N_{good} for data and MC after all other cuts have been applied.

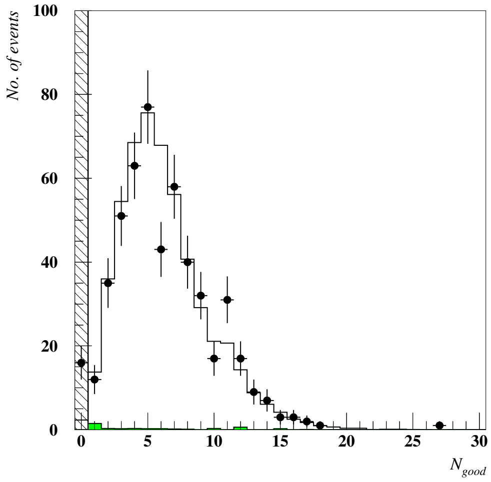

Figure 5.4: Distribution of good track multiplicity, after all other cuts have been applied. The data events are shown as closed circles, the sum of signal and background MC as the open histogram, and the background contribution is shown by the shaded histogram. The shaded area shows those events that pass all other cuts but are rejected by the good track multiplicity cut. In the unshaded region there is generally good agreement between data and MC.

- $N_{good} > 0.25(N_{trks} - 20)$ for $P_T > 30$ GeV

  $N_{good} > (N_{trks} - 5)$ or $N_{good} > 10$ for $P_T < 30$ GeV

  where N_{trks} is the number of particle tracks. A large fraction of the tracks reconstructed in an event are required to be good tracks. The number of beam gas background events is reduced since beam gas events are characterised by a large number of non-vertex tracks. Figure 5.5 shows the scatter plots of N_{good} versus N_{trks} for charged current MC events and high P_T data events. By comparing (a) and (b) it can be seen that beam gas events populate the region of high N_{trks} and low N_{good}. Figures 5.5 (c) and (d) show that the number of beam gas background events is small for events with $P_T > 30$ GeV, and the cut made is illustrated by the lines. Figures 5.5 (e) and (f) show that there is significant contamination from beam gas backgound for $P_T < 30$ GeV, so a tighter cut is applied to events with P_T <30 GeV with less than 10 good tracks.

- $E_{BHAC}/E_{BCAL} <\ 0.9$ for $E_{BCAL} > 2$ GeV
  where E_{BHAC} is the energy measured by the HAC cells in BCAL, and E_{BCAL} is the total energy measured in BCAL. This cut requires that the energy deposited in BCAL must not be entirely hadronic. Halo muons and cosmic rays which miss the EMC layer, but pass through the HAC cells are removed. Since genuine *ep* interactions will produce particles which must pass through the EMC layer before the HAC cells, these interactions will not be purely hadronic. Figure 5.6 shows the distribution of E_{BHAC}/E_{BCAL} for data and MC after all other cuts have been applied.

- $|\Delta\Phi|$ <0.5 radians for $P_T < 30$ GeV
  $|\Delta\Phi|$ <2.0 radians for for $P_T > 30$ GeV
  $\Delta\Phi$ is the difference between the azimuthal angles of the missing P_T calculated from the tracks measured in the CTD and calculated using the energy deposited in the calorimeter. For charged current events these two angles should agree quite closely. This requirement is effective in removing halo and cosmic muon events. Figure 5.7 shows the distributions of $\Delta\Phi$ for events with $P_T < 30$ GeV (left) and events with $P_T > 30$ GeV (right).

- Photoproduction rejection
  Photoproduction events, where the scattered electron is lost down the rear beam pipe, can be poorly measured resulting, in high missing transverse momentum. These events, a background to the charged current DIS signal, are characterised by two hadronic jets that are in opposite directions in azimuth. Tracks fitted to the vertex are used to identify such events by their topology and reject them [35].

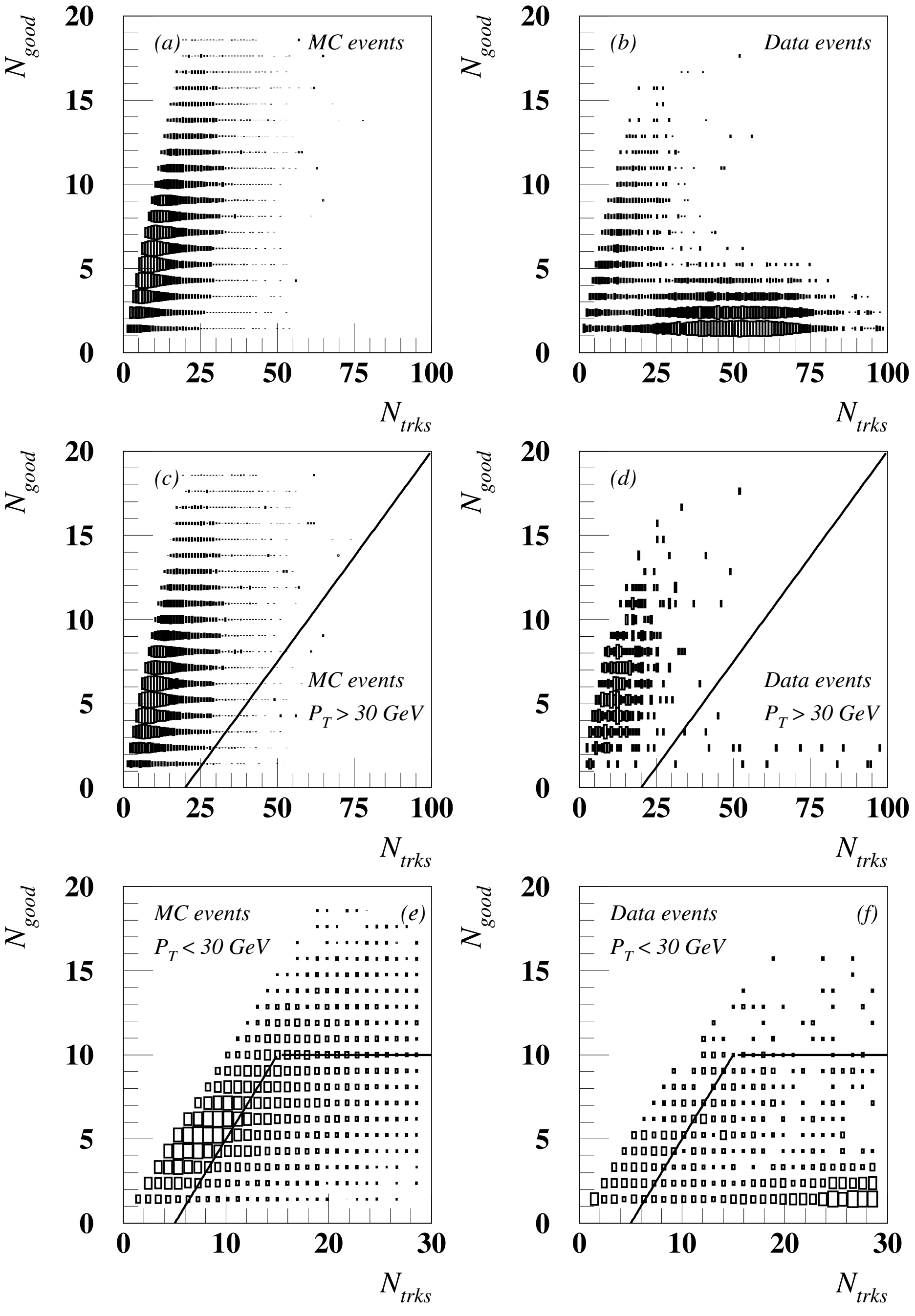

Figure 5.5: The number of good tracks is plotted against the total number of tracks separately for (a) all MC events; (b) all data events; (c) MC events with $P_T > 30$ GeV; (d) data events with $P_T > 30$ GeV; (e) MC events with $P_T < 30$ GeV and (f) data events with $P_T < 30$ GeV.

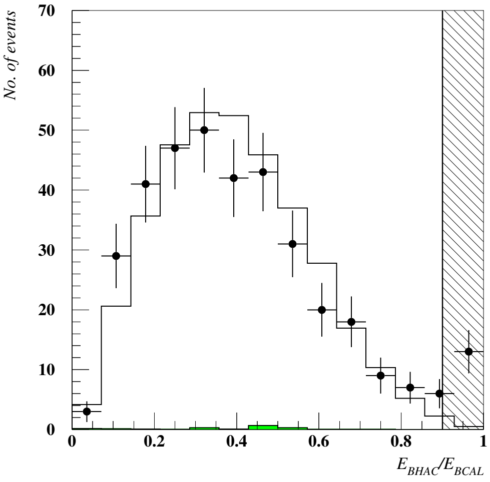

Figure 5.6: Distribution of E_{BHAC}/E_{BCAL}, for the high γ_0 charged current event sample after all other cuts have been applied. The shaded area shows those events that pass all other cuts but are rejected by the E_{BHAC}/E_{BCAL} cut. The data events are shown as closed circles, the sum of signal and background MC as the open histogram, and the background contribution is shown by the shaded histogram. In the unshaded region there is generally good agreement between data and MC.

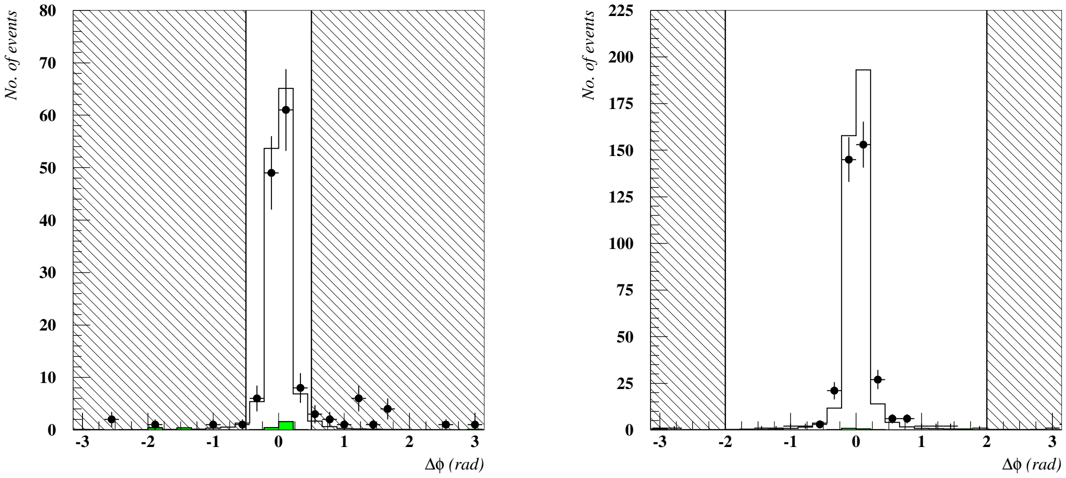

Figure 5.7: Distribution of $\Delta\Phi$, for the high γ_0 charged current event sample after all other cuts have been applied. The distributions for $P_T < 30$ GeV (left) and $P_T > 30$ GeV (right) are shown. The data events are shown as closed circles, the sum of signal and background MC as the open histogram, and the background contribution is shown by the shaded histogram. The shaded areas show those events that pass all other cuts but are rejected by the $\Delta\Phi$ cuts. In the unshaded regions there is generally good agreement between data and MC.

5.4 Low γ_0 selection

Events with a hadronic angle, calculated with reference to the nominal interaction point, γ_0, less than 0.4 radians are required to satisfy the following criteria.

- P_T >25 GeV

  The P_T threshold is increased to 25 GeV. This is necessary since there is no tracking information available to use to reject background events. Figure 5.8 (left) shows the distribution of P_T for data and MC, after all other cuts have been applied.

- $P_T(-ir)$ >25 GeV

  Similarly the threshold for P_T excluding the inner ring of cells in FCAL is increased because there is no tracking information available for background rejection. Figure 5.8 (right) shows the distribution of $P_T(-ir)$ for data and MC, after all other cuts have been applied. The large number of data events removed by this cut was found to be consistent with the estimate of the beam gas background from the study of pilot bunch events.

- -50 cm < Z_{vtx} < 50 cm

  The Z position of the *ep* interaction vertex, measured from the timing of energy deposits in FCAL, is required to be within 50 cm of the nominal interaction point at $Z = 0$ cm. Figure 5.9 shows the distribution of the Z position of the interaction vertex, measured from the timing of energy deposits in the calorimeter, for data and MC events after all other cuts have been applied. It can be seen that the data distribution is well described by the MC events.

5.5 Neutral current DIS rejection

Neutral current DIS events with poorly measured electron or hadronic energy can have high transverse momentum. Selection cuts are applied, to identify and

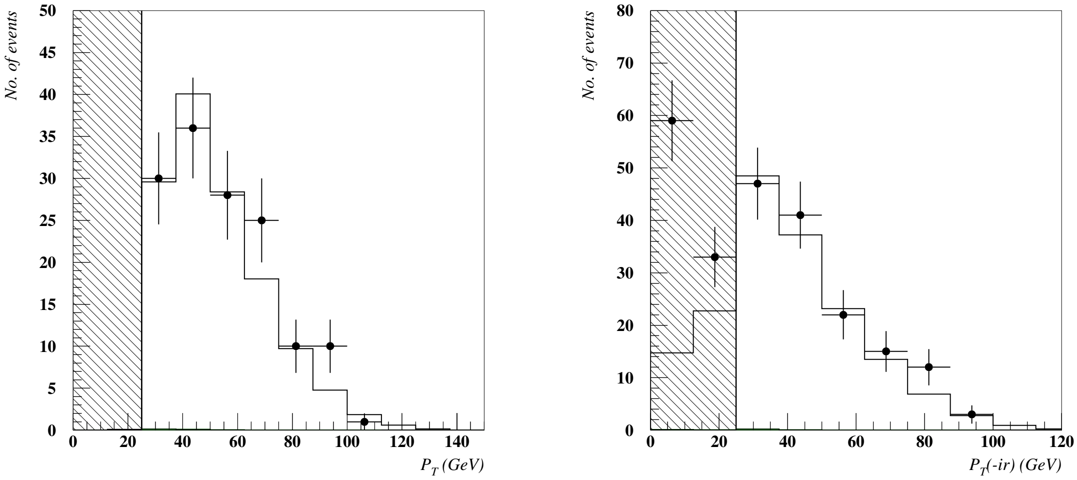

Figure 5.8: Distributions for total P_T (left), and P_T excluding the inner ring of cells in FCAL (right), for low γ_0 events after all other cuts have been applied. The data events are shown as closed circles, the sum of signal and background MC as the open histogram, and the background contribution is shown by the shaded histogram. The shaded areas show those events that pass all other cuts but are rejected by the P_T or $P_T(-ir)$ cut.

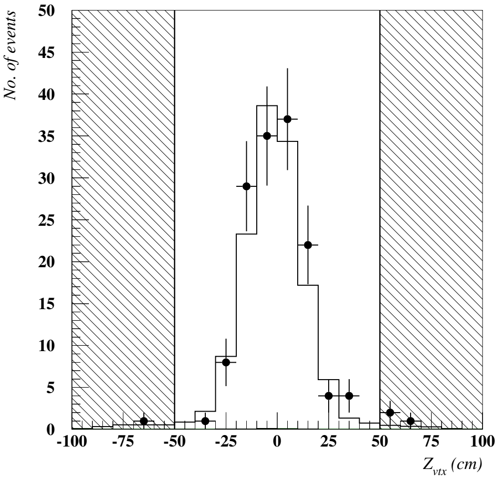

Figure 5.9: Distribution of the Z position of the interaction vertex measured from the timing of energy deposits in FCAL, for the low γ_0 charged current event sample, after all other cuts have been applied. The data events are shown as closed circles, the sum of signal and background MC as the open histogram, and the background contribution is shown by the shaded histogram. The shaded areas show those events that pass all other cuts but are rejected by the Z vertex position cut. In the unshaded regions there is good agreement between data and MC.

reject these events. Events are required to satisfy the following criteria in order to be identified as NC DIS, and are then rejected.

- $P_T < 30$ GeV

  Neutral current DIS events are expected to be a background at low P_T. This is shown in figure 5.10 (a), where the shaded histogram shows the contribution from NC DIS MC.

- $\delta > 20$ GeV

  The quantity δ peaks at twice the electron beam energy for NC DIS events, and close to zero for charged current DIS events. This is shown in figure 5.10 (b), where the shaded histogram shows the contribution from NC DIS MC.

- SINISTRA 95 electron

  An electron candidate is required using the SINISTRA 95 [36] program. This uses a neural network to identify the characteristic pattern of energy deposited in the calorimeter by a electron. The energy of the scattered electron candidate is required to be greater than 4 GeV. The probability function of the electron finder must give a high probability of a correctly identified electron. Figures 5.10 (c) and 5.11 (a) show the distributions of scattered electron energy, E'_e, and electron probability, E_{PROB}, for data and MC events.

- E_{NEAR} <5 GeV

  E_{NEAR} is the energy not associated with the electron candidate in a surrounding η,ϕ cone of 0.8. η is the pseudorapidity, defined as $\eta = -\ln\tan(\theta/2)$. E_{NEAR} is required to be low in order to exclude electromagnetic energy deposits that are inside hadronic jets. Figure 5.10 (d) shows the distribution of E_{NEAR} for data and MC events.

- $DCA < 15$ cm (in CTD acceptance)

  If the electron candidate is within the acceptance of the CTD ($15° < \theta <$

164°), then it is required to have a matching track that passes within 15 cm of the energy deposited in the calorimeter. It is required that there is no other track in an η,ϕ cone of 0.8 around the matched track. In addition it is required that the track must have at least 25% of the energy of the calorimeter deposit associated with the electron. Figures 5.11 (b) and (c) show the distributions of the distance of closest approach, DCA, of the matching track to the calorimeter deposit, and the fraction of the track momentum to the calorimeter energy, P_{TRK}/E_{CAL}.

- $P_T^e > 20$ GeV (forward of CTD acceptance)
  Electron candidates that are forward of the CTD acceptance are required to have at least 20 GeV of transverse momentum. Requiring high transverse momentum distinguishes genuine electrons from hadronic deposits. Figure 5.11 (d) shows the distribution of the transverse momentum of the scattered electron candidate, P_T^e, for events in which the electron is very forward in the detector.

5.6 Halo and cosmic muon rejection

Halo and cosmic muon events are rejected using the programs ISITAMU [37] and MUFFIN [38]. A characteristic of muon events is the observation of long narrow energy deposits in the calorimeter which correspond to a straight line trajectory through the detector. These programs use the topology of calorimeter energy deposits and tracks in the CTD to identify cosmic and beam halo muon events. In addition MUFFIN makes use of data from the muon chambers, backing calorimeter and timing information from the calorimeter to perform sophisticated pattern recognition, in order to identify muon events.

For events with low γ_0 additional background rejection is required. Halo muon events typically form a narrower shower than a hadronic jet from an *ep* interaction. The width of showers measured in the FCAL is used to identify halo muon events, and reject them.

5.7 Data quality

The electronics associated with calorimeter photo-multiplier tubes (PMTs) can suffer from random discharges, which fake energy deposits. These sparks in the calorimeter are characterised by a large imbalance in the energy reported by the two PMTs, for the calorimeter cell. These events are identified by this energy imbalance and rejected.

Runs unsuitable for physics analysis, for some reason, such as failure of a detector component, are rejected.

5.8 Calorimeter timing cuts

The calorimeter provides high precision timing for each cell. Each calorimeter cell has a local clock, which is offset according to the geometry of the calorimeter. The offsets are chosen such that a particle travelling at the speed of light from the nominal interaction point will strike any cell at the cell's time $t = 0$. The timing is also tied into the HERA bunch crossing time, so that calorimeter timing cuts can be used to reject non-ep interactions and noise.

Calorimeter timing cuts were used to reject events that were inconsistent with an interaction near the nominal interaction point. Calorimeter timing cuts were applied to the FCAL and RCAL separately, and also to the global calorimeter time, the interval between the FCAL and RCAL times, and the interval between the times for the upper and lower halves of the BCAL. The global calorimeter time is an average of the times from the different sections of the calorimeter. Events were rejected using the timing cuts only if both PMTs for each calorimeter cell were used in the energy calculation. The calorimeter timing cuts used are summarised in table 5.1.

Timing cut	Energy requirement
$\mid T_{FCAL} \mid< 6$ ns	$E_{FCAL} > 0.6$ GeV
$\mid T_{FCAL} \mid< 5$ ns	$E_{FCAL} > 10$ GeV
$\mid T_{RCAL} \mid< 6$ ns	$E_{RCAL} > 0.6$ GeV
$\mid T_{RCAL} \mid< 5$ ns	$E_{RCAL} > 10$ GeV
$\mid T_{GLOBAL} \mid< 6$ ns	$E_{GLOBAL} > 2$ GeV
$\mid T_{FCAL} - T_{RCAL} \mid< 6$ ns	E_{FCAL} and $E_{RCAL} > 1$ GeV
$\mid T_{UP} - T_{DOWN} \mid< 8$ ns	E_{UP} and $E_{DOWN} > 1$ GeV

Table 5.1: Summary of calorimeter timing cuts.

The timing for calorimeter energy deposits is not well simulated in MC. Therefore a sample of NC events was used to estimate the efficiency of the timing cuts for charged current events. The efficiency was found to be 99.6%, and was neglected in the cross section determination.

5.9 Kinematic region

Figure 5.12 shows the distributions of Q^2 and y, for data and MC events after all other cuts have been applied. The event sample is restricted to the region where Q^2 >200 GeV^2 and $y < 0.9$. This restricts the measurements to a region where the Jacquet-Blondel estimators give good resolution for the kinematic quantities (see section 4.4), and the background contribution is small. In addition 8 cosmic and halo muon events were rejected by a visual scan. After selection 642 candidate events remain in data from the 1,254,508 events passing the offline pre-selection. The expected number of events from MC simulation is 653. The selection efficiency for each cut from MC and the fraction of data events passing each cut are shown in table 5.2. The x and y of the selected data events are shown in figure 5.13. Overall it has been shown that the MC describes the data adequately and the background contribution is small, so the MC can be used to unfold the cross sections.

Cut	MC efficiency (%)	Fraction surviving in data (%)
Offline pre-selection	88.8	100.0
FLT	91.1	95.1
SLT	90.8	89.3
TLT	89.8	93.7
P_T	76.7	30.5
$P_T(-ir)$	72.6	15.1
P_T/E_T	83.6	43.3
Z_{vtx}	95.3	62.4
Q^2	84.0	26.4
y	96.2	97.9
$N_{good} \geq 1$	98.1	69.2
N_{good} compared to N_{trks}	79.8	35.6
$\Delta\Phi$	92.4	73.7
E_{BHAC}/E_{BCAL}	99.9	94.7
Halo & cosmic muon rejection	99.7	86.0
CAL timing	99.6	97.0
NC rejection	99.6	99.5
PhP rejection	90.7	73.8
CAL spark rejection	100.0	95.8
Low γ_0 halo muon rejection	99.1	92.2
Visual scan	-	100.0

Table 5.2: Summary of the charged current event selection. The fraction of the generated MC events that pass each selction cut is shown. Also shown is the fraction of data events passing the offline pre-selection that also pass each selection cut.

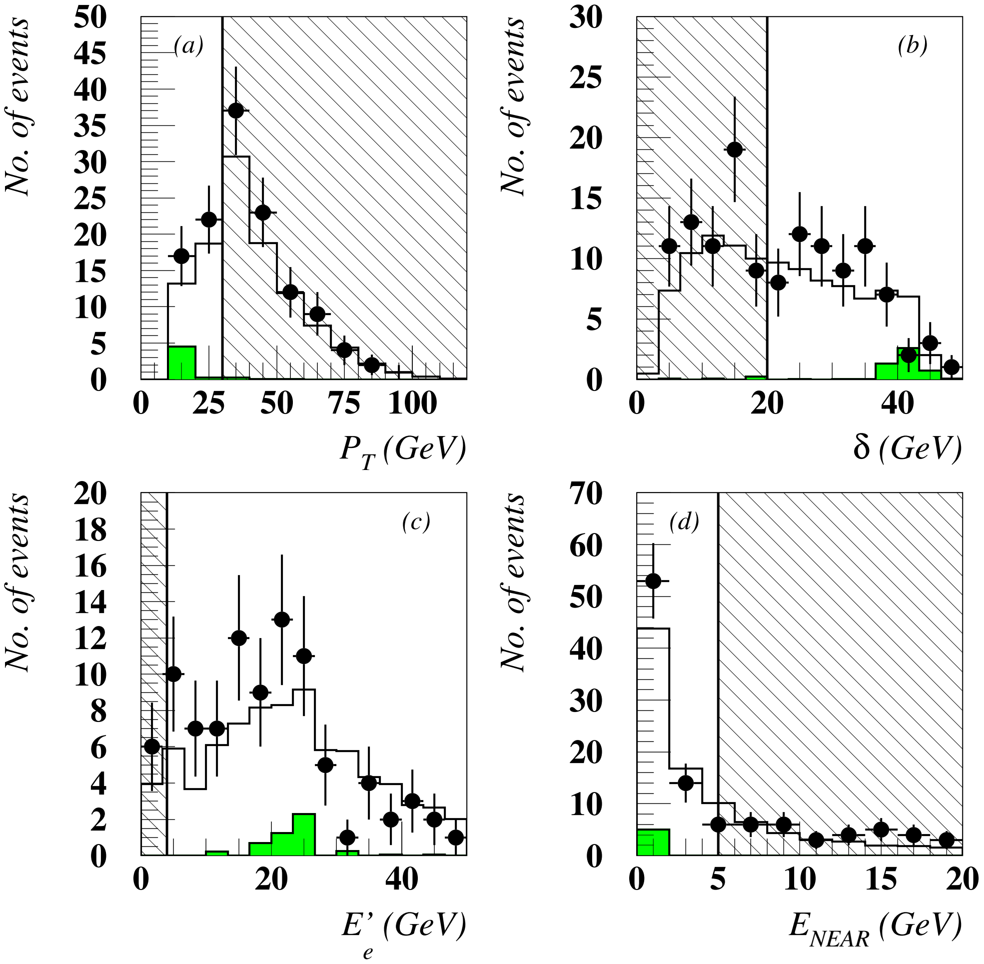

Figure 5.10: Distributions of quantities used to reject NC DIS events, for events where an electron is found. The data events are shown as closed circles, the sum of signal and background MC as the open histogram, and the NC DIS MC background contribution is shown by the shaded histogram. The shaded areas show the requirements detailed in the NC rejection algorithm.

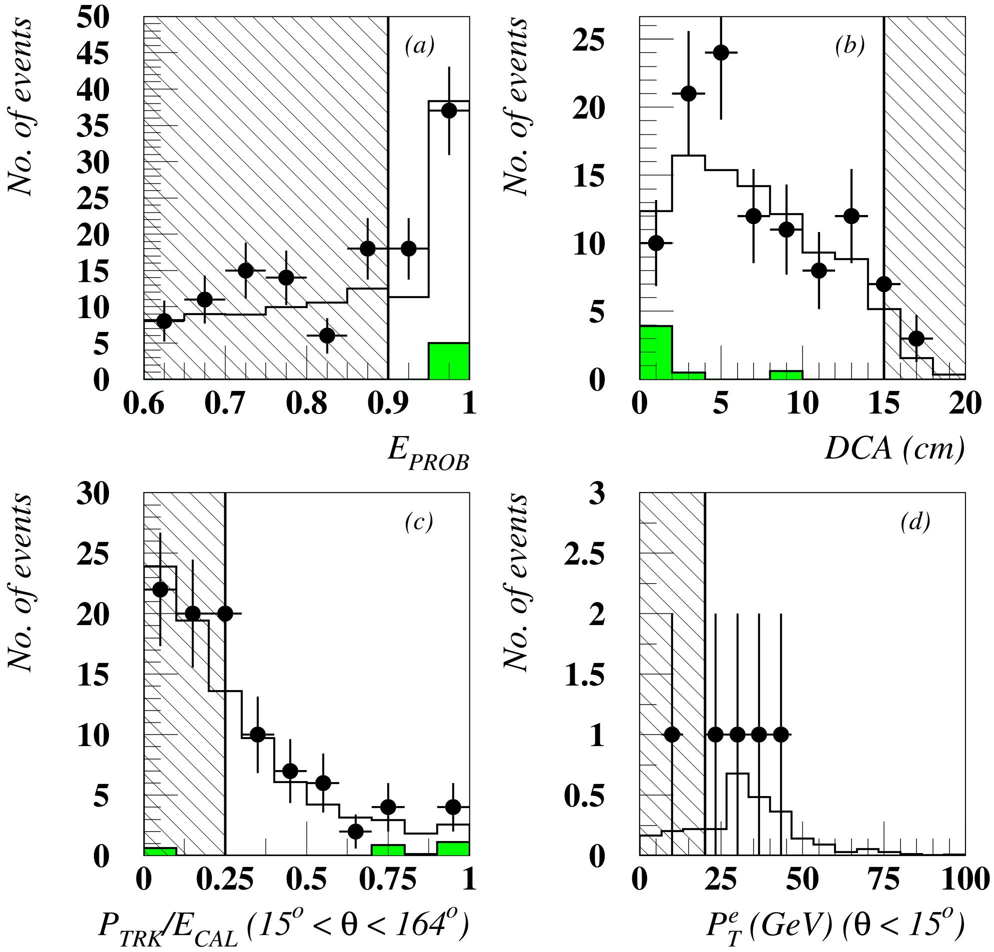

Figure 5.11: Distributions of quantities used to reject NC DIS events, for events where an electron is found. The data events are shown as closed circles, the sum of signal and background MC as the open histogram, and the NC DIS MC background contribution is shown by the shaded histogram. The shaded areas show the requirements detailed in the NC rejection algorithm.

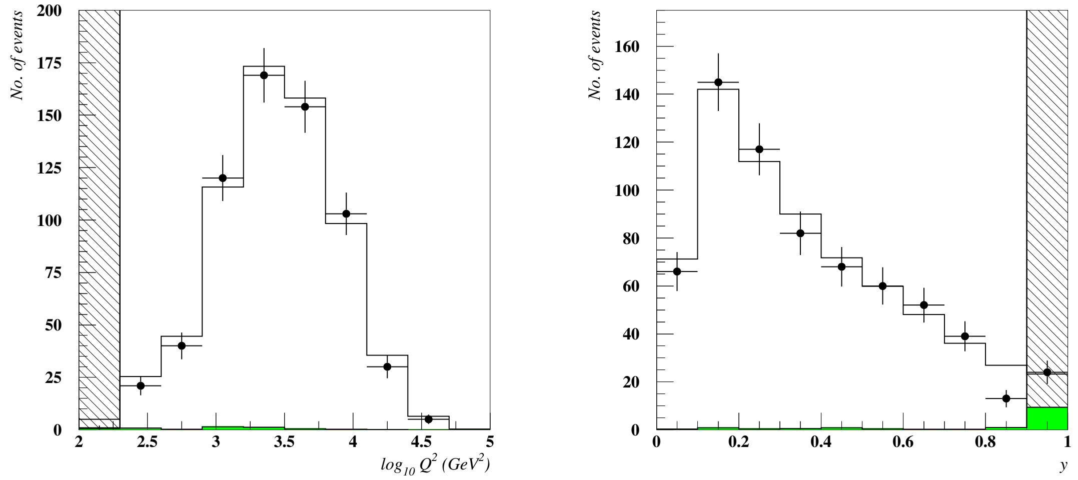

Figure 5.12: The distributions of Q^2 (left) and y (right) after all other cuts have been applied. The data events are shown as closed circles, the sum of signal and background MC as the open histogram, and the background contribution is shown by the shaded histogram. The shaded areas show those events that pass all other cuts but are rejected by the Q^2 or y requirement.

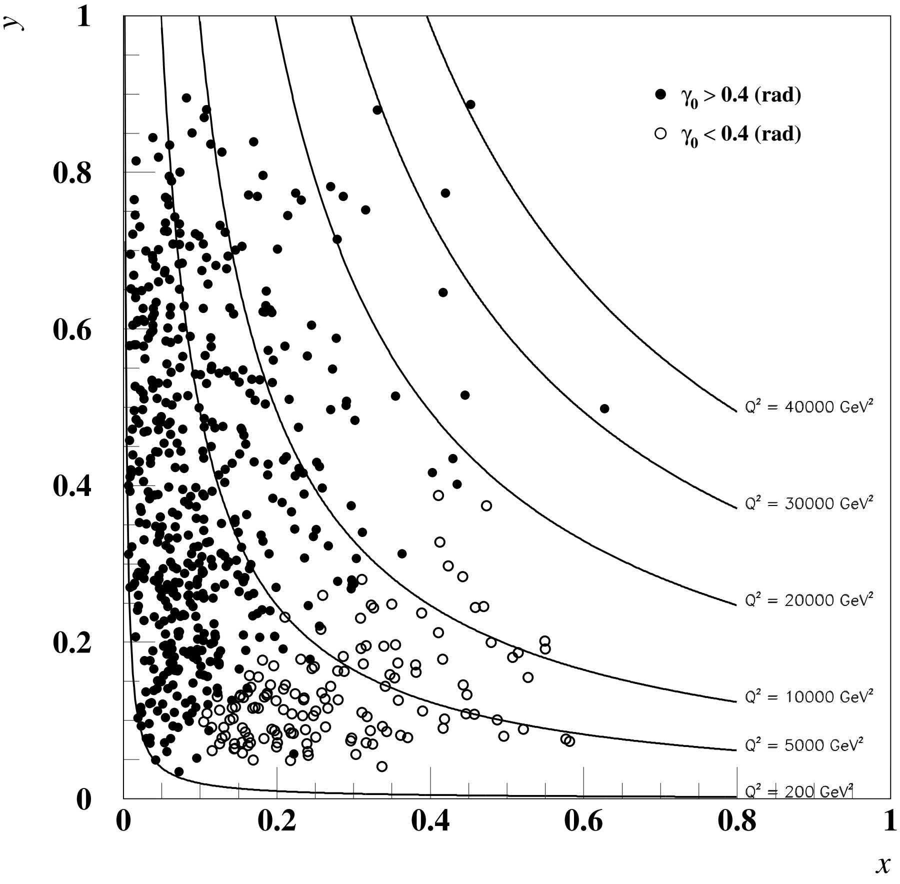

Figure 5.13: The charged current candidate events are shown plotted in the xy plane.

Chapter 6

Cross section measurements

In order to measure cross sections for charged current DIS the kinematic plane is divided into bins according to the statistical precision of the data and the resolution of the reconstruction. The number of data events measured in each bin is then used to determine the cross section. Measurements are made of the single differential cross sections with respect to Q^2, x and y: $d\sigma^{CC}_{Born}/dQ^2(e^-p)$; $d\sigma^{CC}_{Born}/dx(e^-p)$ and $d\sigma^{CC}_{Born}/dy(e^-p)$. In addition, the reduced double differential cross section, $\tilde{\sigma}(e^-p)$, is measured as a function of x and Q^2.

6.1 Bin definitions and resolutions

In order to measure the cross sections the events selected must be binned in the appropriate variables. The choice of the boundaries and sizes of the bins is important for an accurate measurement.

The acceptance, $\mathcal{A}$, efficiency, $\mathcal{E}$, and purity, $\mathcal{P}$, are defined for MC for each bin as follows:

$$\mathcal{A} = \frac{\text{no. of events measured in bin}}{\text{no. of events generated in bin}} \tag{6.1}$$

$$\mathcal{E} = \frac{\text{no. of events generated and measured in bin}}{\text{no. of events generated in bin}} \tag{6.2}$$

$$\mathcal{P} = \frac{\text{no. of events generated and measured in bin}}{\text{no. of events measured in bin}} \tag{6.3}$$

where the number of events measured in a bin, is the number of events that satisfy the selection criteria given in chapter 5, and are binned according to the measured value of x, y or Q^2. The number of events generated in a bin, is the number of events generated in the kinematic region of interest, binned according to the true value x, y or Q^2.

The acceptance, $\mathcal{A}$, reflects the geometric acceptance of the detector and the acceptance of the selection that is made to select charged current events and reject background. A high acceptance will give rise to a small correction to the measured cross section and minimise the systematic uncertainty from the MC simulation. The efficiency and purity in each bin characterise the effect of migrations and the resolution of the kinematic variable measurement. The efficiency measures the fraction of the events generated in a bin that are also measured in the same bin. A high efficiency means that migrations are small and the event selection does not reject a large fraction of the events. Similarly the purity gives a measure of how many of the events measured really belong in a different bin. A high purity means that the number of events that have migrated into the bin from neighbouring bins is small.

The acceptance, efficiency and purity, calculated from MC, in the bins used to extract the double differential cross section are shown in figure 6.1. It can be seen that the acceptance is typically $> 50\%$, the efficiency $> 40\%$ and the purity $> 50\%$, except in the low x and Q^2 bins where tight background rejection cuts are necessary.

For the measurement of $d\sigma^{CC}_{Born}/dQ^2(e^-p)$ 7 bins of equal width in $\log_{10}Q^2$ between Q^2 of 400 GeV^2 and Q^2 of 28000 GeV^2 were chosen. In addition bins from Q^2

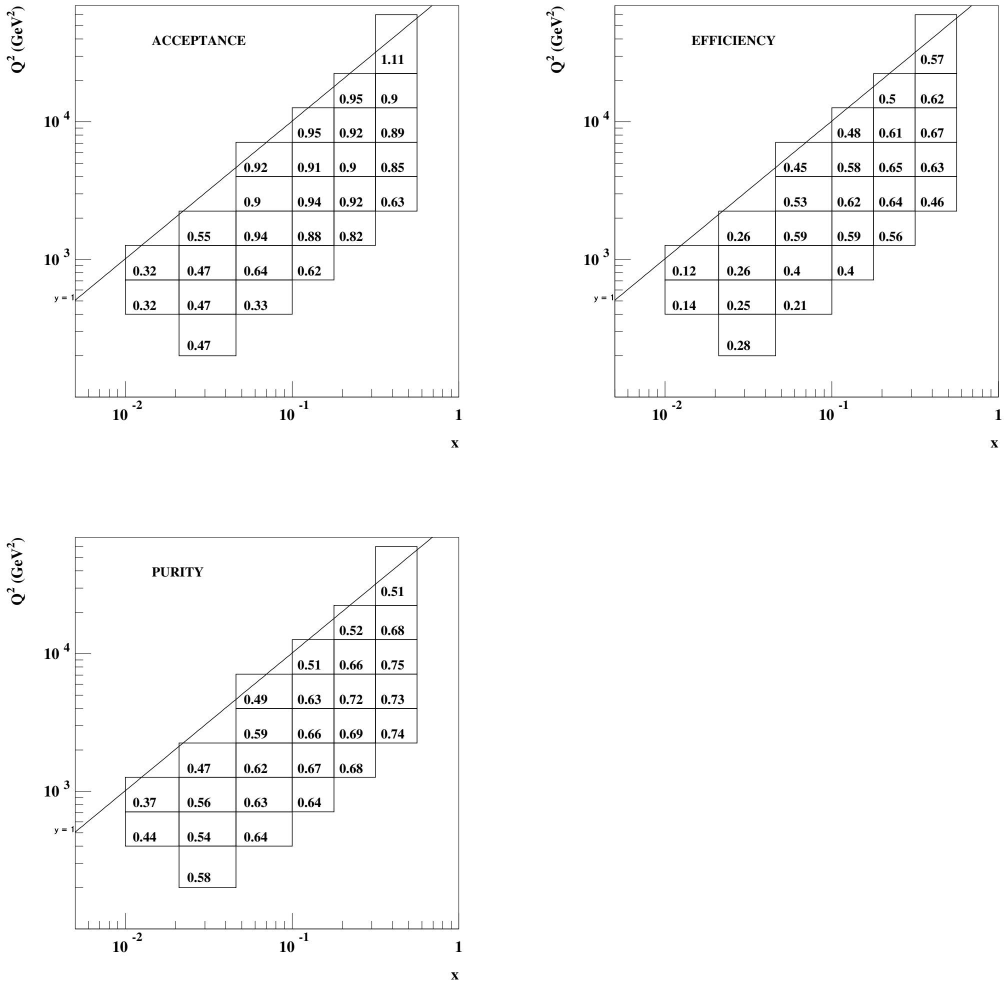

Figure 6.1: The acceptance, efficiency and purity are shown in the bins used for the extraction of the double differential cross section.

of 200 to 400 GeV^2 and Q^2 of 28000 to 60000 GeV^2 were used. The lower Q^2 bin width reflects the observation that the Q^2 resolution of the Jaquet-Blondel estimators becomes worse as Q^2 decreases. In addition the lowest Q^2 bin is affected most by background contamination. The highest Q^2 bin is made wider due to the limited statistics available in data. The value of $d\sigma^{CC}_{Born}/dQ^2(e^-p)$ is quoted at the logarithmic centre of each of the bins.

The x resolution of the Jaquet-Blondel estimators improves significantly with increasing x. Therefore 3 bins were chosen with equal width in $\log_{10}x$ from x of 0.01 to x of 0.1, and 4 bins with equal width in $\log_{10}x$ from x of 0.1 to x of 1. The differential cross section $d\sigma^{CC}_{Born}/dx(e^-p)$ is quoted at the logarithmic centre of each bin except in the highest x bin, in which the cross section falls extremely steeply so the lower value of x=0.65 was chosen.

The cross section $d\sigma^{CC}_{Born}/dy(e^-p)$ changes rapidly at low y, therefore 2 bins were defined with equal bin widths between y of 0 and y of 0.2. Five further bins, with equal bin widths, were defined from y of 0.2 to y of 0.9. The differential cross section is quoted at the centre of each bin.

The resolutions of the Jacquet-Blondel estimators, as measured from MC, are shown in the cross section bins for the single differential cross sections $d\sigma^{CC}_{Born}/dQ^2(e^-p)$, $d^{CC}_{Born}\sigma/dx(e^-p)$ and $d\sigma^{CC}_{Born}/dy(e^-p)$, in figures 6.2, 6.3 and 6.4. In each case the distributions are centred around zero, so no large bias is expected. The bins widths were chosen such that each bin is significantly wider than the resolution of the measured quantity in the kinematic region of the bin (see figures 4.4, 4.5 and 4.6). This ensures that migration between bins is rare and that the purity and efficiency for each bin is high.

The bins chosen for the extraction of the double differential cross section are a combination of the bins chosen for the measurements of $d\sigma^{CC}_{Born}/dQ^2(e^-p)$ and $d\sigma^{CC}_{Born}/dx(e^-p)$, and are shown in figure 6.5. Figure 6.6 illustrates the migrations expected, from the MC simulation, in the double differential bins. For each bin

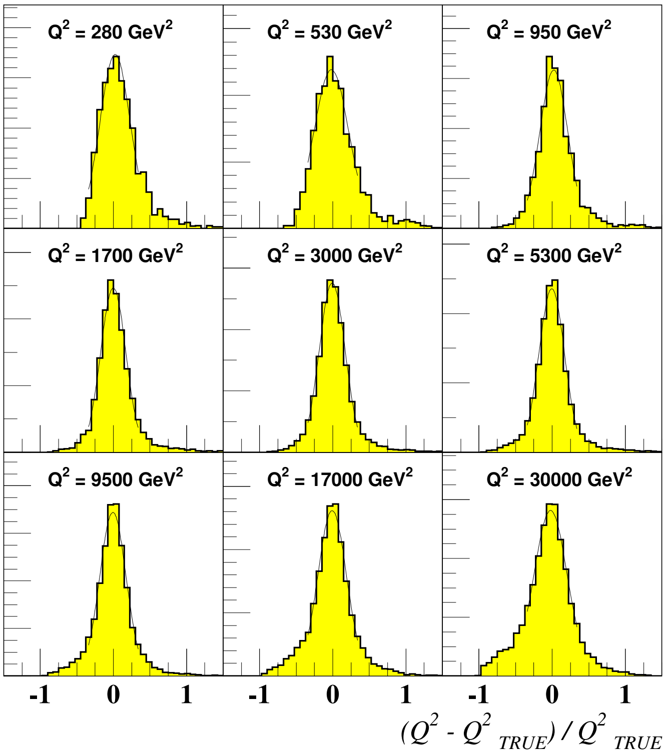

Figure 6.2: The resolution of the measured Q^2 is shown in the bins used for the extraction of the cross section $d\sigma^{CC}_{Born}/dQ^2(e^- p)$.

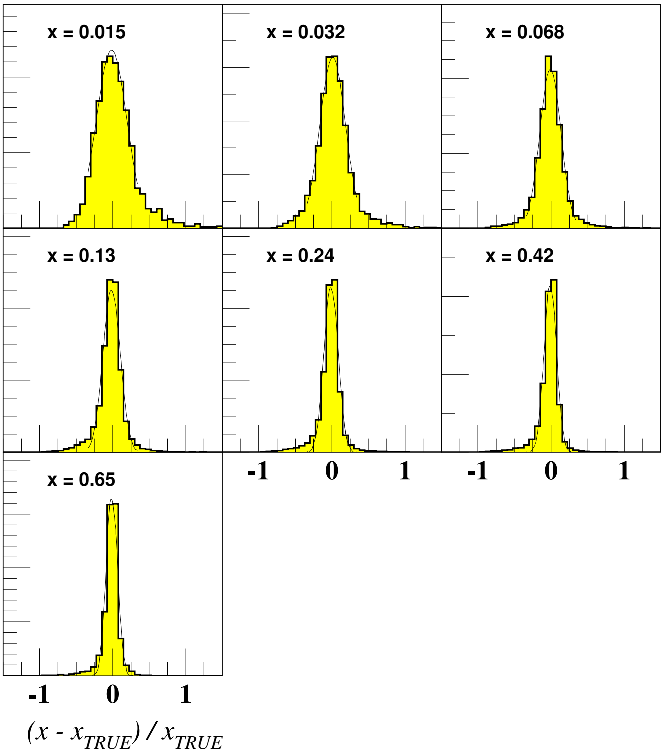

Figure 6.3: The resolution of the measured x is shown in the bins used for the extraction of the cross section $d\sigma^{CC}_{Born}/dx(e^{-}p)$.

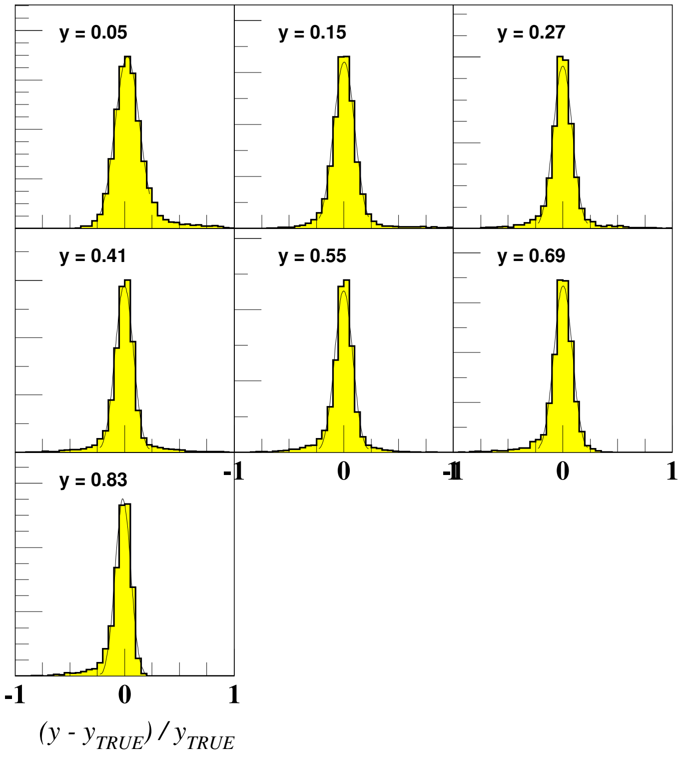

Figure 6.4: The resolution of the measured y is shown in the bins used for the extraction of the cross section $d\sigma^{CC}_{Born}/dy(e^{-}p)$.

an arrow is drawn from the mean generated x and Q^2 to the mean measured x and Q^2.

6.2 Extracting the cross sections

The cross sections are measured from the number of candidate events in each cross section bin. Detector acceptance will reduce the number of events in each bin, and detector resolution will move events from their true position and cause migrations, so that events end up in another bin. In addition initial state radiation will change the kinematics of the events. The detector and radiative effects must be removed to extract an accurate measurement of the Born cross sections. Bin-by-bin unfolding was chosen as the method of cross section extraction. Using this method factors to correct the number of events measured for acceptance, migrations and resolution were calculated for each cross section bin.

The measured cross section can be written in terms of the number of data events measured, N^{data}_{meas}, the integrated luminosity, $\mathcal{L}$, and the acceptance, $\mathcal{A}$ as:

$$\sigma^{data}_{meas} = \frac{N^{data}_{meas} - N^{bkgd}_{meas}}{\mathcal{L}\mathcal{A}} \tag{6.4}$$

where N^{bkgd}_{meas} is the number of background events estimated using MC, weighted to the data luminosity, that must be subtracted from the number of data events measured. The Born cross section is given by:

$$\sigma_{Born} = \mathcal{C}_{rad} \cdot \sigma_{meas} \tag{6.5}$$

where $\mathcal{C}_{rad}$ is the radiative correction factor, which is given by:

$$\mathcal{C}_{rad} = \frac{\sigma^{theory}_{Born}}{\sigma^{MC}_{meas}} \tag{6.6}$$

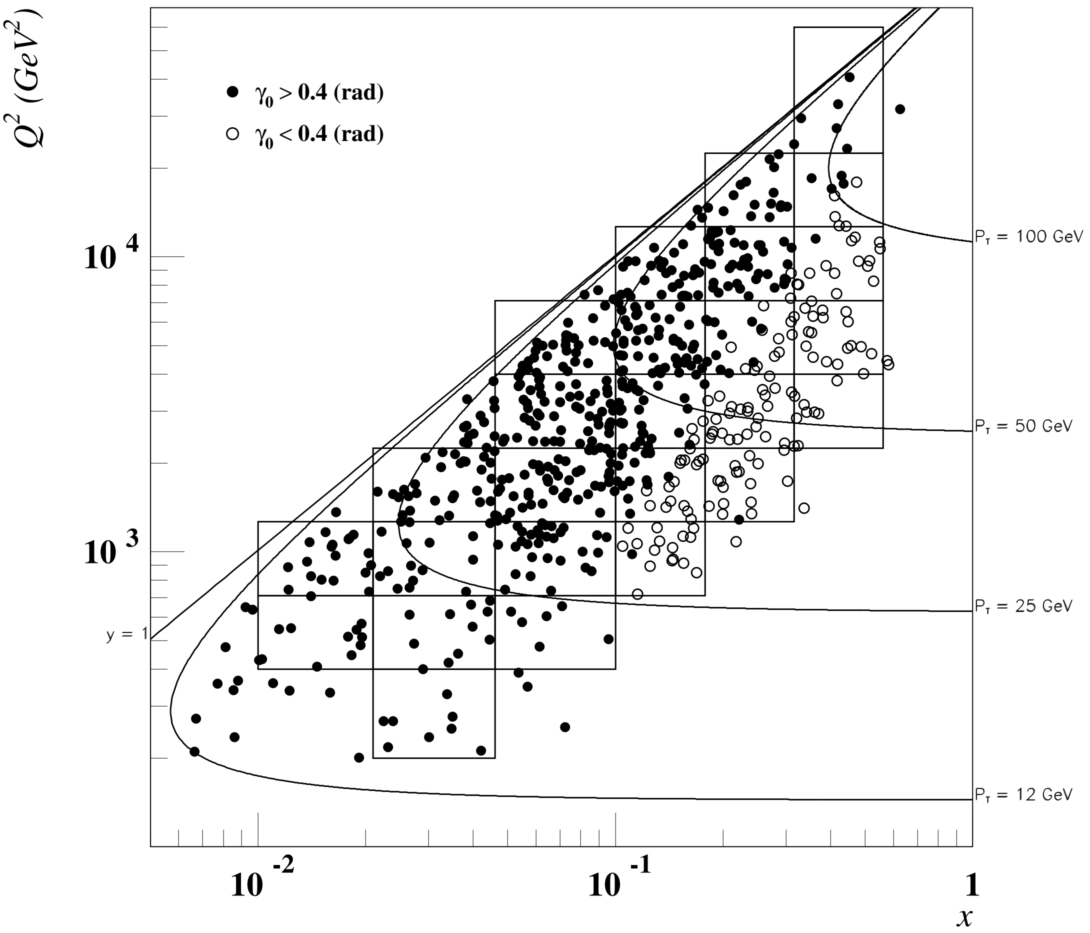

Figure 6.5: The charged current candidate events are shown plotted in the xQ^2 plane, with the bins used for the extraction of the double differential cross section marked.

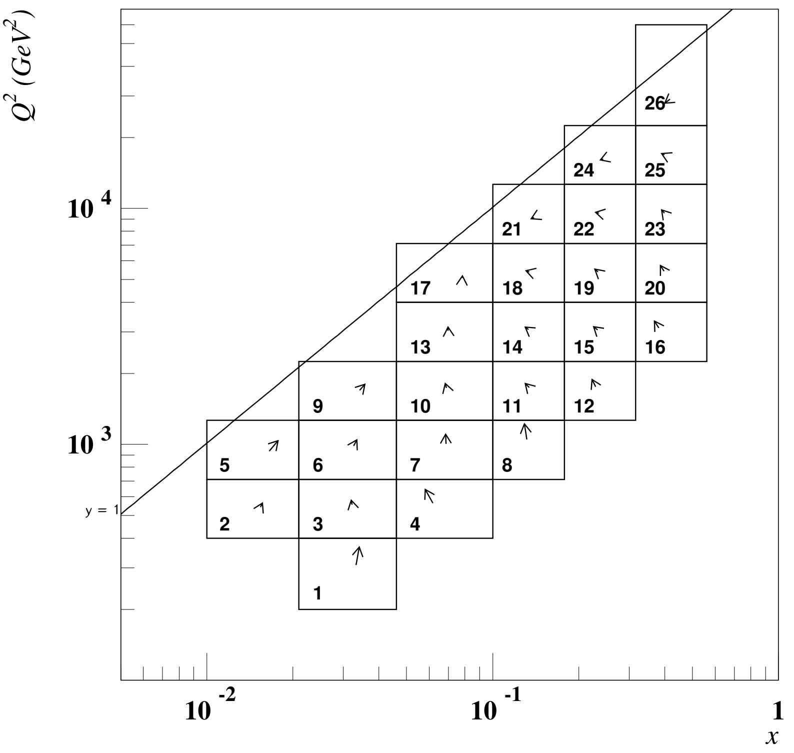

Figure 6.6: The average migration expected in each of the bins used to extract the double differential cross section is shown. The arrows go from the mean generated x and Q^2 to the mean measured x and Q^2 in each bin.

where σ^{theory}_{Born} is the Born cross section and σ^{MC}_{meas} is the radiative cross section from the MC. Combining these expressions, the Born cross section in data is given by:

$$\sigma^{data}_{Born} = \frac{N^{data}_{meas} - N^{bkgd}_{meas}}{N^{MC}_{meas}} \cdot \sigma^{theory}_{Born} \tag{6.7}$$

where N^{MC}_{meas} is the number of MC events measured, weighted to the data luminosity. To extract the differential cross sections, for example with respect to Q^2, a bin centre correction, $\mathcal{C}_{bin}$, is defined to convert the cross section integrated over a bin into a differential cross section quoted at a particular point.

$$\mathcal{C}_{bin} = \frac{d\sigma^{theory}_{Born}/dQ^2 \mid_{Q^2_0}}{\sigma^{theory}_{Born}} \tag{6.8}$$

The differential cross section with respect to Q^2 is then given by:

$$\left.\frac{d\sigma^{data}_{Born}}{dQ^2}\right|_{Q^2_0} = \frac{N^{data}_{meas} - N^{bkgd}_{meas}}{N^{MC}_{meas}} \cdot \left.\frac{d\sigma^{theory}_{Born}}{dQ^2}\right|_{Q^2_0} \tag{6.9}$$

where Q^2_0 is the point in the bin at which the cross section is quoted.

The statistical uncertainty calculation for the unfolded cross sections takes into account the statistical error from the number of data events and also the small contribution from MC statistics. The statistical error assigned to the number of events in the data is $\sqrt{N^{data}_{meas}}$ for bins with 12 or more events. For bins with less than 12 events a 67% confidence interval is calculated using Poisson statistics, and the boundaries of this confidence interval are taken as the statistical uncertainty. For the MC samples, the number of events is the sum of the event weights, $\sum_i \omega_i$, and thus the statistical error is given by the square root of sum of the squares of the weights, $\sqrt{\sum_i \omega_i^2}$. The statistical error on the cross section, for example with respect to Q^2, is given by:

$$\Delta\left(\frac{d\sigma^{data}_{Born}}{dQ^2}\right) = \sqrt{\left(\frac{\Delta N^{data}_{meas}}{N^{MC}_{meas}}\right)^2 + \left(\frac{\Delta N^{bkgd}_{meas}}{N^{MC}_{meas}}\right)^2 + \left(\frac{\Delta N^{MC}_{meas}(N^{data}_{meas} - N^{bkgd}_{meas})}{(N^{MC}_{meas})^2}\right)^2} \cdot \frac{d\sigma^{theory}_{Born}}{dQ^2} \tag{6.10}$$

where ΔN^{data}_{meas}, ΔN^{bkgd}_{meas} and ΔN^{MC}_{meas} are the statistical uncertainties from the number of data events, background MC events and signal MC events respectively.

6.3 Systematic uncertainty

The event and detector simulations result in distributions of simulated events that do not perfectly describe the data event distributions. Using these simulated events to unfold the cross sections will introduce some bias into the measured cross sections. The systematic uncertainty that is assigned to the cross section measurements is estimated separately for each kinematic variable bin by varying MC parameters by an amount that reflects the understanding of the detctor and event simulations. For each systematic uncertainty the cross sections are unfolded and compared to the nominal values, and the difference is considered to be the systematic error. The systematic errors that increase and decrease the cross sections are added separately in quadrature for each kinematic bin.

6.3.1 Calorimeter energy scale

The uncertainty in the absolute energy scale of the calorimeter introduces an important systematic change in the measured cross sections. Detailed studies have been made [39] using a variety of methods to quantify the difference between the MC energy scale and that measured in the real detector. Using NC events, the double angle method of reconstruction can be used to calculate the amount of transverse momentum expected in the calorimeter (see section 4.4). This is independent of the absolute energy scale of the calorimeter. By comparing the ratio of double angle transverse momentum to measured transverse momentum, between data and MC, the difference between the real detector response and the simulation can be evaluated. This comparison is shown as a function of the hadronic angle γ in figure 4.7, and shows a result consistent with the study in [39]. The systematic error is estimated by varying the energy scale in the MC simulation. The energy scale in the MC was varied by $\pm 2\%$ in the FCAL and

BCAL, and by ±3% in the RCAL. The change in the cross sections, δ_{ESCALE}, resulting from this is shown in figure 6.7. It is found that at high x and high Q^2, the energy scale uncertainty dominates the systematic error, yielding changes in the cross section measurements of between 20% and 30%.

6.3.2 Sensitivity to selection thresholds

The distributions of important event quantities are not identical for simulated events and the data events. When selection cuts are applied to these distributions, disagreement between data and MC distributions can result in biases in the measured cross sections. In order to estimate the uncertainty that is to be assigned to the cross section measurement, the selection thresholds are varied in the event selection by approximately the resolutions of the quantities involved.

A summary of the selection thresholds that were varied is given in table 6.1. In the majority of kinematic bins it was found that varying the selection thresholds resulted in small changes in the measured cross sections. However, it was found that varying the P_T/E_T threshold gave a change in the cross section of around 10% at low Q^2 in $d\sigma^{CC}_{Born}/dQ^2(e^-p)$ and up to 15% in the double differential cross section bins. Varying the $P_T(-ir)$ cut threshold was found to give changes in the cross section of $\sim$ 10% in the single differential cross sections at low Q^2 and low y. In the double differential cross section bins the corresponding change was $\sim$ 15%, in the low Q^2 and high x bins. The tracking requirment for $P_T < 30$ GeV was found to give the largest changes in the cross sections. A change in the cross section of $>$ 20% was observed in the lowest Q^2 bin of $d\sigma^{CC}_{Born}/dQ^2(e^-p)$, and changes $>$ 30% were observed in the lowest Q^2 bins of the double differential cross section.

6.3.3 Effect of F_L

The hard scattering process, as simulated in the MC events by the program LEPTO, neglects the contribution to the cross section from the longitudinal

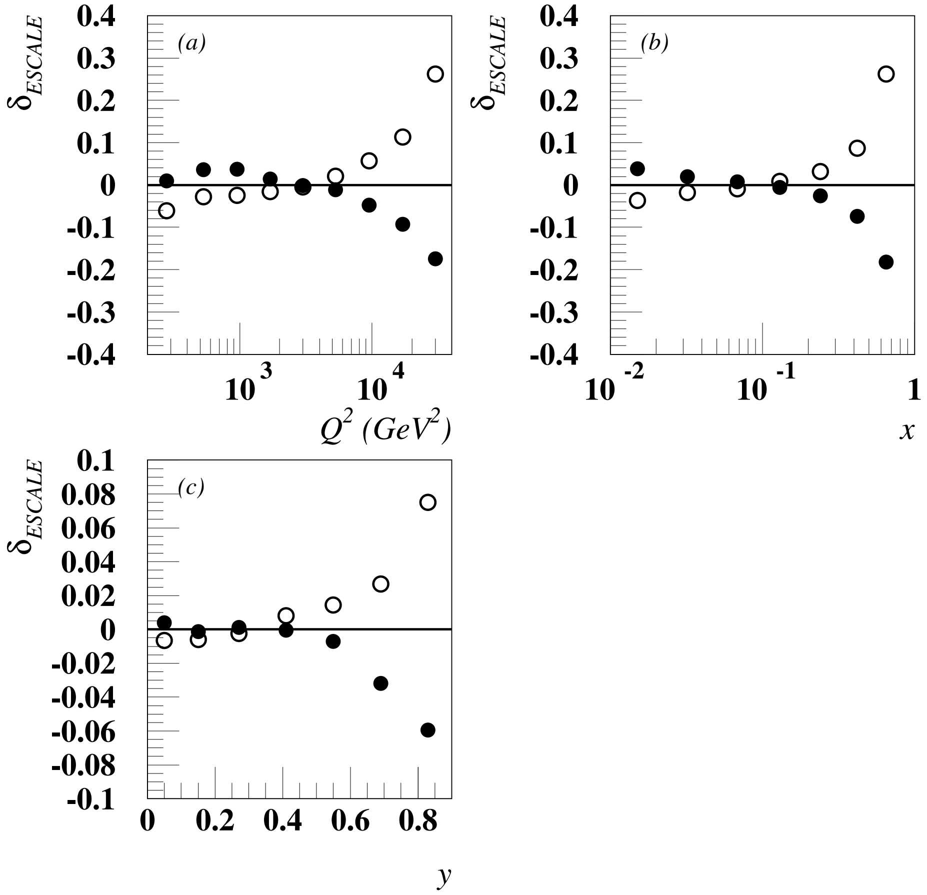

Figure 6.7: Relative uncertainty in the measurement of the cross sections due to the uncertainty in the calorimeter energy scale, δ_{ESCALE}, for (a) $d\sigma^{CC}_{Born}/dQ^2(e^-p)$, (b) $d\sigma^{CC}_{Born}/dx(e^-p)$ and (c) $d\sigma^{CC}_{Born}/dy(e^-p)$. The closed circles show the change in nominal cross section when the energy scale is increased and the open circles show the change when it is decreased.

Quantity	Threshold
P_T high γ_0	12 ± 1.2 GeV
P_T low γ_0	25 ± 2.5 GeV
$P_T(-ir)$ high γ_0	10 ± 1.0 GeV
$P_T(-ir)$ low γ_0	25 ± 2.5 GeV
P_T/E_T	0.5 ± 0.05
$\Delta\Phi$ $P_T < 30$ GeV	0.5 ± 0.05 rad
$\Delta\Phi$ $P_T > 30$ GeV	2.0 ± 0.2 rad
Tracking $P_T > 30$ GeV	$N_{good} > 0.25 \pm 0.05(N_{trks} - 20 \pm 5)$
Tracking $P_T < 30$ GeV	$N_{good} > (N_{trks} - 5 \pm 1)$ or $N_{good} > 10 \pm 1$

Table 6.1: Summary of the selection thresholds varied.

structure function, F_L. The method for the extraction of the cross sections, described in section 6.2, ensures that consistent measurements of the cross sections including F_L are obtained. However the exclusion of F_L could have an effect on the acceptance and result in a bias in the measured cross sections. To investigate this effect the MC events were reweighted to the SM Born cross section including F_L, and the cross sections extracted and compared with the nominal measurements. The ratios of the extracted cross sections are shown in figure 6.8. The uncertainty introduced into the measurement of the cross sections is found to be largest at high y where it is $\sim 2\%$, and less than 1% in all the double differential x and Q^2 bins.

6.3.4 Monte Carlo fragmentation

The Monte Carlo events used to unfold the nominal cross sections use the ARIADNE colour dipole model of fragmentation. To test the sensitivity of the cross section measurements to higher order QCD effects in the hadronic final state, the cross section measurements were repeated using MC events with the matrix element parton shower (MEPS) model of fragmentation. A comparison of data and MC distributions is shown in figure 6.9, and a comparison of the cross sections extracted is shown in figure 6.10. The uncertainty introduced into the cross section measurements, δ_{MEPS}, is found to be largest at high Q^2 and high y where it is $\sim 15\%$ and at low x where it is $\sim 5\%$.

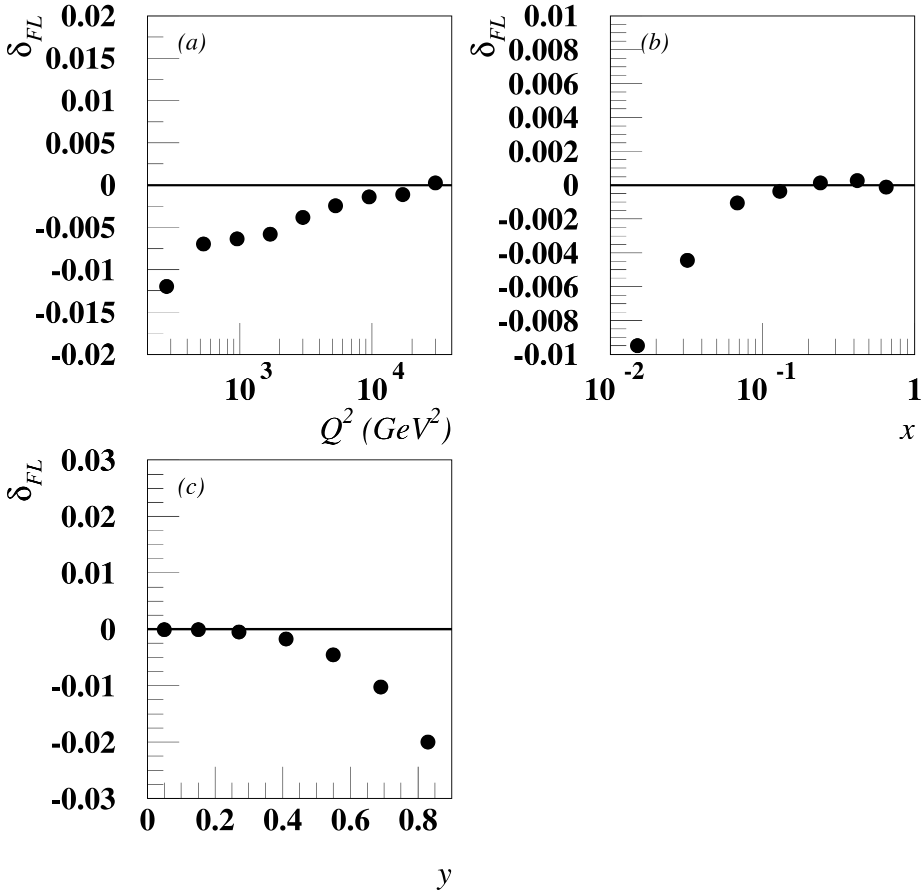

Figure 6.8: Relative uncertainty in the measurement of the cross sections due to the effect of F_L, δ_{F_L}, for (a) $d\sigma^{CC}_{Born}/dQ^2(e^-p)$, (b) $d\sigma^{CC}_{Born}/dx(e^-p)$ and (c) $d\sigma^{CC}_{Born}/dy(e^-p)$.

6.3.5 Parton density function

The MC events were generated using the CTEQ5D parameterisation of the parton density function of the proton. Therefore the x and Q^2 distributions of the generated events follow this prediction. To examine the effect of the choice of parton density function parameterisation on the measured cross sections, the MC events were reweighted to the prediction of the MRST (99) parameterisation, and the cross sections extracted and compared with the nominal measurements. The difference between the reweighted cross sections and the nominal cross sections was found to be typically less than 1% in all kinematic bins except the highest y bin where it is $\sim 1.5\%$.

6.3.6 Electroweak radiative correction

The radiative correction factors detailed in section 6.2, are calculated using the HERACLES program. The radiative cross sections from HERACLES have been compared with other calculations [40], and found to be in good agreement with differences typically small, but rising to $\sim 2\%$ at high x and low y.

The systematic uncertainty from the calculation of the radiative correction factors was neglected in the final cross section measurement.

6.3.7 Background subtraction

In order to check the normalisation of the photoproduction background MC events, a fit to the data P_T/E_T spectrum for events with $P_T < 30$ GeV (figure 5.2) was performed. Contributions from signal and background MC were included. Figure 6.11 shows the result of the fit for the normalisation, which yielded the normalisation factor N=$0.96^{+0.76}_{-0.40}$. In addition the fit was repeated varying the fractions of the direct and resolved photoproduction processes. The fit was found to have little sensitivity to this fraction. The normalisation of the photoproduction background MC was varied within the limits of the fit and the resulting change in the cross section was found to be negligable.

6.3.8 Vertex finding efficiency

The CTD vertex finding efficiency was estimated from low gamma charged current candidate events, which are not required to have a CTD vertex. The CTD vertex finding efficiency is defined as the ratio of the number of events with a CTD vertex to the total number of events. Figure 6.12 shows the CTD vertex finding efficiency as a function of γ_0, calculated for data and MC. It can be seen that although there is a difference in efficiency between data and MC at the low γ_0 end, good agreement is observed as γ_0 increases towards the 0.4 radian threshold where the analysis requires a CTD vertex. It can also be seen that the CTD vertex finding efficiency is approaching 100% at the threshold value of 0.4 radians. Given the high efficiency and the good agreement between the data and MC estimations, the contribution to the systematic error from the uncertainty in the CTD vertex finding efficiency is neglected.

6.3.9 Trigger efficiency

The first level trigger (FLT) is described in section 2.2.7, and the charged current trigger configuration used is described in section 5.1. The limited resolution of the calorimeter first level trigger (CFLT), results in a slow turn on to full efficiency of the trigger thresholds. This turn on can be esimated for the charged current trigger using events that fire an independent trigger. The trigger used included only the EMC and total energy measured in the calorimeter. The efficiency is defined as the fraction of the charged current events passing the independent trigger that also passed the charged current trigger. The efficiency as a function of offline P_T is shown in figure 6.13, for data and MC, for the $P_T(FLT) \geq 5$ GeV threshold. It can be seen that MC simulation has a higher efficiency for this trigger than that measured from the data for P_T less than the offline threshold of 12 GeV. The MC was reweighted so that the trigger efficiency reflected the efficiency measured in the data, and the cross sections extracted. The reweighting was found to give a negligible change in the measured cross sections and consequently this contribution to the overall systematic uncertainty was neglected.

6.3.10 Energy leakage

In a small fraction of events the energy deposited by the hadronic jet is not confined to the calorimeter. In this case the backing calorimeter (BAC), which consists of the instrumented iron yoke of the magnet surrounding the main components of the detector, can be used to correct the calorimeter energy. It is found that the mean fraction of the total calorimeter energy measured in the BAC is less than 0.1%, and therefore the contribution to the total systematic uncertainty from energy leakage into the BAC is neglected.

6.3.11 Kinematic correction

The method for correcting the biases in the Jacquet-Blondel estimators of x, y and Q^2 is described in section 4.4 and in detail in [31]. As a systematic check the fit to NC DIS MC for γ_{max} was repeated with the fraction of non-backsplash islands allowed to be removed decreased from 1% to 0.75%. The value of 1% is the result of a fit to maximise the efficiency of the correction, and a change to 0.75% represents the uncertainty associated with the fit. This still results in optimal reconstruction of x, y and Q^2. The cross sections were then extracted and compared with the nominal measurements. The difference was found to be less than 1%, except at the highest x and Q^2 where it was $\sim 2\%$ and the lowest y bin where the difference was found to be $\sim 3\%$

6.3.12 Monte Carlo distribution of the vertex position

The Monte Carlo events were generated with the vertex position distribution measured from NC DIS data events, using a method detailed in [33]. The method makes use of three overlapping regions in the Z coordinate to maximise selection efficiency for the NC DIS events used. Each of these regions is normalised according to the selection efficiency determined using MC events with a uniform distribution of the Z coordinate of the interaction vertex between -100 cm and +100 cm. The selection efficiency, and therefore normalisation, was varied by it's uncertainty in the outer two of the three regions defined, and the MC events reweighted accordingly. The central region is constrained by the overall normalisation. The change in the cross sections due to reweighting was found to be less than 0.5% and the contribution to the overall systematic uncertainty was neglected.

6.3.13 Summary of the systematic uncertainties

Figure 6.14 shows the total relative systematic uncertainty, δ_{SYST}, calculated by adding in quadrature the systematic uncertainties from each of the sources described previously in the kinematic bins used to unfold the cross sections. The uncertainty in the measured luminosity is 1.8% and is not included in the overall systematic uncertainty.

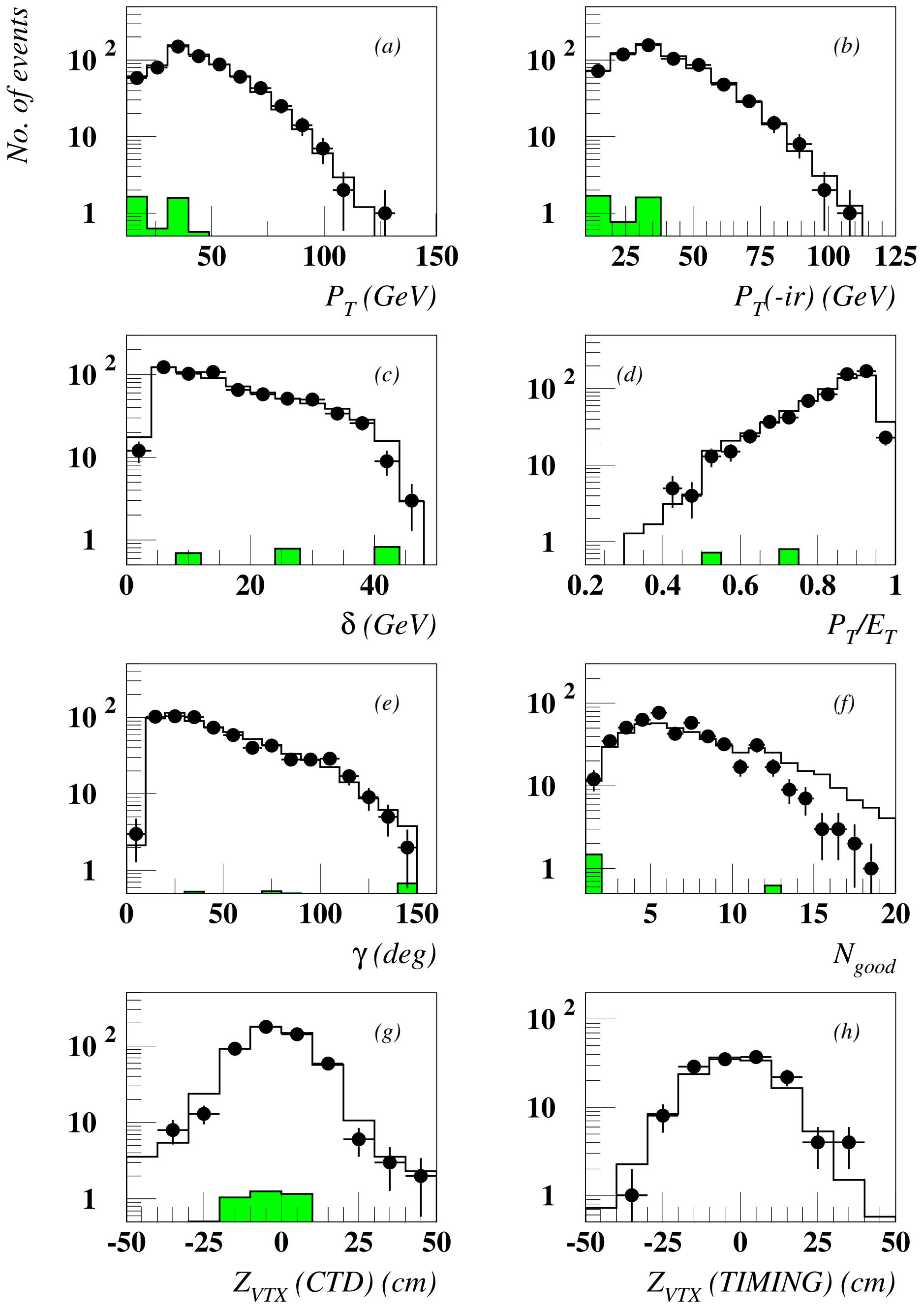

Figure 6.9: Comparison of data and MC distributions for MC with MEPS fragmentation. The data events are shown as closed circles, the sum of signal MEPS and background MC as the open histogram, and the background contribution is shown by the shaded histogram.

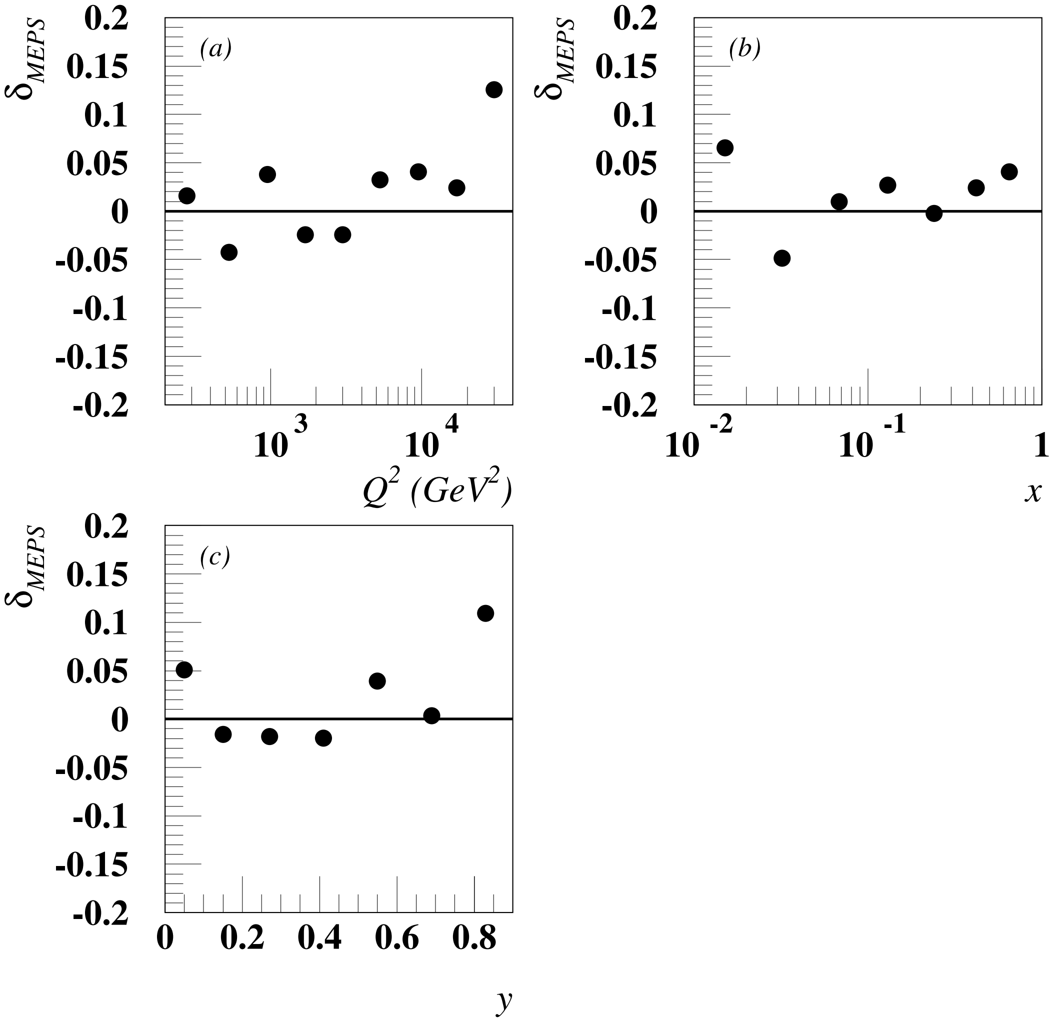

Figure 6.10: Relative uncertainty in the measurement of the cross sections due to Monte Carlo fragmentation, δ_{MEPS}, for (a) $d\sigma^{CC}_{Born}/dQ^2(e^-p)$, (b) $d\sigma^{CC}_{Born}/dx(e^-p)$ and (c) $d\sigma^{CC}_{Born}/dy(e^-p)$.

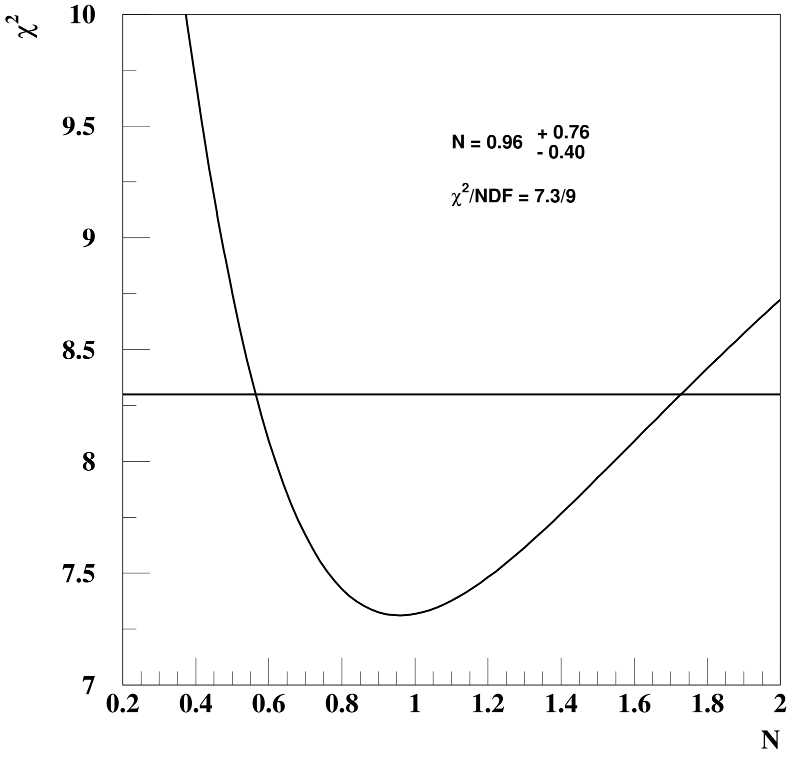

Figure 6.11: Result of the fit to the P_T/E_T spectrum for the overall normalisation of the photoproduction background Monte Carlo events.

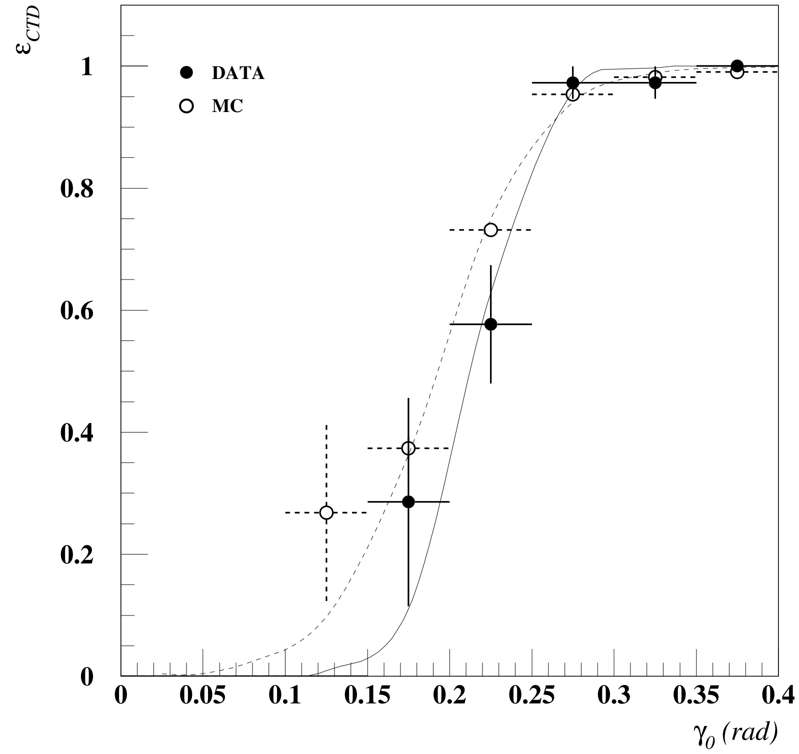

Figure 6.12: The CTD vertex finding efficiency, ε_{CTD}, for MC (open cirles) and data events (closed circles) as a function of the angle of the hadronic jet calculated assuming the nominal position for the interaction vertex, γ_0.

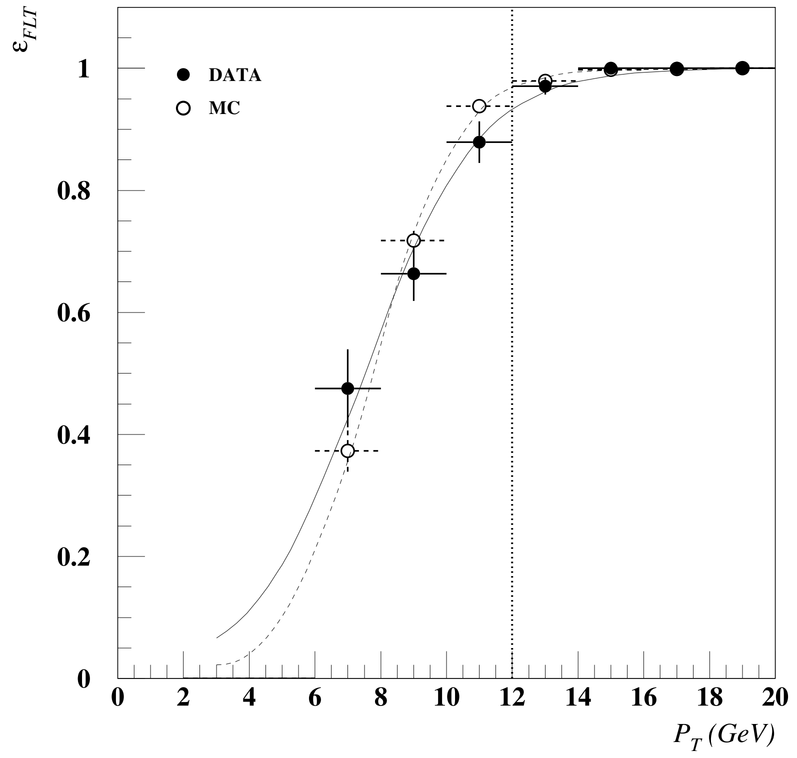

Figure 6.13: The FLT trigger efficiency, ε_{FLT}, for $P_T(FLT) \geq 5$ GeV is shown as a function of offline P_T for MC (open circles) and data events (closed circles). The dotted line shows the offline selection threshold of 12 GeV.

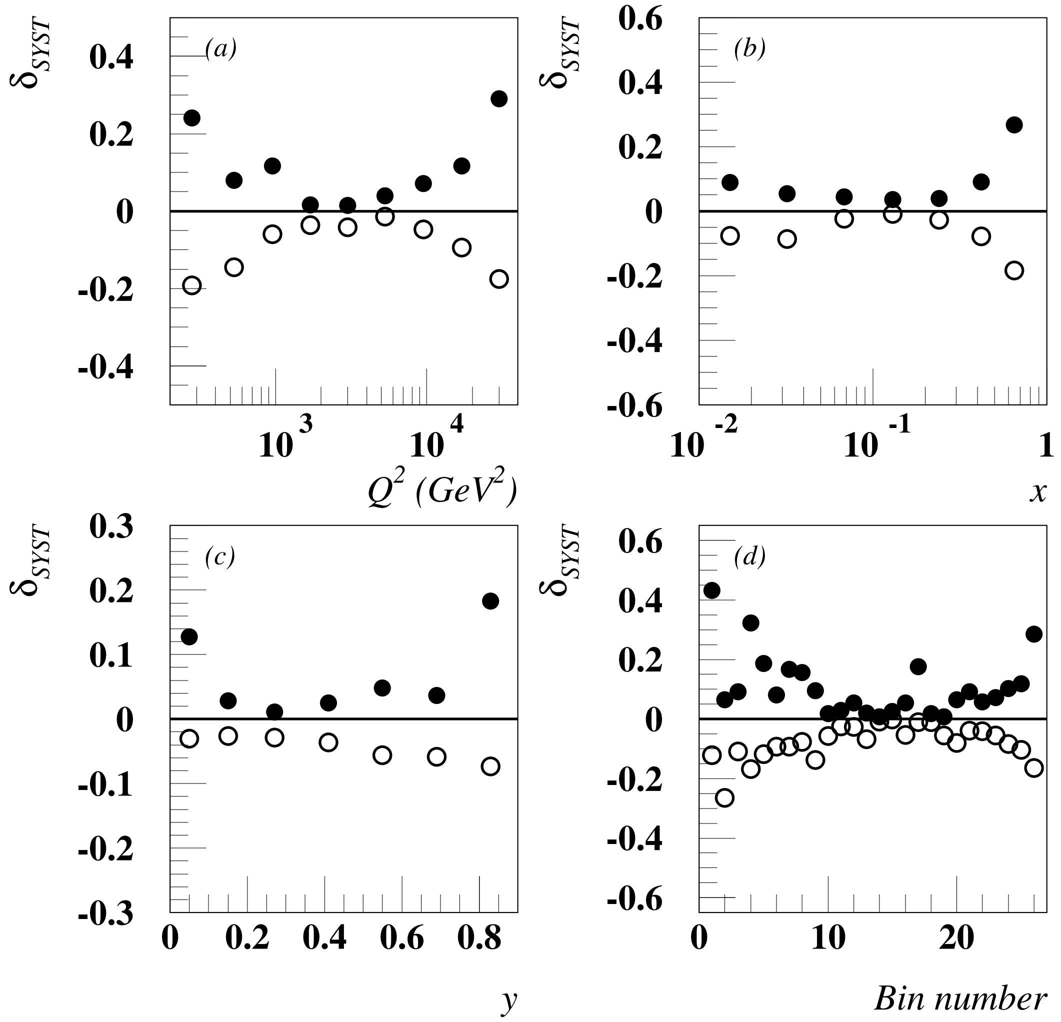

Figure 6.14: Relative total systematic uncertainty in the measurement of the cross sections, δ_{SYST}, for (a) $d\sigma^{CC}_{Born}/dQ^2(e^-p)$, (b) $d\sigma^{CC}_{Born}/dx(e^-p)$, (c) $d\sigma^{CC}_{Born}/dy(e^-p)$ and (d) $d^2\sigma^{CC}_{Born}/dxdQ^2(e^-p)$.

Chapter 7

Results and interpretation

7.1 Measured cross sections

The measured single differential cross sections with respect to Q^2, x and y are shown in figures 7.1, 7.2 and 7.3. In each case the measurements are compared to the SM expectation evaluated with the CTEQ5D and MRST (99) parameterisations of the parton density functions. The lower plot in each case shows the ratio of the measured cross section to the CTEQ5D prediction. The inner error bars, delimited by horizontal lines, show the statistical error, while the total error bar shows the quadratic sum of the statistical and systematic error. The shaded band shows the uncertainty in the SM prediction coming from the PDF parameterisation. This is evaluated from a ZEUS NLO QCD fit [41] to low Q^2 data from HERA and fixed target experiments. The SM gives a good description of the data.

The reduced double differential cross section is defined as:

$$\tilde{\sigma}(e^{\pm}p) = \left[\frac{G_F^2}{2\pi x}\left(\frac{M_W^4}{(Q^2+M_W^2)^2}\right)\right]^{-1} \cdot \frac{d^2\sigma_{Born}^{CC}(e^{\pm}p)}{dxdQ^2} \tag{7.1}$$

$$\tilde{\sigma}(e^{\pm}p) = \frac{1}{2}[Y_+F_2^{CC}(x,Q^2) - y^2F_L^{CC}(x,Q^2) \mp Y_-xF_3^{CC}(x,Q^2)] \tag{7.2}$$

To leading order in α_S, neglecting the contribution from bottom and top quarks, for e^-p scattering, this becomes:

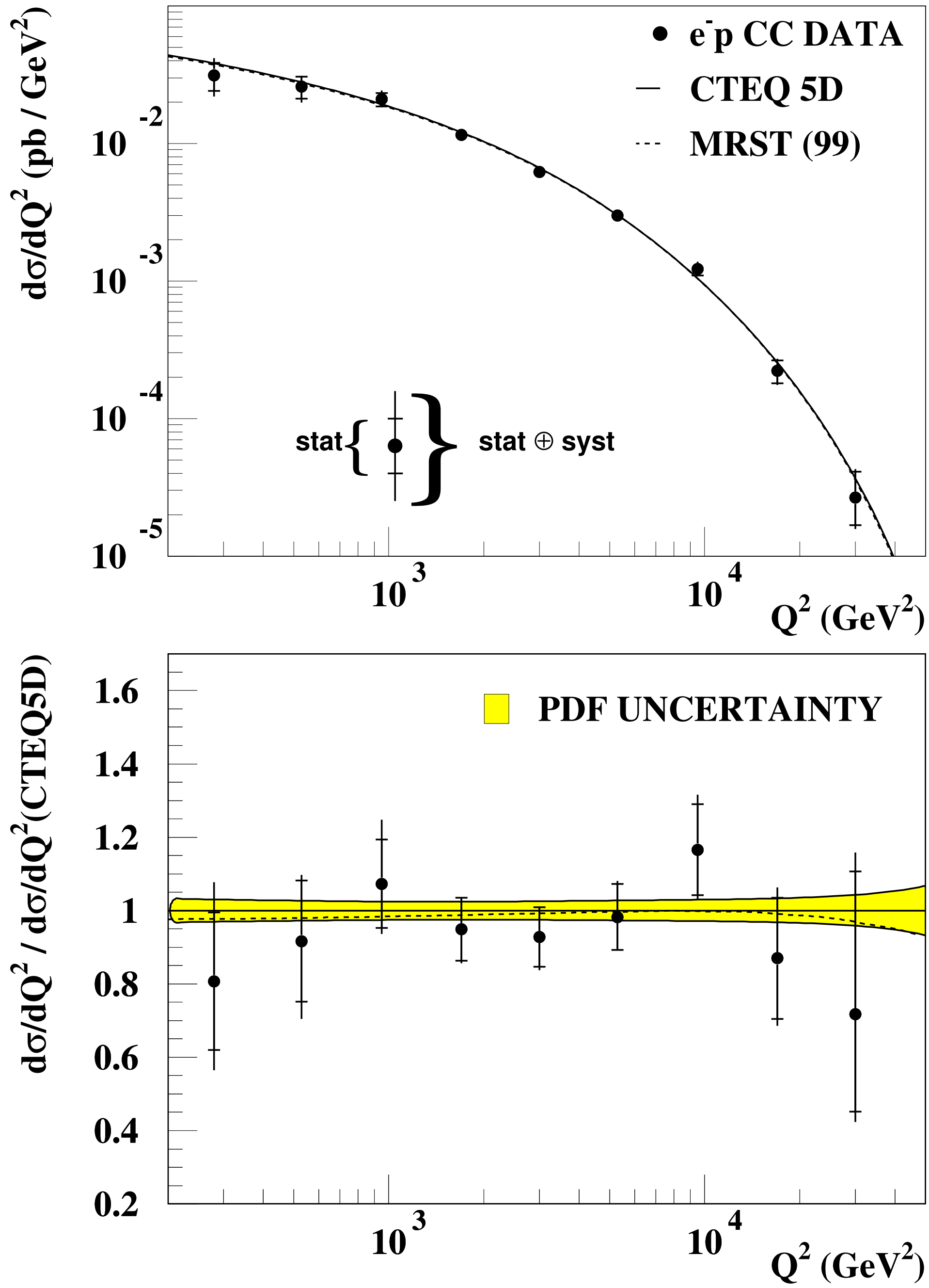

Figure 7.1: The measured single differential cross section $d\sigma/dQ^2(e^-p)$.

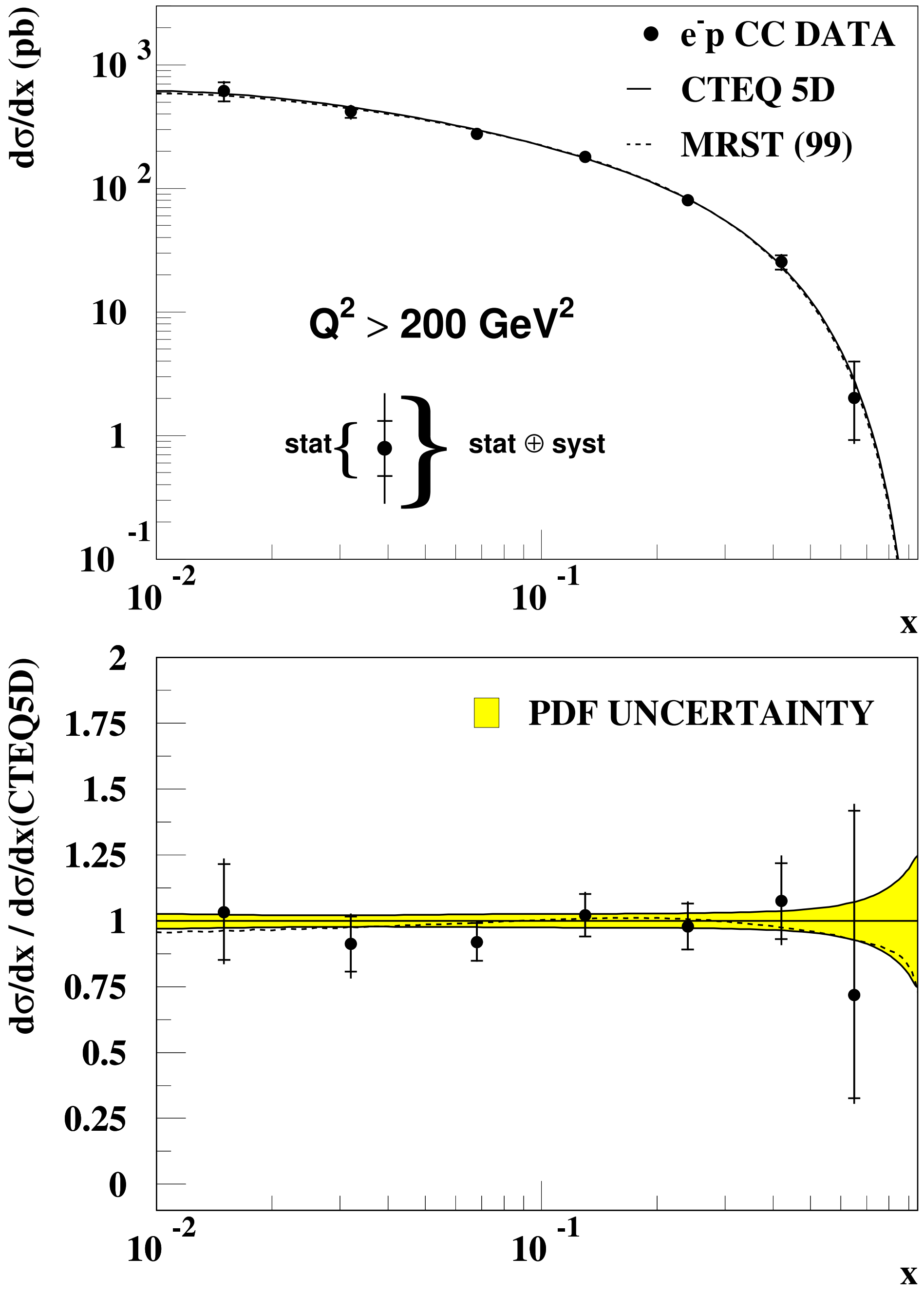

Figure 7.2: The measured single differential cross section $d\sigma/dx(e^{-}p)$.

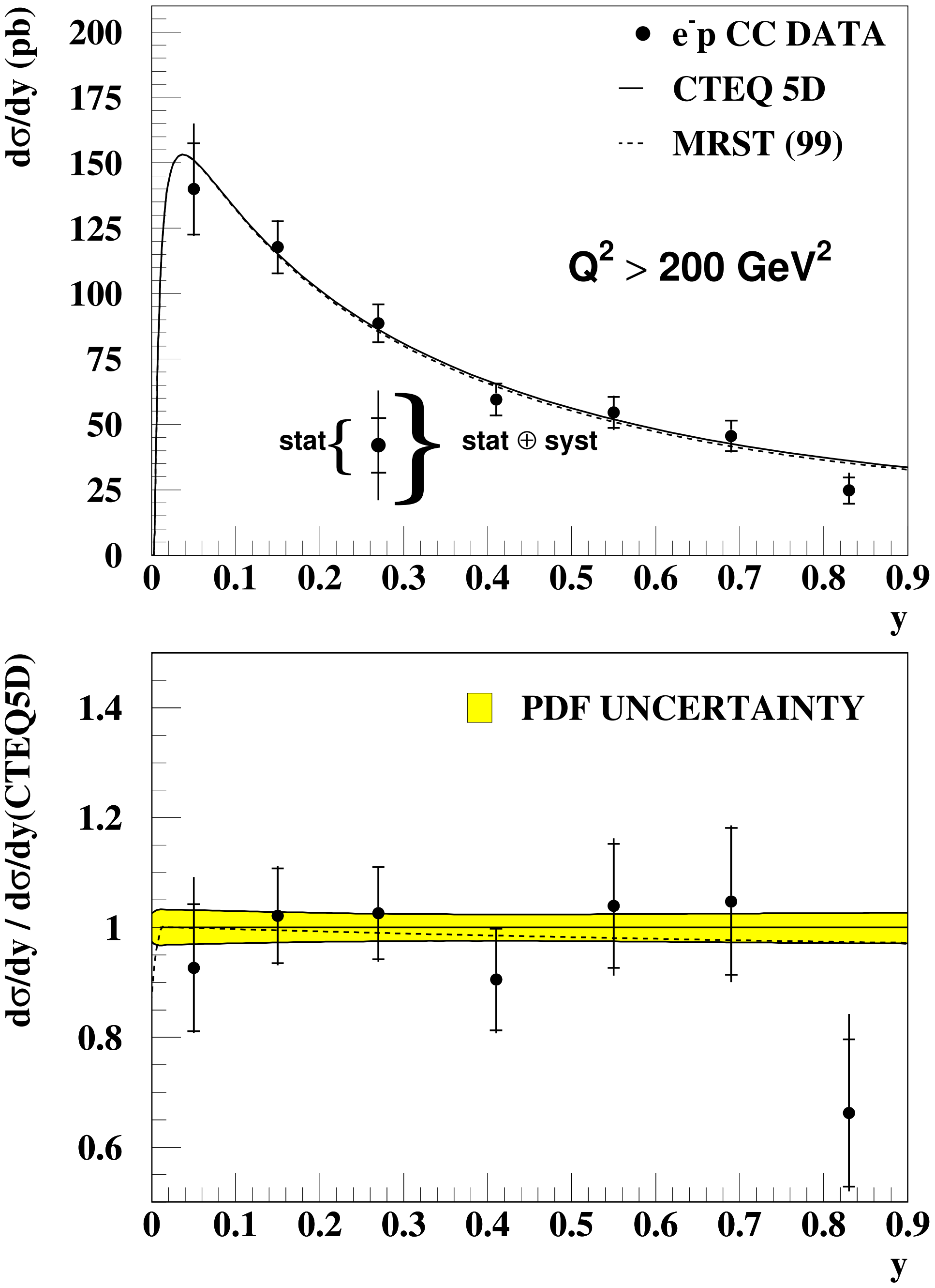

Figure 7.3: The measured single differential cross section $d\sigma/dy(e^-p)$.

$$\tilde{\sigma} = x[(u + c) + (1 - y)^2(\bar{d} + \bar{s})] \tag{7.3}$$

and for e^+p scattering:

$$\tilde{\sigma} = x[(\bar{u} + \bar{c}) + (1 - y)^2(d + s)] \tag{7.4}$$

The reduced cross section was evaluated using the values $G_F = 1.16639 \cdot 10^{-5}$ GeV^{-2} and $M_W = 80.419$ GeV from the PDG [42]. Figure 7.4 shows the reduced cross section as a function of x in bins of Q^2. The measurement is compared to the SM expectation evaluated with the CTEQ5D parameterisation of the parton density functions. Also shown separately are the expected contributions from the $(u + c)$ and $(1 - y)^2(\bar{d} + \bar{s})$ terms from the LO QCD CTEQ5L fit. It can be seen that at low Q^2 the sea quark contribution makes up a significant fraction of the total cross section, and both sea and valence contributions are necessary to describe the data. At high Q^2 the cross section is dominated by the contribution from the valence quarks.

The reduced cross section is plotted as a function of Q^2 in bins of x in figure 7.5. The measurement is compared to the SM expectation evaluated with the CTEQ5D and MRST (99) parameterisations of the parton density functions, and found to be well described by both.

The total cross section for charged current DIS in the kinematic region $Q^2 > 200$ GeV^2 was also measured, and found to be:

$$\sigma^{CC}(Q^2 > 200 \text{ GeV}^2) = 66.09 \pm 2.65(\text{stat})^{+1.50}_{-0.96}(\text{syst}) \text{ pb} \tag{7.5}$$

The Standard Model expectation evaluated using the CTEQ5D parameterisation of the parton density functions is 67.72 pb.

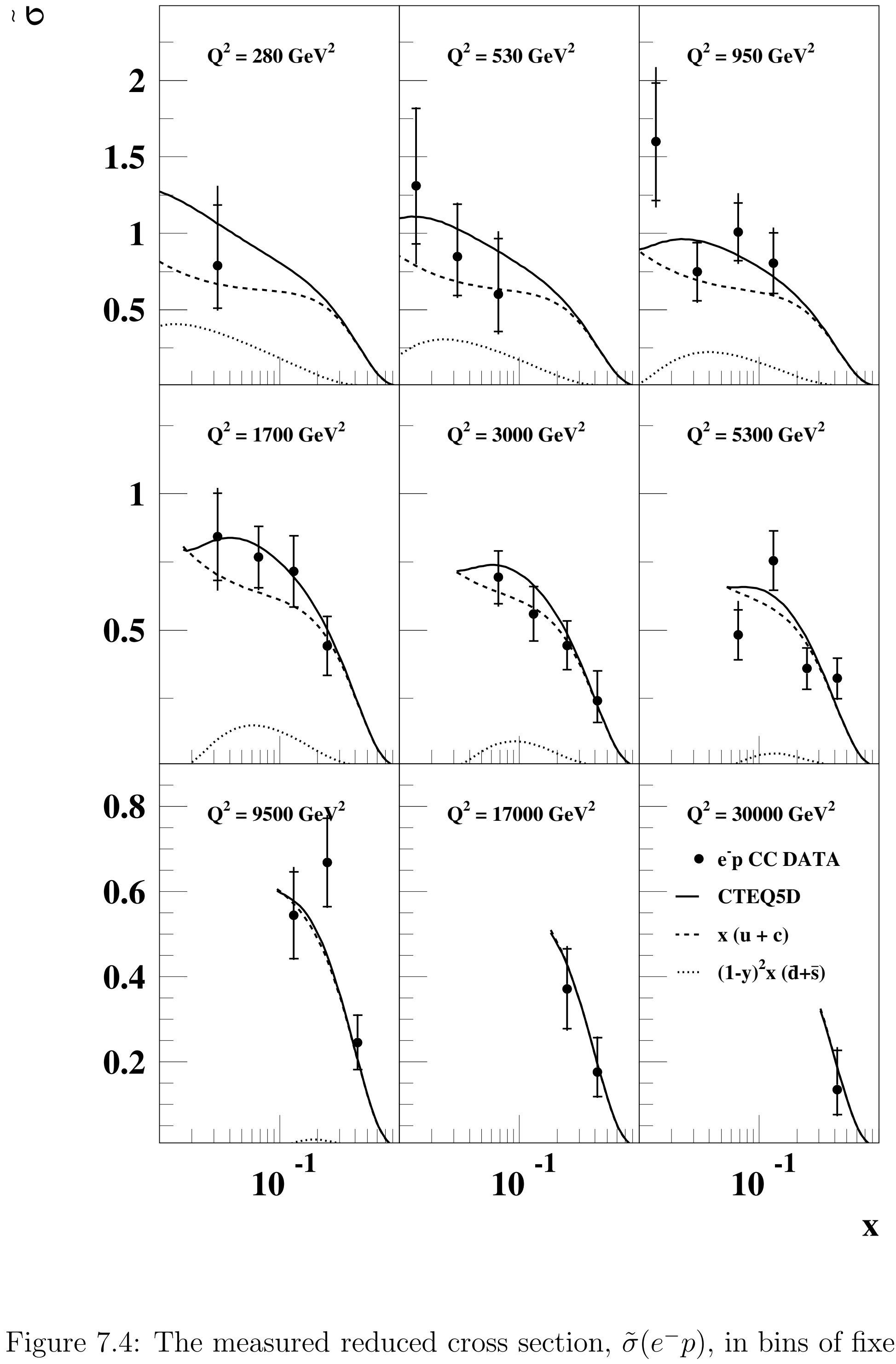

Figure 7.4: The measured reduced cross section, $\tilde{\sigma}(e^-p)$, in bins of fixed Q^2.

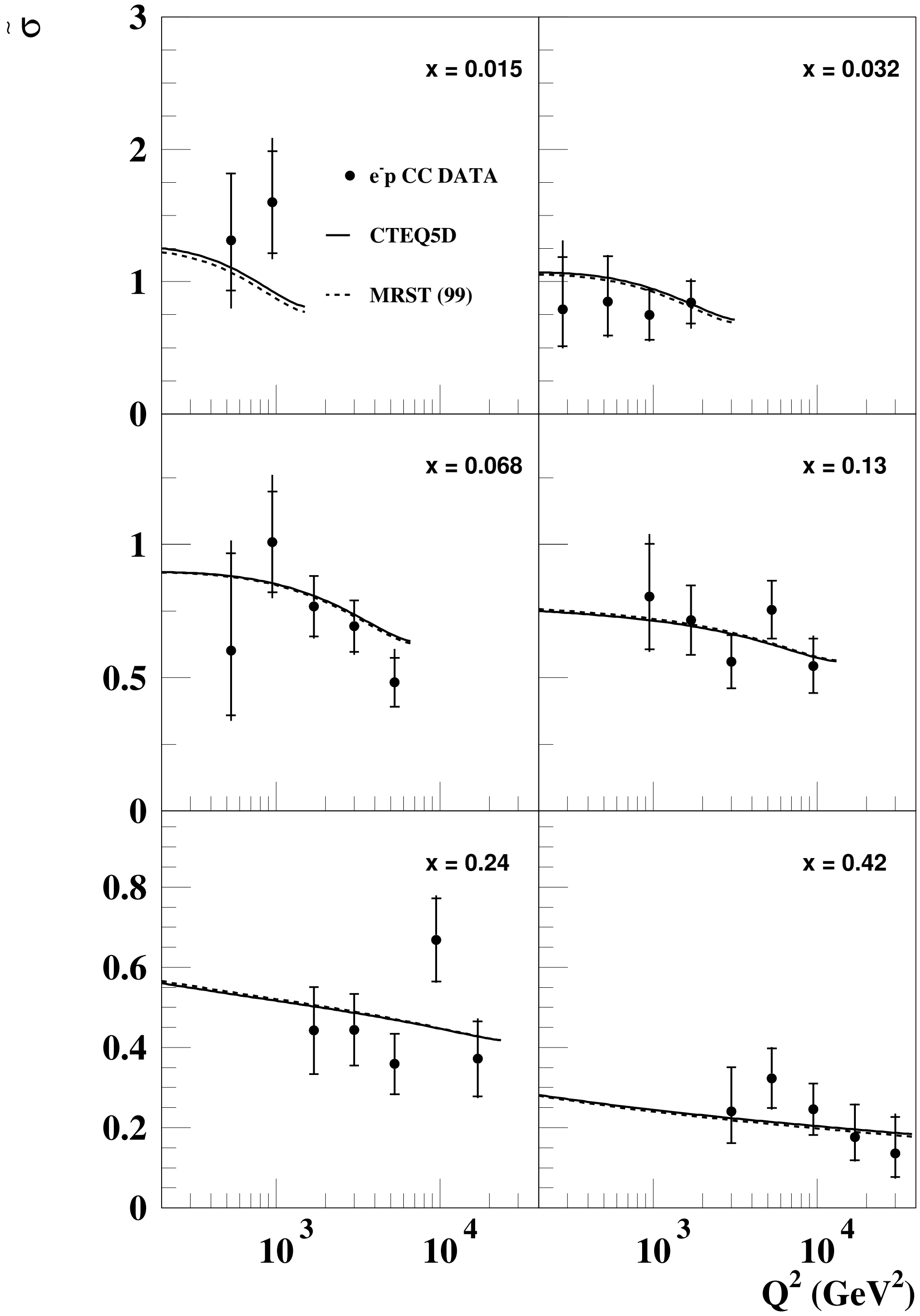

Figure 7.5: The measured reduced cross section, $\tilde{\sigma}(e^-p)$, in bins of fixed x.

7.2 Comparison of $e^{\pm}p$ CC DIS cross sections

Figures 7.6 and 7.7 show the ratios of the measured single differential cross sections for e^-p scattering to the cross sections for charged current e^+p scattering [43]. In each case only the statistical error is shown. It can be seen in figure 7.6 that $d\sigma_{Born}^{CC}/dQ^2$ is about 1.5 times larger for e^-p scattering than e^+p scattering, rising to about a factor of 40 at $Q^2 \sim 30000$ GeV^2. Similarly in figure 7.7 the cross section $d\sigma_{Born}^{CC}/dx$ is higher for e^-p scattering than e^+p scattering, increasing with rising x. The larger cross section for e^-p charged current scattering compared to e^+p scattering occurs for two reasons. Firstly, the largest contribution to e^-p scattering comes from the u-quark density, and for e^+p scattering from the d-quark density. In the quark parton model the u-quark density is approximately twice as large as the d-quark density, so the cross section is higher for this reason. Also as discussed in section 1.3.1, the quarks are suppressed by a factor of $(1-y)^2$ in e^+p, as a direct consequence of helicity conservation in the weak interaction.

In figure 7.8, the reduced cross section is plotted as a function of $(1-y)^2$. This illustrates the helicity structure of the charged current interaction (see section 1.3.1). To leading order in α_S and in the region of approximate scaling, $x \sim 0.1$, this yields a straight line, whose intercept gives the $(u+c)$ quark contribution and whose slope gives the $(\bar{d}+\bar{s})$ quark contribution, for e^-p scattering and the corresponding antiquark contributions for e^+p scattering.

7.3 Comparison of CC and NC DIS cross sections

It can be seen by comparing sections 1.3.1 and 1.3.2 that there are important differences between the forms of the charged and neutral current DIS cross sections. Firstly all the quark and antiquark flavours accessable at HERA contribute to the cross section for neutral current DIS, since they can all couple to the exchanged

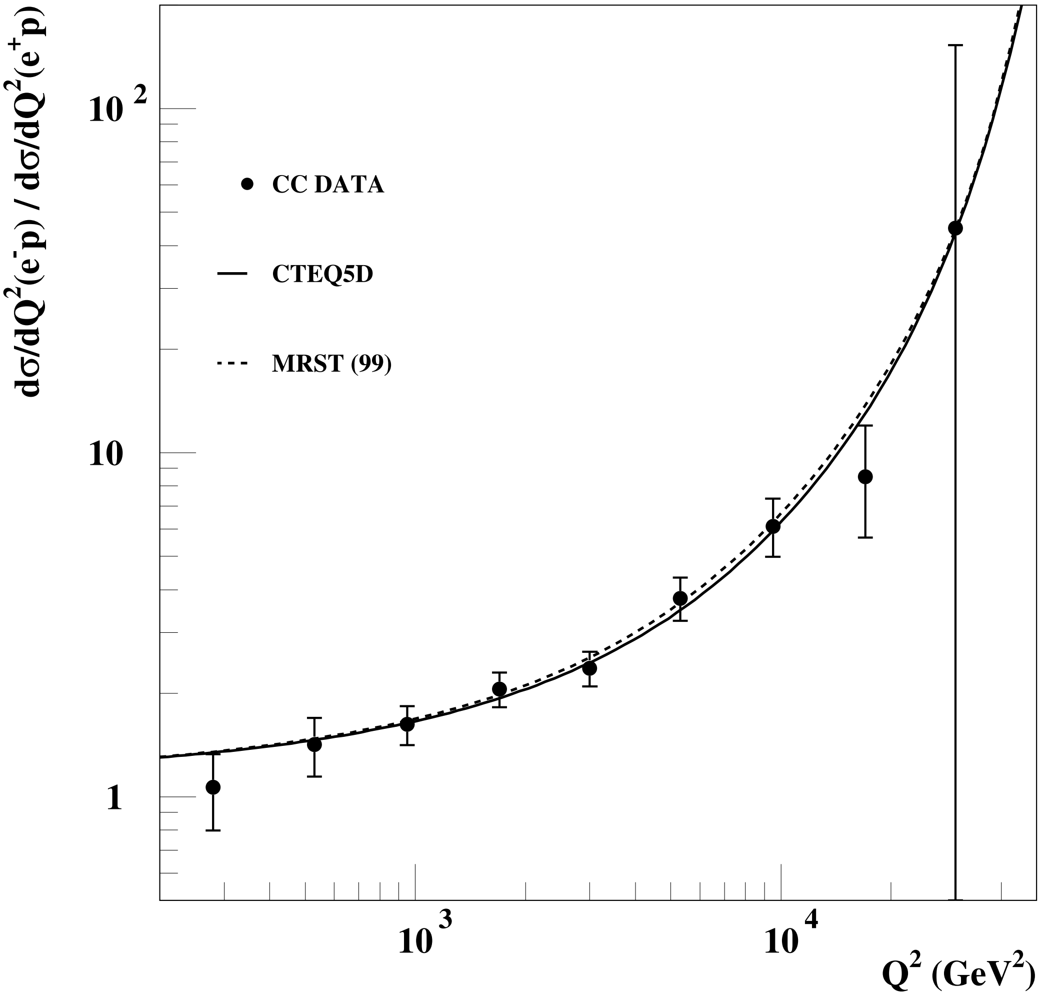

Figure 7.6: The ratio of $d\sigma^{CC}_{Born}/dQ^2$ for e^-p and e^+p scattering.

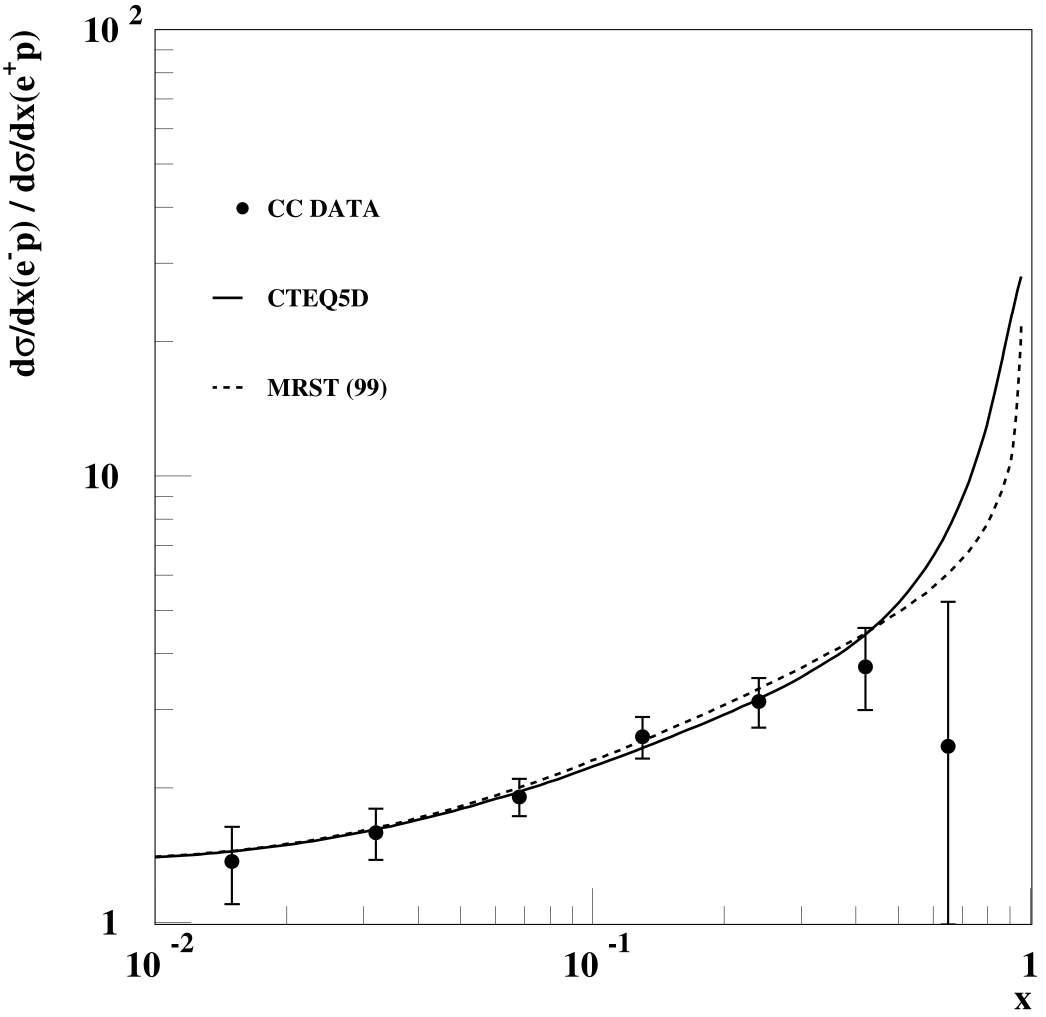

Figure 7.7: The ratio $d\sigma^{CC}_{Born}/dx$ for e^-p and e^+p scattering.

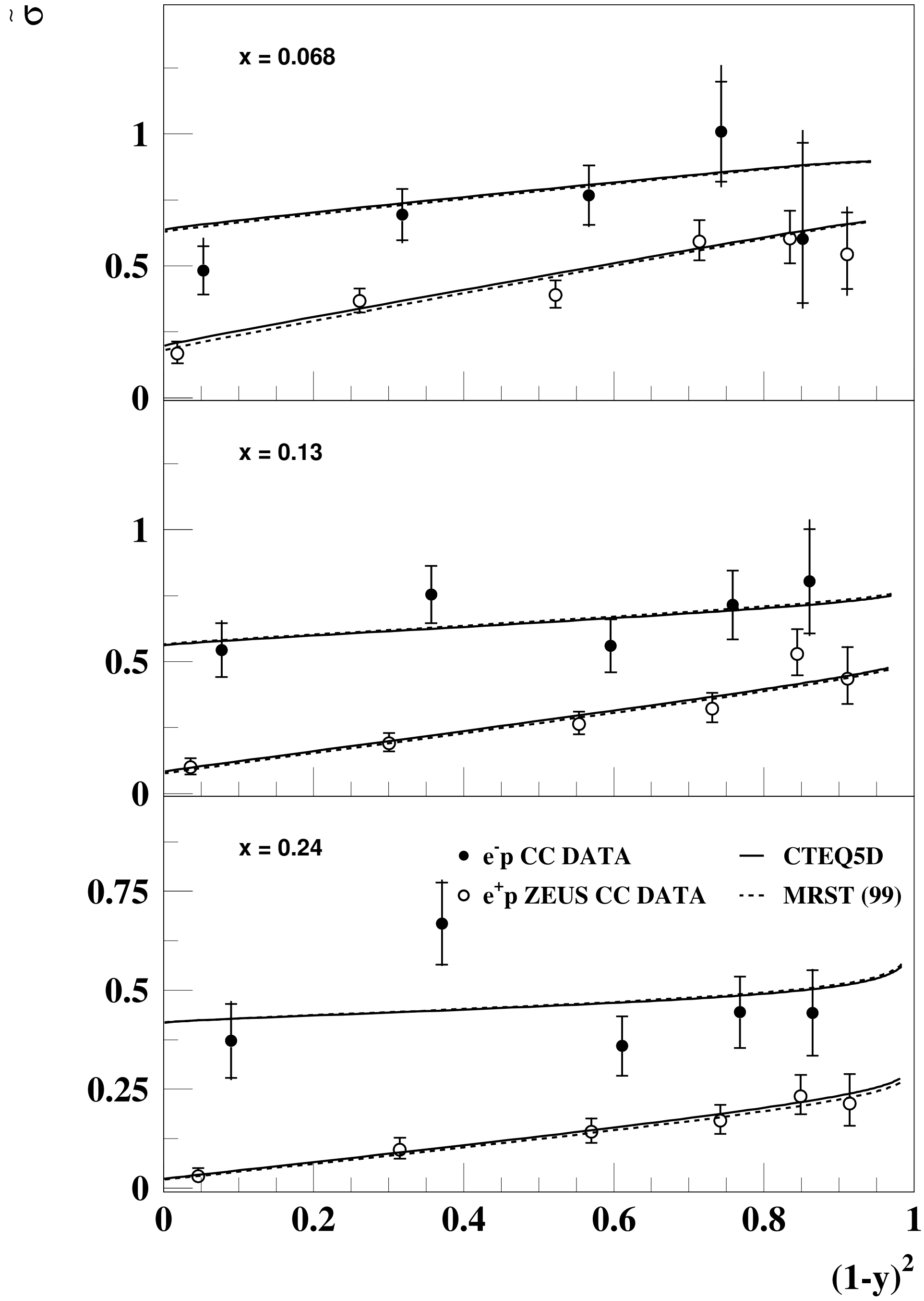

Figure 7.8: The measured reduced cross section, $\tilde{\sigma}(e^{\pm}p)$, in bins of fixed x, plotted as a function of the helicity structure $(1-y)^2$.

photon or Z^0 boson. This is not the case in charged current DIS in which, for e^-p scattering, the exchanged W boson interacts only with positively charged quarks and antiquarks in the proton and vice versa for e^+p scattering. Another important difference is seen in the propagator terms of the CC and NC DIS cross sections. Neutral current DIS can occur through the exchange of a photon or a Z^0 boson. The form of the propagator means that Z^0 exchange is highly suppressed compared to photon exchange for low values of Q^2, due to the large mass of the Z^0. Only when Q^2 approaches M_Z^2, does Z^0 exchange contribute significantly. The charged current cross section is suppressed at low Q^2 by the large mass of the W boson.

The cross sections for charged and neutral current e^-p deep inelastic scattering, as a function of Q^2, are shown in figure 7.9. It can be seen that the cross section for NC DIS is significantly larger than that for CC DIS at lower values of Q^2. When $Q^2 \approx M_W^2 \approx M_Z^2$ the exchange of a Z^0 in the NC interaction and the exchange of a W in charged current scattering are no longer suppressed by the large masses of the bosons and the NC and CC cross sections have similar magnitudes. This demonstrates electroweak unification at the scale of $Q^2 \approx M_W^2 \approx M_Z^2$.

7.4 Electroweak analysis of the CC DIS cross section

It can be seen from section 1.3.1 that the absolute magnitude of the charged current DIS cross section is determined by the Fermi constant, G_F, and the PDFs. The Q^2 dependence however arises mainly from the propagator term $M_W^4/(M_W^2+Q^2)^2$. An electroweak analysis was performed on the measured cross section. A fit to $d\sigma_{Born}^{CC}/dQ^2(e^-p)$ with G_F and the mass of the W boson, M_W, treated as free parameters yields the results

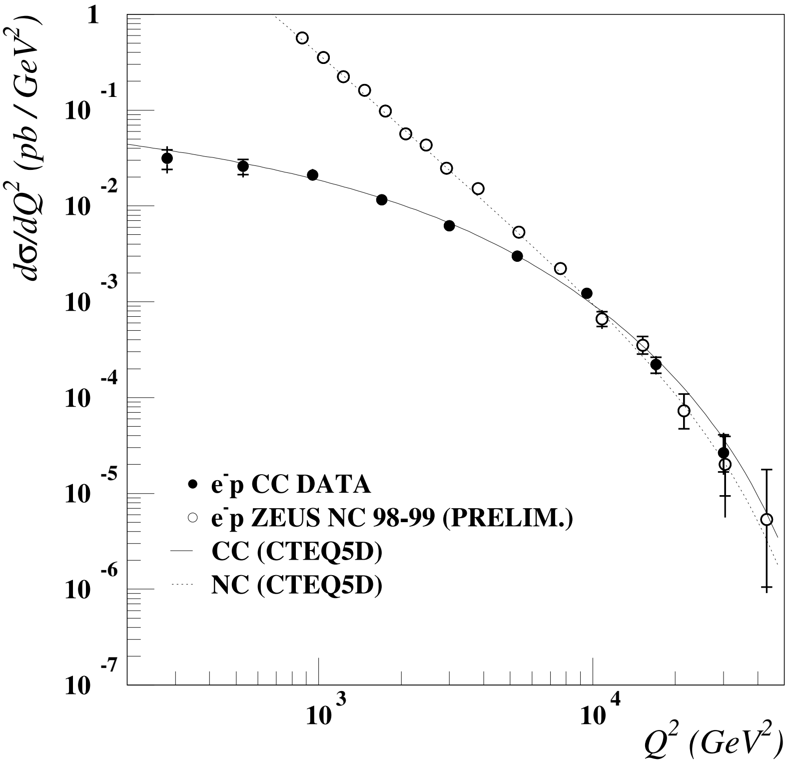

Figure 7.9: Measurements of the single differential cross section $d\sigma/dQ^2$, for NC and CC e^-p DIS.

$$M_W = 81.9^{+4.4}_{-4.2}(stat)^{+4.9}_{-4.0}(syst)^{+0.34}_{-0.06}(PDF)\ \text{GeV} \tag{7.6}$$

and

$$G_F = (1.140^{+0.046}_{-0.045}(stat)^{+0.043}_{-0.041}(syst)^{+0.012}_{-0.015}(PDF)) \cdot 10^{-5}\ \text{GeV}^{-2} \tag{7.7}$$

The systematic uncertainty includes contributions from the sources identified in section 6.3 and the overall uncertainty on the measured luminosity. In addition, the uncertainty arising from the knowledge of the PDFs was estimated by varying the PDFs within the uncertainties given in the ZEUS NLO fit [41].

Repeating the fit with G_F fixed to the PDG [42] value of $1.16639 \cdot 10^{-5}$ GeV^{-2} gives the result:

$$M_W = 79.8 \pm 2.1(stat)^{+1.8}_{-1.4}(syst)^{+1.3}_{-1.2}(PDF)\ \text{GeV} \tag{7.8}$$

Figure 7.10 shows the results of these fits. The value of G_F is found to be in good agreement with the value obtained from measurements of muon decay [42], and the values of M_W are found to be in good agreement with measurements of time-like W boson production made at the Tevatron and LEP [42].

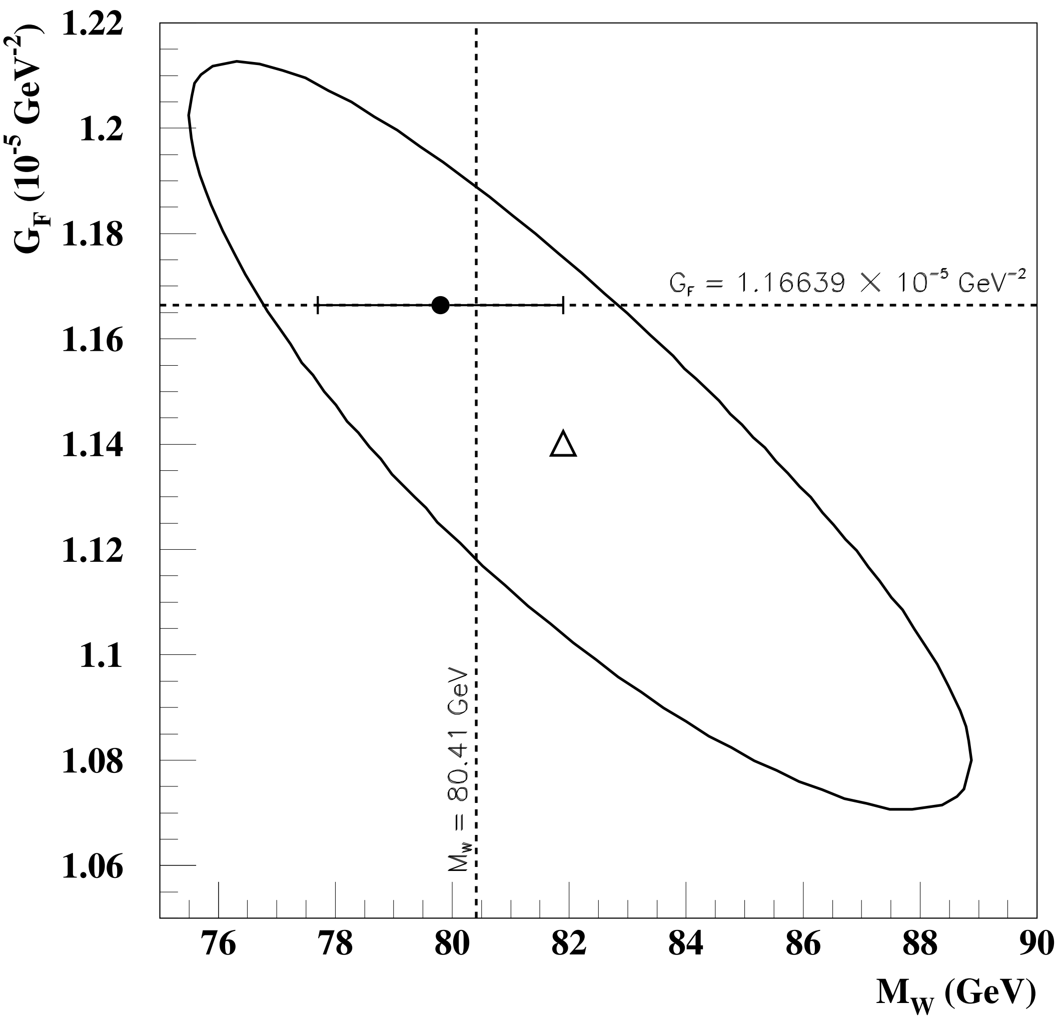

Figure 7.10: The result of fits to $d\sigma^{CC}_{Born}/dQ^2(e^-p)$ to determine G_F and M_W. The open triangle indicates the result of the fit treating G_F and M_W as free parameters. The ellipse shows the 70% confidence level contour for this fit. The filled circle shows the result of fitting for M_W with G_F set to the PDG value. Dotted lines show the PDG fit values of G_F and M_W.

Chapter 8

Conclusions

The cross section for charged current $e^- p$ deep inelastic scattering has been measured at a centre of mass energy of 318 GeV. The measurement is based on 16.4 pb^{-1} of $e^- p$ data taken by the ZEUS detector at HERA in 1998 and early 1999. The single differential cross sections with respect to Q^2, x and y: $d\sigma^{CC}_{Born}/dQ^2(e^- p)$; $d\sigma^{CC}_{Born}/dx(e^- p)$ and $d\sigma^{CC}_{Born}/dy(e^- p)$ and the total cross section were measured in the kinematic region $Q^2 > 200$ GeV^2, where background contamination was estimated to be less than 1%. The total cross section was found to be $\sigma^{CC}(Q^2 > 200 \text{ GeV}^2) = 66.09 \pm 2.65(\text{stat})^{+1.50}_{-0.96}(\text{syst})$ pb. These measurements benefit from approximately 40 times more luminosity than the previous ZEUS measurement of the cross sections for charged current $e^- p$ deep inelastic scattering [45], and extend the measured cross sections to higher Q^2 and higher x than the previous measurement. The reduced double differential cross section was also measured, in bins of x and Q^2 in the kinematic region $200 \text{ GeV}^2 < \text{Q}^2 < 60000 \text{ GeV}^2$ and $0.01 < x < 0.56$. The measurements are confonted with the Standard Model predictions evaluated using the CTEQ5D and MRST (99) parameterisations of the parton density functions. Both parameterisations are found to describe the data well. The measurements are compared with previous measured cross sections for $e^+ p$ charged current deep inelastic scattering [43], and cross sections for neutral current deep inelastic scattering [44].

An electroweak analysis has also been performed on the measured cross section. A fit to $d\sigma^{CC}_{Born}/dQ^2(e^-p)$ with the Fermi constant, G_F, and the mass of the W boson, M_W, treated as free parameters yields the results

$$M_W = 81.9^{+4.4}_{-4.2}(stat)^{+4.9}_{-4.0}(syst)^{+0.34}_{-0.06}(PDF)\ \text{GeV} \tag{8.1}$$

and

$$G_F = (1.140^{+0.046}_{-0.045}(stat)^{+0.043}_{-0.041}(syst)^{+0.012}_{-0.015}(PDF)) \cdot 10^{-5}\ \text{GeV}^{-2} \tag{8.2}$$

Fixing G_F to the PDG value of $1.16639 \cdot 10^{-5}$ GeV^{-2} gives the result:

$$M_W = 79.8 \pm 2.1(stat)^{+1.8}_{-1.4}(syst)^{+1.3}_{-1.2}(PDF)\ \text{GeV} \tag{8.3}$$

The value of G_F is found to be in good agreement with the value obtained from measurements of muon decay [42], and the values of M_W are found to be in good agreement with measurements of time-like W boson production made at the Tevatron and LEP [42].

Measurements of the charged and neutral current deep inelastic scattering cross sections at the highest possible Q^2 and x are currently limited by statistics. In the future, the completion of the HERA upgrade should vastly increase the luminosity delivered, and provide longitudinally polarised lepton beams. The increased luminosity will result in more precise cross section measurements in the high Q^2 and high x regions and increased sensitivity to the electroweak parameters. The charged current cross section is proportional to 1±P where P is the longitudinal polarisation of the lepton beam and the ± represents the charge of the lepton beam. Measurements of the charged current cross section made with longitudinally polarised lepton beams will be combined with the currently available unpolarised measurements to explore the electroweak sector. Figure 8.1 shows the total cross sections for charged current DIS as a function of polarisation.

The points at zero polarisation are the e^-p measurement presented in this analysis and the ZEUS measurement for e^+p scattering [43]. The points at non-zero polarisation are taken from Monte Carlo simulation, and show how future running with polarised lepton beams can determine the dependence of the charged current cross section on lepton beam polarisation.

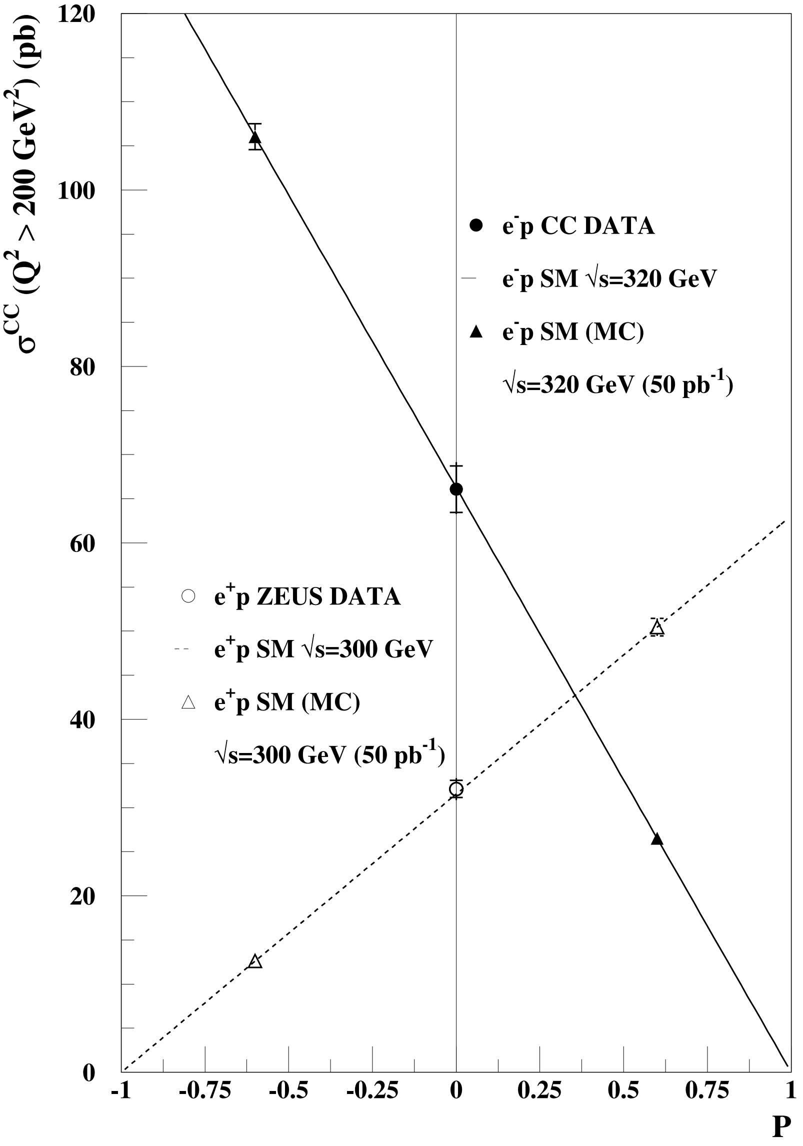

Figure 8.1: The total CC DIS cross section for both e^-p and e^+p scattering, plotted as a function of lepton beam polarisation, P.

Appendix

Q^2 range (GeV^2)	Q_0^2 (GeV^2)	N_{meas}^{data}	N_{meas}^{bkgd}	$\mathcal{A}$	$\mathcal{C}_{rad}$	$d\sigma/dQ^2$ (pb/GeV^2)
200 - 400	280	21	0.92	0.20	0.98	$3.13 \pm 0.73^{+0.75}_{-0.60} \cdot 10^{-2}$
400 - 711	530	32	0.18	0.25	0.99	$2.59 \pm 0.47^{+0.21}_{-0.38} \cdot 10^{-2}$
711 - 1270	950	82	0.57	0.46	1.01	$2.09 \pm 0.24^{+0.25}_{-0.12} \cdot 10^{-2}$
1270 - 2250	1700	127	1.51	0.72	1.03	$1.16 \pm 0.11^{+0.02}_{-0.04} \cdot 10^{-2}$
2250 - 4000	3000	134	0.75	0.83	1.03	$6.20 \pm 0.54^{+0.09}_{-0.26} \cdot 10^{-3}$
4000 - 7110	5300	122	0.44	0.90	1.05	$2.98 \pm 0.27^{+0.12}_{-0.04} \cdot 10^{-3}$
7110 - 12600	9500	89	0.23	0.93	1.07	$1.22 \pm 0.13^{+0.09}_{-0.06} \cdot 10^{-3}$
12600 - 22500	17000	28	0.08	0.94	1.09	$2.22 \pm 0.42^{+0.26}_{-0.21} \cdot 10^{-4}$
22500 - 60000	30000	7	0.03	1.15	1.09	$2.65^{+1.44+0.77}_{-0.98-0.46} \cdot 10^{-5}$

Table 1: Values of the differential cross section $d\sigma/dQ^2(e^-p)$. For each bin the following quantities are given: the Q^2 range; the value at which the cross section is quoted, Q_0^2; the number of data events, N_{meas}^{data}; the number of expected background events, N_{meas}^{bkgd}; the acceptance, $\mathcal{A}$; the radiative correction factor, $\mathcal{C}_{rad}$, and the measured Born level cross section $d\sigma/dQ^2$, with statistical and systematic uncertainties.

x range	x_0	N^{data}_{meas}	N^{bkgd}_{meas}	$\mathcal{A}$	$\mathcal{C}_{rad}$	$d\sigma/dx$ (pb)
0.010 - 0.021	0.015	35	0.85	0.32	1.00	$6.17\pm1.09^{+0.55}_{-0.47} \cdot 10^2$
0.021 - 0.046	0.032	80	0.92	0.51	1.00	$4.20\pm0.48^{+0.23}_{-0.36} \cdot 10^2$
0.046 - 0.100	0.068	171	0.15	0.76	1.01	$2.75\pm0.22^{+0.12}_{-0.06} \cdot 10^2$
0.100 - 0.178	0.130	161	0.62	0.78	1.02	$1.79\pm0.14^{+0.07}_{-0.02} \cdot 10^2$
0.178 - 0.316	0.240	127	0.21	0.75	1.04	$8.04\pm0.72^{+0.32}_{-0.21} \cdot 10^1$
0.316 - 0.562	0.420	56	0.03	0.61	1.06	$2.54\pm0.34^{+0.23}_{-0.20} \cdot 10^1$
0.562 - 1.000	0.650	3	0.00	0.48	1.10	$2.01^{+1.96+0.54}_{-1.10-0.37} \cdot 10^0$

Table 2: Values of the differential cross section $d\sigma/dx(e^-p)$. For each bin the following quantities are given: the x range; the value at which the cross section is quoted, x_0; the number of data events, N^{data}_{meas}; the number of expected background events, N^{bkgd}_{meas}; the acceptance, $\mathcal{A}$; the radiative correction factor, $\mathcal{C}_{rad}$, and the measured Born level cross section $d\sigma/dx$, with statistical and systematic uncertainties.

y range	y_0	N^{data}_{meas}	N^{bkgd}_{meas}	$\mathcal{A}$	$\mathcal{C}_{rad}$	$d\sigma/dy$ (pb)
0.00 - 0.10	0.05	66	0.34	0.34	0.99	$1.40\pm0.18^{+0.18}_{-0.04} \cdot 10^2$
0.10 - 0.20	0.15	145	0.85	0.77	0.99	$1.18\pm0.10^{+0.03}_{-0.03} \cdot 10^2$
0.20 - 0.34	0.27	154	0.61	0.75	1.00	$8.87\pm0.72^{+0.10}_{-0.25} \cdot 10^1$
0.34 - 0.48	0.41	100	1.13	0.74	1.02	$5.96\pm0.61^{+0.15}_{-0.22} \cdot 10^1$
0.48 - 0.62	0.55	87	0.48	0.69	1.02	$5.46\pm0.59^{+0.26}_{-0.31} \cdot 10^1$
0.62 - 0.76	0.69	63	0.30	0.59	1.03	$4.56\pm0.58^{+0.17}_{-0.27} \cdot 10^1$
0.76 - 0.90	0.83	27	1.08	0.45	1.07	$2.47\pm0.50^{+0.45}_{-0.18} \cdot 10^1$

Table 3: Values of the differential cross section $d\sigma/dy(e^-p)$. For each bin the following quantities are given: the y range; the value at which the cross section is quoted, y_0; the number of data events, N^{data}_{meas}; the number of expected background events, N^{bkgd}_{meas}; the acceptance, $\mathcal{A}$; the radiative correction factor, $\mathcal{C}_{rad}$, and the measured Born level cross section $d\sigma/dy$, with statistical and systematic uncertainties.

Q^2 range (GeV^2)	Q_0^2 (GeV^2)	x range	x_0	N_{meas}^{data}	N_{meas}^{bkgd}	$\mathcal{A}$	$\mathcal{C}_{rad}$	$\tilde{\sigma}$
200 - 400	280	0.021 - 0.046	0.032	8	0.10	0.48	0.96	$0.789^{+0.396+0.341}_{-0.279-0.095}$
400 - 711	530	0.010 - 0.021	0.015	12	0.05	0.33	0.99	$1.310^{+0.505+0.085}_{-0.380-0.348}$
400 - 711	530	0.021 - 0.046	0.032	11	0.03	0.48	0.97	$0.849^{+0.343+0.078}_{-0.256-0.093}$
400 - 711	530	0.046 - 0.100	0.068	6	0.07	0.34	0.97	$0.602^{+0.365+0.195}_{-0.243-0.101}$
711 - 1265	950	0.010 - 0.021	0.015	18	0.02	0.32	1.03	$1.600^{+0.385+0.299}_{-0.385-0.190}$
711 - 1265	950	0.021 - 0.046	0.032	16	0.10	0.48	0.99	$0.749^{+0.190+0.061}_{-0.190-0.069}$
711 - 1265	950	0.046 - 0.100	0.068	30	0.36	0.65	0.98	$1.010^{+0.189+0.168}_{-0.189-0.093}$
711 - 1265	950	0.100 - 0.178	0.130	17	0.08	0.63	1.00	$0.805^{+0.198+0.126}_{-0.198-0.061}$
1265 - 2249	1700	0.021 - 0.046	0.032	29	0.34	0.55	1.02	$0.842^{+0.160+0.081}_{-0.160-0.115}$
1265 - 2249	1700	0.046 - 0.100	0.068	48	0.31	0.95	1.01	$0.768^{+0.113+0.015}_{-0.113-0.044}$
1265 - 2249	1700	0.100 - 0.178	0.130	31	0.16	0.88	1.03	$0.715^{+0.130+0.021}_{-0.130-0.017}$
1265 - 2249	1700	0.178 - 0.316	0.240	17	0.03	0.82	1.04	$0.442^{+0.108+0.024}_{-0.108-0.012}$
2249 - 4000	3000	0.046 - 0.100	0.068	53	0.33	0.90	1.02	$0.694^{+0.097+0.013}_{-0.097-0.047}$
2249 - 4000	3000	0.100 - 0.178	0.130	32	0.08	0.94	1.01	$0.560^{+0.100+0.004}_{-0.100-0.005}$
2249 - 4000	3000	0.178 - 0.316	0.240	25	0.05	0.92	1.03	$0.444^{+0.090+0.011}_{-0.090-0.001}$
2249 - 4000	3000	0.316 - 0.562	0.420	9	0.00	0.63	1.07	$0.241^{+0.110+0.013}_{-0.079-0.013}$
4000 - 7113	5300	0.046 - 0.100	0.068	29	0.34	0.92	1.07	$0.483^{+0.091+0.085}_{-0.091-0.005}$
4000 - 7113	5300	0.100 - 0.178	0.130	49	0.05	0.92	1.03	$0.755^{+0.109+0.014}_{-0.109-0.008}$
4000 - 7113	5300	0.178 - 0.316	0.240	23	0.02	0.91	1.04	$0.359^{+0.075+0.003}_{-0.075-0.020}$
4000 - 7113	5300	0.316 - 0.562	0.420	19	0.00	0.86	1.05	$0.323^{+0.075+0.021}_{-0.075-0.026}$
7113 - 12649	9500	0.100 - 0.178	0.130	29	0.18	0.96	1.07	$0.544^{+0.102+0.050}_{-0.102-0.021}$
7113 - 12649	9500	0.178 - 0.316	0.240	42	0.02	0.92	1.04	$0.669^{+0.104+0.039}_{-0.104-0.027}$
7113 - 12649	9500	0.316 - 0.562	0.420	15	0.00	0.89	1.07	$0.246^{+0.064+0.018}_{-0.064-0.013}$
12649 - 22494	17000	0.178 - 0.316	0.240	16	0.05	0.96	1.09	$0.372^{+0.093+0.038}_{-0.093-0.031}$
12649 - 22494	17000	0.316 - 0.562	0.420	9	0.00	0.91	1.05	$0.177^{+0.081+0.021}_{-0.058-0.018}$
22494 - 60000	30000	0.316 - 0.562	0.420	5	0.00	1.12	1.09	$0.135^{+0.092+0.039}_{-0.059-0.022}$

Table 4: Values of the reduced double differential cross section $\tilde{\sigma}(e^-p)$. For each bin the following quantities are given: the Q^2 range; the value at which the cross section is quoted, Q_0^2; the x range; the value at which the cross section is quoted, x_0;the number of data events, N_{meas}^{data}; the number of expected background events, N_{meas}^{bkgd}; the acceptance, $\mathcal{A}$; the radiative correction factor, $\mathcal{C}_{rad}$, and the measured Born level reduced cross section, $\tilde{\sigma}$, with statistical and systematic uncertainties.

Bibliography

[1] For example: F. Halzen and A. Martin, "Quarks and Leptons", Wiley (1984).

[2] ZEUS Collab., "Measurement of the proton structure function F_2 in e^+p collisions at HERA", Abstract 1048, XXX International Conference on High-Energy Physics, Osaka, July 27 - August 2.

[3] A. M. Cooper-Sarkar, R. Devenish, A. de Roeck, Int'l J. Mod. Phys. **A13** (1998) 3385.

[4] V. N. Gribov, L. N. Lipatov, Sov. J. Nucl. Phys., **15** (1972) 438.
L. N. Lipatov, Sov. J. Nucl. Phys., **20** (1975) 96.
Y. L. Dokshitzer, Sov. Phys. JETP, **46** (1977) 641.
G. Altarelli, G. Parisi, Nucl. Phys., **B126** (1977) 298.

[5] H. L. Lai *et al.*, Phys. Rev. **D55** (1997) 1280.

[6] A. D. Martin *et al.*, Eur. Phys. J. **C14** (2000) 133-145.

[7] A.M. Cooper-Sarkar, "NLO QCD fits of ZEUS data", ZEUS Note 00-041.

[8] HERA, "A Proposal for a Large Electron-Proton Colliding Beam Facility at DESY", DESY HERA 81-10.

[9] ZEUS Collab., "The ZEUS Detector", Status Report 1993, ed. U. Holm, DESY (1993) (unpublished).

[10] M. Derrick *et al.*, Nucl. Inst. Meth., **A309** (1991) 77.
A. Andresen *et al.*, Nucl. Inst. Meth., **A309** (1991) 101.
B. Bernstein *et al.*, Nucl. Inst. Meth., **A336** (1993) 23.

[11] B. Foster *et al.*, Nucl. Inst. Meth., **A338** (1994) 254.

[12] R. Hall-Wilton *et al.*, "The CTD Tracking Resolution", ZEUS Note 99-024.

[13] H. Bethe, W. Heitler, Proc. Roy. Soc., **A146** (1934) 83.

[14] K. Olkiewicz, A. Eskreys, "Off-line Luminosity Calculation in the ZEUS Experiment in 1997, 1998 and 1999", ZEUS Note 99-044.

[15] W. H. Smith *et al.*, "The ZEUS Trigger System", ZEUS Note 89-084.

[16] W. H. Smith *et al.*, Nucl. Inst. Meth., **A355** (1995) 278.

[17] G.P. Heath *et al.*, Nucl. Inst. Meth. **A315** (1992) 431-435.

[18] H. Spiesberger, "HERACLES and DJANGOH: Event Generation for ep Interactions at HERA Including Radiative Processes", 1998, available on WWW: `http://www.desy.de/~hspiesb/djangoh.html`.

[19] A. Kwiatkowski, H. Spiesberger, H. J. Möhring, Comp. Phys. Commun. **69** (1992) 155-172.
H. Spiesberger, "HERACLES - An Event Generator for ep interactions at HERA Including Radiative Processes (Version 4.6)", 1996, available on WWW: `http://www.desy.de/~hspiesb/heracles.html`.

[20] L. Lönnblad, Comp. Phys. Commun. **71** (1992) 15.

[21] G. Ingelman, A. Edin, J. Rathsman, Comp. Phys. Commun. **101** (1997) 108-134.

[22] H. L. Lai *et al.*, Eur. Phys. J. **C12** (2000) 375-392.

[23] T. Sjöstrand, Comp. Phys. Commun. **82** (1994) 74.

[24] G. Marchesini *et al.*, Comp. Phys. Commun. **67** (1992) 465.

[25] J.A.M. Vermaseren, Nucl. Phys., **B229** (1983) 347.

[26] U. Baur, J.A.M. Vermaseren, D. Zeppenfeld, Nucl. Phys., **B375** (1992) 3.

[27] F. Jacquet, A. Blondel, "Proceedings of the study of an *ep* facility for Europe", DESY 79-48 391.

[28] S. Bentvelsen, J. Engelen, P. Kooijman, Proc. of the Workshop "Physics at HERA", vol. 1, Eds. W. Buchmüller and G. Ingelman, DESY (1991) 23.

[29] G. M. Briskin, "Diffractive Dissociation in *ep* Deep Inelastic Scattering", Ph.D. Thesis.

[30] M. Martinez, "Calorimeter Noisy Cell Study for 1998-2000 ZEUS Data", ZEUS Note 00-016.

[31] J. Grosse-Knetter, "Energy Correction for Islands", ZEUS Note 97-039.
J. Grosse-Knetter, "Corrections for the Hadronic Final State", ZEUS Note 98-031.
J. Grosse-Knetter, Minutes of the ZEUS SFEW physics group, 7th September 1999.

[32] G. F. Hartner *et al.*, "VCTRAK (3.07/04): Offline Output Information", ZEUS Note 97-064.
G. F. Hartner, "VCTRAK Briefing: Program and Math", ZEUS Note 98-058.

[33] J.R. Goncalo, K. Long, "A minimum bias vertex distribution for the 1998/99 e^-p data", ZEUS Note 00-027.

[34] R. Pawlak, "Vertex reconstruction from FCAL timing", ZEUS Note 98-040.

[35] K. Nagano, Minutes of the ZEUS High Q^2 and Exotics physics group, 12th December 1997.

[36] H. Abramowicz, A. Caldwell, R. Sinkus, "Neural Network Based Electron Identification in the ZEUS Calorimeter", DESY 95-054.
R. Sinkus, Nucl. Inst. Meth. **A361** (1995) 290.

[37] H. Abramowicz, ISITAMU algorithm, Phantom library.

[38] A. Kruse, A. v. Sighem, "MUFFINCUP - A Wrapper for MUFFIN User Manual and Documentation", ZEUS Note 98-025 .

[39] ZEUS Collab., J.Breitweg *et al.*, Eur. Phys. J. **C11** (1999) 3, 427-445.

[40] A. M. Cooper-Sarkar *et al.*, J. Phys. **G25** (1999) 1387-1409.
B. Heinemann, S. Riess, H. Spiesberger, "Radiative Corrections for Charged Current Scattering: A Comparison of Computer Codes", Proc. of the 1998/99 Workshop "Monte Carlo Generators for HERA Physics", DESY.

[41] M. Botje, DESY 99-038, NIKHEF-99-011.

[42] D. E. Groom *et al.*, Eur. Phys. J. **C15** (2000) 1.

[43] ZEUS Collab., J.Breitweg *et al.*, Eur. Phys. J. **C12** (2000) 3, 411-428.

[44] ZEUS Collab., "Measurement of high-Q^2 neutral current cross sections in e^-p DIS and a first measurement of the structure function xF_3 at HERA", Abstract 1049, XXX International Conference on High-Energy Physics, Osaka, July 27 - August 2.

[45] ZEUS Collab., M.Derrick *et al.*, Zeits. f. Phys. **C72** (1996) 1, 47-64.